

REPORT DOCUMENTATION PAGE

AD-A222 057

REPORT SECURITY CLASSIFICATION Unclassified		1b. RESTRICTIVE MARKINGS N/A	
SECURITY CLASSIFICATION AUTHORITY N/A		3. DISTRIBUTION/AVAILABILITY OF REPORT Unlimited	
DECLASSIFICATION/DOWNGRADING SCHEDULE N/A		5. MONITORING ORGANIZATION REPORT NUMBER(S) AFOSR-TR-90-0531	
PERFORMING ORGANIZATION REPORT NUMBER AFOSRFR		7a. NAME OF MONITORING ORGANIZATION Air Force Office of Scientific Research Directorate of Chemical & Atmospheric Sciences	
NAME OF PERFORMING ORGANIZATION Mesoscale Environmental Simulations & Operations, Inc.		7b. ADDRESS (City, State, and ZIP Code) Building 410 Bolling AFB, DC 20332-6448	
6c. ADDRESS (City, State, and ZIP Code) Langley Executive Center 28 Research Drive Hampton, VA 23666-1325		9. PROCUREMENT INSTRUMENT IDENTIFICATION NUMBER F49620-86-C-0044	
8a. NAME OF FUNDING/SPONSORING ORGANIZATION Air Force Office of Scientific Research		10. SOURCE OF FUNDING NUMBERS	
8b. OFFICE SYMBOL (If applicable) N/C		PROGRAM ELEMENT NO. PROJECT NO. TASK NO. WORK UNIT ACCESSION NO.	
8c. ADDRESS (City, State, and ZIP Code) Building 410 Bolling AFB, DC 20332-6448		612310 2310 A1	
11. TITLE (Include Security Classification) "A Numerical Study of the Role of Meso Beta and Meso Gamma Scale Vertical Exchange Processes in the Evolution of Upper Tropospheric Frontal Systems" (Unclassified)			
12. PERSONAL AUTHOR(S) Kaplan, Michael L.			
13a. TYPE OF REPORT Final Report		13b. TIME COVERED FROM 3/1/86 TO 2/28/90	
14. DATE OF REPORT (Year, Month, Day) 90/4/29		15. PAGE COUNT 89	
16. SUPPLEMENTARY NOTATION N/A			
17. COSATI CODES		18. SUBJECT TERMS (Continue on reverse if necessary and identify by block number)	
FIELD	GROUP	SUB-GROUP	
		Frontogenesis, Turbulence, Numerical Modeling, Mesoscale, Vertical Exchange, Frontolysis, Wind Profiler	
19. ABSTRACT (Continue on reverse if necessary and identify by block number) During the four year research project, several specific areas of knowledge were enhanced in the process of simulating meso-beta and meso-gamma scale frontogenesis and frontolysis. First, a new theory was developed, based on numerical simulations and mesoscale observations, of ageostrophic along-stream frontogenesis. This six-stage process explains how a stratified flow can trigger a sequence of unbalanced nonlinear adjustments which result in an along-stream frontal zone. Second, the effects of nonhydrostatic and turbulent motions on the fronts formed via the mechanism in ageostrophic along-stream frontogenesis was investigated. It was found that the turbulent covariances generated over length scales of ~5-10 km could drastically modify hydrostatic frontogenesis and produce substantial vertical heat and momentum fluxes particularly in dry adiabatic regions which exhibited significant magnitudes of velocity convergence. Third, it was found that both meso-beta scale hydrostatic and meso-gamma scale nonhydrostatic processes accompanying ageostrophic along-stream frontogenesis could produce significant local increases in relative vorticity equivalent to 1-3 times the Coriolis parameter or larger.			
20. DISTRIBUTION/AVAILABILITY OF ABSTRACT <input checked="" type="checkbox"/> UNCLASSIFIED/UNLIMITED <input type="checkbox"/> SAME AS RPT. <input type="checkbox"/> DTIC USERS		21. ABSTRACT SECURITY CLASSIFICATION Unclassified	
22a. NAME OF RESPONSIBLE INDIVIDUAL Lt. Col. James G. Stobie		22b. TELEPHONE (Include Area Code) (202) 767-4963	
		22c. OFFICE SYMBOL N/C	

90 01 25 110

DISTRIBUTION STATEMENT

Unclassified

Approved for public release
Distribution Unlimited

(Block 19 Continued)

over time periods of 1-3 hours and tens of minutes, respectively. The former via the combined tilting and convergence of vorticity during isentropic folding and the latter via tilting and the vertical transport of vorticity during the turbulence caused by ageostrophic frontogenesis. Locally, the potential vorticity was not conserved during the largest nonhydrostatic vertical transport processes resulting in lower tropospheric increases of nearly 300% in 30 minutes during ageostrophic along-stream frontogenesis.

Fourth, generated mass and temperature information directly from wind profiler data to be utilized in the verification of the mesoscale simulation of ageostrophic frontogenesis. This is probably the first observed profiler data which was employed for this purpose.

Fifth, defined the complex nonlinear wave dynamics caused when the Front Range of the Rocky Mountains produces a drag on a jet streak which resulted in ageostrophic along-stream frontogenesis. Simulated and diagnosed the observed dynamics of a leeside standing wave, an inertia-gravity wave forced by leeside shearing instability, and hydraulic jumps all of which contributed to ageostrophic along-stream frontogenesis.

Sixth, produced one of the first, if not the first nonhydrostatic numerical simulations initialized from a fully three-dimensional unbalanced hydrostatic mesoscale circulation.

Seventh, synthesized hydrostatic simulation results, nonhydrostatic simulation results, and observations to better understand the genesis of the dryline and the role of ageostrophic frontogenesis in producing dryline bulges in proximity to regions where tornadic convective storms develop.



Accession For	
NTIS GRA&I	<input checked="checked" type="checkbox"/>
DTIC TAB	<input type="checkbox"/>
Unannounced	<input type="checkbox"/>
Justification	
By	
Distribution/	
Availability Codes	
Dist	Avail and/or Special
A-1	

Research Progress and Forecast Report
(Final Technical Report)

Air Force Office of Scientific Research
Directorate of Chemical and Atmospheric Sciences

Contract # F49620-86-C-0044 - 'A Numerical Study of the Role of Meso-Beta and Meso-Gamma Scale Vertical Exchange Processes in the Evolution of Upper Tropospheric Frontal Systems'

April 29, 1990

Principal Investigator - Dr. Michael L. Kaplan
Program Manager - Lt. Col. James G. Stobie
Point of Contact - Lt. Col. James G. Stobie

(a) Research Objectives :

1. Investigate the impact of the submeso-alpha scale hydrostatic, submeso-beta scale nonhydrostatic, and turbulent exchange of heat and momentum on the distribution of potential vorticity during upper tropospheric frontogenesis and frontolysis.
2. Study the relative magnitude of the hydrostatic, nonhydrostatic, and turbulent exchange of heat and momentum at meso-beta and finer length scales during upper tropospheric frontogenesis and frontolysis as a function of wind shear and static stability.
3. Develop a parameterization scheme for a meso-beta scale numerical model which replicates the subgrid scale vertical exchange of heat and momentum as diagnosed from observed profiler data sets.

(b) Major Research Accomplishments :

During the four year research project there were at least seven clearly defined areas of knowledge which were enhanced by virtue of the numerical, analytical, and observational studies which were performed. In

this section of the report we will briefly describe each of these areas of knowledge. More detailed information can be found in the four papers listed in section (k) submitted for publication in the scientific literature, i.e. Kaplan and Karyampudi a,b,c (1990); Cram et al. (1990).

It should be noted that observed profiler, surface, satellite, and synoptic data sets were analyzed in depth for three case studies, i.e., 13 April 1986, 25 April 1986, and 30 December 1987. Each of these case studies indicated the likelihood of mesoscale frontogenesis to the lee of the Front Range of the Rocky Mountains. However, the numerical simulation experiments involved only the 13 April 1986 case study for two specific reasons: 1) computational resources were finite and 2) this case study contained an extraordinary set of observational signals of the phenomena of interest. The findings discussed in subsequent sections of this report pertain to the numerical, analytical, and observational work performed on the 13 April 1986 case study only.

1. A Theory of Ageostrophic Along-stream Frontogenesis :

In their comprehensive review article, Keyser and Shapiro (1986) indicate that the preponderance of research in frontogenetical processes involve semi-geostrophic theory. Semi-geostrophic theory is totally appropriate when dealing with scales of motion where the wind field is in balance with the mass field and where the length scale of adjustment \gg Rossby radius of deformation:

$$R = \frac{NH}{f} \quad (1)$$

(Gill, 1982) which is typically \gg 500 km. In semi-geostrophic frontogenesis the balanced nature of the flow restricts the frontogenetical or frontolytical dynamics to be in the cross-stream plane where the along-stream component of the geostrophic wind and the cross-stream component of the ageostrophic wind dominate the adjustment processes. The 'stream' being defined as the flow parallel to the largest magnitude geostrophic wind vector. When a mesoscale heating source or perturbation in the mass field is imposed on the 'stream' the scale of adjustment is typically much shorter than the scale of R , hence it is \ll 500 km. Therefore the concept of balanced flow, where the total time tendency of divergence: $[dD/dT] \sim 0$ may not be appropriate. In unbalanced

flow along-stream ageostrophy can become an important mechanism in modifying the structure of baroclinic zones. This flow imbalance is typically forced by: 1) the perturbation of isentropic surfaces during cross-mountain flow, 2) a propagating internal gravity wave, or 3) the release of latent heat accompanying a developing mesoscale convective complex.

In our simulation experiments employing both hydrostatic and nonhydrostatic numerical models with horizontal grid resolutions ranging from 156 to 1.5 km (note Table 1 for a description of simulation experiments) it was evident that as the grid resolution became smaller the role of the along-stream component of the ageostrophic wind in frontogenesis became more important. As a matter of fact, as the grid resolution became smaller, various terrain-induced adjustments greatly perturbed the along-stream ageostrophic wind component. These adjustments included: 1) a region of accelerated upper-tropospheric flow downstream from a large amplitude mountain wave and 2) a propagating inertia-gravity wave triggered by leeslope shearing instability. We were able to define a six-stage dynamical process where a thermal perturbation at the mesoscale resulted in very significant along-stream frontogenesis. While we may not have been the first simulation study to replicate these frontogenetical processes, we are unaware of any published work describing this uniquely mesoscale sequence of dynamical events. This process was not well-resolved until simulations were performed with resolutions ~ 6 km. A basic description of this six-stage process follows.

Stage 1 involves the initial thermal perturbation which could be caused by diabatic heating or the overturning of the isentropic surfaces during the genesis of an internal wave in a shearing stratified flow. The latter genesis mechanism would occur during the development of a large amplitude mountain wave. This is the mechanism which introduces the initial thermal perturbation along the stream.

During stage 2, the increased vertical wind shear accompanying this along-stream pressure perturbation results in the increased vertical variation of the potential temperature with respect to height. This is the result of the new vertical shear imposed upon the fluid by the nonuniform vertical heating resulting in the increased vertical variation of the horizontal advection of potential temperature with respect to height. This literally is analogous to the differential vertical folding of isentropes accompanying the mesoscale ageostrophic shear zone. This acts to modify the vertical variation of potential temperature resulting in nonuniform vertical stratification, i.e., a vertical front is formed.

Stage 3 involves the tilting of this vertical 'front' into the horizontal plane by the significant gradient of vertical motion accompanying the gradient of the along-stream ageostrophic wind component. Here, the vertical exchange processes are clearly crucial in transforming a vertical stratification into a horizontal temperature gradient thus reinforcing the initial thermal perturbation in stage 1.

During stage 4 the new tilting-induced along-stream temperature gradient is sufficiently large to modify the along-stream pressure gradient force and accelerate the wind further. This is analogous to the increase of the isallobaric wind accompanying an amplifying inertia-gravity wave.

Stage 5 involves the continued amplification of the along-stream temperature gradient by the ageostrophic wind through the stretching deformation interacting with the new along-stream front. As the pressure gradient increases and nonuniformly accelerates the flow the along-stream convergence increases the along-stream temperature gradient resulting in an ever-steepening frontal zone. This is the extreme example of nonlinear unbalanced flow as convergence increases the frontogenesis which increases the nonuniform pressure gradient force further intensifying the along-stream ageostrophy.

Finally, nonhydrostatic and turbulent processes prevent a singularity from occurring by modifying the frontal 'collapse' sequence described in stages 1-5. The final stages of this process and sensitivity of frontogenesis terms to the grid mesh employed in the simulation can be seen depicted in Figure 1 and Table 2, respectively. Miller's (1948) frontogenesis equation:

$$\frac{d}{dt} |\nabla_3 \theta|^2 = 2 \vec{F} \cdot \nabla_3 \theta ; \text{ where} \quad (2)$$

$$\vec{F} = \nabla_3 \frac{d\theta}{dt} - (\nabla_3 \vec{V}) \cdot (\nabla_3 \theta)$$

was utilized for these calculations.

2. Nonhydrostatic 'Turbulence' and Its Effects on Frontogenesis

The hydrostatic process defined in the previous subsection establishes an environment where nonhydrostatic vertical exchange processes can modify the structure of the ageostrophic along-stream front. In an effort to simulate the nonhydrostatic adjustments within the front depicted in Figure 1 the nonhydrostatic TASS model (Proctor, 1987a,b) was employed for a nested grid 1.5 km simulation within the initial state provided by the hydrostatic MASS model (Kaplan et al., 1982) simulation which utilized a 6 km grid mesh. The area of coverage of the 135 x 135 matrix employed in the nonhydrostatic simulation (NA), the area of coverage of the hydrostatic simulation (B), and the meso-beta scale region of largest magnitude nonhydrostatic response (NB) are depicted in Figure 2. The nonhydrostatic simulation was performed for one hour of real time and it was initialized at 1400 UTC which was during the period when the process defined in section 1 reached a maximum.

The initial environment which the hydrostatic frontogenesis produced included a meso-beta scale convergence zone superimposed upon an overturning isentropic surface within the middle troposphere as can be seen in Figure 3. This represents an inertia-gravity wave (E3) which is highly frontogenetical within the along-stream plane (FE3). The 10 minute sequenced evolution of TASS-simulated dependent variables depicted in Figure 4 clearly indicate the development of a nonhydrostatic gravity wave (E3a) which has created a dry adiabatic layer in proximity to the horizontal velocity convergence zone. These features are all imbedded within the hydrostatic front. This nonhydrostatic front (FE3a) imbedded within the hydrostatic front is formed by a sequence of events which is similar to those described in subsection 1, however, with the vertical accelerations being on the same order of magnitude as the horizontal accelerations, tilting is a more dominant process when compared to the hydrostatic frontogenesis. As can be seen in Tables 2 and 3, the magnitude of nonhydrostatic frontogenesis is considerably larger than the hydrostatic frontogenetical processes. This new nonhydrostatic front prevents the hydrostatic front from 'collapsing' to a singularity by interrupting the hydrostatic adjustment processes and producing a new along-stream front at a finer length scale and along the downstream periphery of the hydrostatic front.

The nonhydrostatic front becomes the locus of vertical motions exceeding 3 ms^{-1} and gradients of vertical motion exceeding $1 \text{ ms}^{-1}/5 \text{ km}$. As such, the superposition of nonhydrostatic horizontal and vertical accelerations produces regions along the periphery of the nonhydrostatic front where very large correlations exist between the deviations of w ,

theta, u , and v from the mean state. Hence, there are select zones along the periphery of the nonhydrostatic front where turbulent heat and momentum fluxes could become significant. These regions can be seen in the cross sections depicted in Figure 4 where isentropic perturbations as well as strong horizontal variations of w , u , and v are forced below 5 km (AGL) accompanying the nonhydrostatic front.

In an effort to determine how significant these turbulent processes were relative to the hydrostatic and nonhydrostatic adjustments, we averaged each of the four grid square values of dependent variables and their average deviations from the mean from the TASS simulation to produce eddy stresses and eddy heating terms. These were then employed as representative subgrid-scale meso-gamma 'turbulent' processes within the hydrostatic meso-beta scale 6 km simulation. The turbulent contributions to frontogenesis as well as the turbulent heating calculated from the vertical variation of eddy heat flux revealed that the meso-gamma scale turbulence produced highly significant forcing compared to the meso-beta scale processes simulated by the MASS model when employing a 6 km grid mesh. Note, in Tables 2 and 3, that the magnitude of the turbulent contribution to frontogenesis approaches 50% of that due to some of the hydrostatic meso-beta scale forcing functions and is significant relative to the nonhydrostatic frontogenetical forcing functions. Also note that the individual grid point values of turbulent heat flux can exceed magnitudes of $30^{\circ}\text{C}/\text{day}$ although this heating rate occurs for only 10-20 minutes at a given point. Representative patterns of turbulent heat flux and their contribution to frontogenesis can be seen depicted in Figure 5.

The development of the nonhydrostatic along-stream front and the turbulence produced by this front act to prevent any particular scale of motion from becoming the repository of a singularity in the frontal 'collapse' process. Nonhydrostatic 'mean' adjustments such as internal gravity waves which produce fronts within the hydrostatic front interrupt hydrostatic frontogenesis and, hence, prevent the hydrostatic feature from 'collapsing' to a singularity. Where the hydrostatic convergence and dry adiabatic layers superpose accompanying the nonhydrostatic front 'turbulent' adjustments vertically redistribute heat and kinetic energy where the largest magnitude nonhydrostatic gradients exist in order to produce reduced vertical shear and shallower isentropic layers. This research indicates, however, that the processes which organize meso-gamma scale turbulent heat and momentum fluxes are organized by

unbalanced shearing-induced internal gravity waves and that the region of largest vertical exchange is typically where the wave-induced convergence is superpositioned relative to a dry adiabatic layer. Clearly, an understanding of these processes is germane for the forecasting of clear air turbulence and the breakdown of frontogenetical processes.

3. Vorticity and Potential Vorticity Budgets During Hydrostatic and Nonhydrostatic Frontogenesis

The frontogenesis processes described in the previous two subsections involve circulations in which there is a direct interaction between the folding of an isentropic surface and the acceleration of air parcels on that surface by the changing pressure gradient force. That is, the frontogenetical processes produce substantial gradients of pressure on isentropic surfaces within the middle troposphere. Since the pressure gradients change rapidly, the acceleration of air parcels is the result of the change of pressure in time along an isentropic surface. Hence, as the scale of the simulations is reduced and the resolution is increased the magnitude of the convergence on isentropic surfaces and the rapidly changing pressure gradient along the isentropic surface will increase significantly in the same place at the same time. Unlike semi-geostrophic frontogenesis where there is an indirect interaction among the increasing cross-frontal temperature gradient, the pressure gradient force, and the rotational wind field, in mesoscale frontogenesis perturbations in the pressure gradient force can directly influence the dynamics on an isentropic surface through the divergent wind. Hence, during meso-beta and meso-gamma scale frontogenesis the vertical component of the absolute vorticity calculated on a constant pressure surface can change very rapidly due to the SUPERPOSITION of the solenoidal term (tilting) accompanying the isentropic folding (increased temperature gradient) and the convergence term accompanying the acceleration of air parcels by the changing pressure gradient force on the isentropic surface.

The significance of this set of interactions can be seen in Tables 4 and 5 which depict the magnitude of all of the terms in the vorticity equation as a function of simulation as was shown earlier for frontogenesis. The absolute vorticity equation in pressure coordinates being defined in Haltiner and Martin (1957) as:

$$\frac{d\eta}{dt} = -\nabla \cdot \vec{V} (\zeta + f) - \hat{k} \cdot \nabla \omega \times \frac{\partial \vec{V}}{\partial p} + \hat{k} \cdot \nabla \times \vec{F} \quad (3)$$

Clearly evident in this comparison is the dominance of the tilting and convergence terms in the 6 km MASS simulation B. Here, the ageostrophic along-stream front produces such large variations of temperature along pressure surfaces that convergence of vorticity and tilting can produce the 'spinup' of vorticity exceeding values of the Coriolis parameter in one hour as is depicted in Table 6. A comparison between the scale of vorticity forcing functions in simulation C, containing no terrain and a 48 km mesh, and simulation B, containing mountains and a 6 km mesh, reveals the extent to which the ageostrophic along-stream frontogenesis produces vorticity maxima well-downstream from the semi-geostrophic forcing. These spinup and displacement processes are direct indicators of the extent to which the significant variation of pressure along isentropic surfaces have forced horizontal convergence accompanying the ageostrophic meso-beta scale front. Hence, vorticity is produced rapidly and not conserved following a parcel well downstream from the semi-geostrophic processes which are occurring over western Colorado at 1500 UTC in simulation C.

Under these circumstances the overturning isentropic surfaces accompanying the ageostrophic along-stream front are a 'conduit' for parcels high in potential vorticity within the upper troposphere which can be transported surfaceward by the increasing convergent wind velocity accompanying the changing pressure gradient force on a given isentropic surface. Potential vorticity being defined by Keyser and Shapiro (1986) as:

$$\frac{\partial \theta}{\partial p} (\zeta + f) \quad (4)$$

As tilting and convergence accompanying the along-stream front increases in magnitude, air parcels containing upper tropospheric values of potential vorticity are transported on isentropic surfaces into the mid-lower troposphere during the 'spinup' of vorticity. The intersection of a constant pressure surface within the middle troposphere, i.e., 50 kPa with the folded isentropic surface can be inferred from Table 4 which indicates

the maxima of vorticity as a function of resolution. Consistent with the isentropic downfolding, Table 7 and Figure 6 depict graphically the organization of a downstream maximum of potential vorticity and its descent from the upper into the middle troposphere accompanying the ageostrophic along-stream front. This downstream descent is due solely to the conservation of potential vorticity on isentropic surfaces where no mixing has occurred. The same convergence process increasing the absolute vorticity on isentropic and pressure surfaces is accompanying the advection of potential vorticity down an isentropic surface.

However, as nonhydrostatic processes become more important at scales of motion < 10 km the turbulent covariances can produce sources and sinks of potential vorticity. These sources and sinks can be diagnosed from an equation originally formulated by Ertel (1942) and subsequently modified by Gidel and Shapiro (1979) for isentropic coordinates:

$$\frac{d}{dt} \left(\zeta + f \frac{\partial \theta}{\partial p} \right) = -(\zeta + f) \frac{\partial}{\partial p} \left(\frac{d\theta}{dt} \right) + \frac{\partial \theta}{\partial p} \left[\hat{k} \cdot \left(\nabla \frac{d\theta}{dt} \times \frac{\partial \vec{V}}{\partial \theta} \right) \right] - \frac{\partial \theta}{\partial p} \left[\hat{k} \cdot (\nabla \times \vec{F}) \right] \quad (5)$$

In our research we again applied the turbulent covariances from the TASS simulation to diagnose the role of meso-gamma scale 'turbulence', within the periphery of the nonhydrostatic front, on the nonconservation of potential vorticity. Our calculations indicated that over time periods of < 1 hour sources of potential vorticity in excess of $1 \times 10^{-5} \text{ Kmb}^{-1}\text{s}^{-1}$ were simulated by TASS below 70 kPa. These values indicate that magnitudes of potential vorticity typically observed within the upper troposphere can be created by turbulent processes within the lower troposphere underneath the downfolded isentropic surfaces accompanying the ageostrophic along-stream front. These source terms can reach magnitudes in excess of $10^{-8} \text{ Kmb}^{-1}\text{s}^{-2}$ when the turbulent heating is very large, the wind shear on the isentropes is significant, and the eddy fluxes of momentum are likewise significant. This is most likely to occur where a highly convergent or divergent flow is superimposed upon a dry adiabatic layer. The resulting shear-induced nonhydrostatic gravity wave becoming the locus of the nonconservation of potential vorticity. This research also indicates that all three of the terms in equation 5 can contribute a similar order of magnitude to the generation of potential vorticity which differs substantially from the calculations of Keyser and Shapiro (1986) who

relied only on the first term. (Their reliance on this term is totally consistent with their semi-geostrophic theoretical perspective.) As a matter of fact, our simulations indicate that in the region of the largest magnitude nonconservation of potential vorticity between 60 and 70 kPa near FE3am2 term #1 contributed ~17%, term #2 ~26%, and term #3 ~57%. Also, our calculations indicate that the maxima of potential vorticity values in excess of $1 \times 10^{-5} \text{ Kmb}^{-1}\text{s}^{-1}$ below 70 kPa are forced by turbulence accompanying the nonhydrostatic front imbedded within the meso-beta scale front and can be interpreted as the final stage of isentropic overturning resulting in the vertical transport of kinetic energy from the upper troposphere into the planetary boundary layer. These 'bulges' of downward transport of kinetic energy (FE3am1 and FE3am2) are depicted in Figure 7 and the accompanying nonhydrostatic vertical transport of vorticity is depicted in Figure 8 and may be the cause of clear air turbulence and/or dryline intrusions often observed on the upstream side of tornadic convective storms (McGinley, 1973; Tegtmeier, 1974; and Koch, 1979).

4. Generation of Temperature Fields from Mesoscale Wind Profiler Data Sets

In an effort to verify the existence of a mesoscale frontal zone to the lee of the Colorado Front Range, a technique was developed to extract mass information from the profiler wind data sets. This technique is described in depth in Cram et al. (1990). It is based on the concept that the complete divergence equation can be employed to solve for the height field if the three-dimensional wind structure is known. Temperatures can then be hydrostatically derived from height data for use in verifying the mesoscale model simulations. While this approach has been employed in the past with numerical model-generated output (Kuo and Anthes, 1985), this is, to our knowledge, the first time that exclusively observed data sets were utilized to extract the mass information from wind data. This is also the first time that said technique has been utilized to derive features that were truly unbalanced gravity wave phenomena.

To summarize the material in Cram et al. (1990), three sets of experiments were performed to test the technique. The first group of experiments employed MASS model-generated wind data. Surrogate profiler and rawinsonde wind profiles were generated from the MASS wind data in an effort to produce the simulated mesoscale height field. It was

found that highly smoothed height fields derived in this manner closely replicated the MASS model-simulated height structure. In a second set of experiments, it was determined that Dirichlet lateral boundary conditions, requiring only model height data, produced a more realistic height field than did Neumann boundary conditions which required the normal gradient of model height. This was thought to be so because of the increased sensitivity of Neumann boundary conditions to model wind tendencies as opposed to the simpler nature of Dirichlet conditions. Finally, hourly profiler winds were employed to retrieve height and temperature fields using the same technique as in experiments 1 and 2. Figure 9 depicts a comparison between time-interpolated rawinsonde-derived winds and temperatures at 60 kPa between 1030 and 1430 UTC with the same profiler-derived fields. This comparison dramatically indicates the power of this new technique as temperatures derived from the four wind profiler data sets provide clear evidence of a mesoscale frontal zone to the lee of the Front Range. The mesoscale nature of this information is further indicated by the time series depicted in Figure 10 in which midtropospheric height change information derived from the profiler wind data indicates a rapid (mesoscale) pressure change signal analogous to surface data observed over the PROFS mesonetwork between 1400 and 1600 UTC. These profiler-derived mass fields contained sufficient information to help verify hydrostatic simulations of ageostrophic frontogenesis and gravity wave development.

5. Terrain-Induced Gravity Waves To the Lee of the Front Range

Earlier, in this section of the report, we described a theory of ageostrophic along-stream frontogenesis which occurs to the lee of the Front Range of the Colorado Rocky Mountains. In an effort to understand the wave dynamics, forced by the drag on a jet streak traversing the Front Range, that result in conditions favorable for ageostrophic frontogenesis, detailed analyses of the leeslope dynamical processes were performed with both mesoscale observational data sets and MASS-simulated meso-beta scale dependent variables. This analysis produced a highly detailed sequence of wave genesis and amplification processes. These processes are described in depth in Kaplan and Karyampudi (1990 a,b). In this subsection, we will summarize the precursor conditions and nonlinear dynamics both observed and simulated prior to and during ageostrophic frontogenesis. These analyses, in Kaplan and Karyampudi (1990 a,b), represent two possible original contributions to our knowledge of

mesoscale dynamical processes: 1) this is very possibly the first published example of a gravity wave forced by shearing instability within the LOWER troposphere and 2) this is very possibly the first simulation study linking terrain-induced gravity waves during supercritical flow to observed downstream secondary circulations well east of the Front Range.

Prior to and during the development of the terrain-induced ageostrophic along-stream front, mesoscale surface and wind profiler as well as synoptic-scale and satellite observations indicate at least five well-substantiated conclusions concerning the mesoscale state of the atmosphere between 0600 and 1800 UTC 13 April 1986 over the region including central and eastern Colorado.

1) A well-defined stratified shearing profile including substantial decreases in the Scorer Parameter with height existed above the Front Range during the early part of this time period which should contribute to the development of internal waves. The prewave temperature, wind, and Scorer Parameter profiles indicating a superpositioned inversion and shearing profile over the Front Range are depicted in Figures 11-13.

2) Surface wind maxima occur shortly after the development of the stratified shearing flow over the Front Range. These maxima are evident in the PROFS mesonetwork surface data time sections for stations BOU, ERI, and BRI just east of the Front Range depicted in Figure 14.

3) A mesoscale surface pressure perturbation develops ahead of the Pacific cold front and is nearly coincident with the onset of high surface winds at leeward observing stations also depicted in Figure 14.

4) The mesoscale surface pressure perturbation coherently propagates across Colorado to at least the Kansas and Nebraska borders during the latter part of this time period, i.e., 1400-1700 UTC as is depicted in Figure 10.

5) Significant wind velocity perturbations as diagnosed from four wind profilers indicate that high frequency velocity increases and decreases are nearly coincident with the propagation of the surface pressure perturbation across eastern Colorado between 1400 and 1700 UTC. These wind profiler time sections are depicted in Figure 15.

The complex wave dynamics accompanying these observations can only be understood by meso-beta scale numerical simulations employing realistic initial data, terrain, and boundary conditions. The results of these numerical simulations utilizing a 6 km version of the MASS model over a 250 x 250 x 20 matrix of grid points are depicted in Figures 16-20. These simulation results support an orderly sequence of processes which are forced by the drag on the jet streak's shearing stratified atmosphere by the Colorado Front Range. These processes result in a secondary jet streak, propagating inertia-gravity wave, and an ageostrophic along-stream front accompanying the gravity wave whose developmental sequence is summarized below.

- 1) A synoptic-scale stratified shearing atmosphere with an upper-level jet stream nearly perpendicular to the Front Range produces a supercritical flow under a low-level inversion. This is depicted at 0600 UTC in Figure 16.
- 2) A large amplitude mountain wave develops over the Front Range producing the generation of divergent kinetic energy at upper levels downstream from the Front Range as well as downward vertical momentum fluxes along the immediate lee slope. The wave and momentum perturbations during the 0600-0900 UTC period are depicted in Figure 16.
- 3) Hydraulic jumps at the base of and downstream from the Front Range redistribute the divergent kinetic energy and vertical stability. This is evident from Figure 17 for the 0900-1000 UTC time period.
- 4) As a result of this redistribution of divergent kinetic energy and vertical stability, a low-level unstable layer and a relatively stable layer in the middle troposphere produces a Scorer Parameter structure east of the Front Range conducive for a wave duct (Lindzen and Tung, 1976) near the critical level. This duct becomes well-established in Figure 17 by 1100 UTC.
- 5) By 1100 UTC, vertical shearing instability (Stobie et al., 1983; Koch and Dorian, 1988) just east of the Front Range produces an inertia-gravity wave within the duct above the critical level. This internal wave becomes evident by 1200 UTC in Figure 17.
- 6) Vertical momentum flux by the inertia-gravity wave as it propagates

eastward across the profiler network produces the downward extension of the secondary jet stream. This sequence of events over eastern Colorado between 1200 and 1500 UTC is depicted in Figure 18. It is evident from this Figure that the phasing of the inertia-gravity wave in the vertical reflects the multilayer atmospheric structure by tilting first upstream above the boundary layer and later downstream within the upper troposphere. The dual Fourier modes associated with the propagating gravity wave become better phased in the vertical resulting in the reduced dispersion of energy in time. Furthermore, the surface pressure trace simulated by the MASS model over the same region is depicted in Figure 19 indicating a pressure perturbation which propagates eastward ahead of the Pacific cold front.

Finally, the scale dependence inherent in these processes is highlighted in Figure 20 which compares the response of a 48 km grid mesh simulation with no terrain, a 24 km simulation with terrain, and this 6 km simulation with terrain over the same region at the same time. It is evident that the secondary circulation is only resolved in the 6 km simulation. Thus it allows us to view the result of mountain drag on a stratified atmosphere well downstream from the barrier.

6. Nonhydrostatic Nested-Grid Simulation Within a Hydrostatic Simulation

Earlier we discussed the role of nonhydrostatic adjustments in modifying the sequence of processes resulting in frontal 'collapse'. These adjustments were simulated by the TASS model which was initialized from interpolated three-dimensional dependent variables produced by the 6 km MASS simulation. This is very possibly the first nonhydrostatic, truly meso-gamma scale simulation initialized with fully varying three-dimensional initial fields which include an ongoing meso-beta scale circulation. This one hour simulation proved that the internal adjustments produced by the nonhydrostatic model did not result in an incoherent sequence of dependent variables when the model was initialized with highly unbalanced mesoscale gravity wave phenomena. It should be noted that no additional smoothing or major modifications to the boundary conditions were enforced for this TASS simulation. An additional advantage of performing this simulation was that one may better understand how hydrostatic circulations establish the meso-gamma scale environment to 'trigger' convection as opposed to employing unrealistically-intense local 'bubble' heat sources which are typically

utilized in nonhydrostatic simulation experiments.

7. Possible Coupling Between Mesoscale Simulations and The Dryline in the Preconvective Environment

It has long been recognized that a well-defined boundary known as the 'dryline' separates dry air of continental origin and moist air of maritime tropical origin to the immediate upstream side of intense, often tornadic, convective storms (Koch and McCarthy, 1982). Such a feature was observed to develop over eastern Colorado, western Kansas, and southwestern Nebraska during the period after 1500 UTC 13 April 1986. This period coincides with (1) the meso-beta and nonhydrostatic simulations discussed earlier in this report, (2) the profiler-derived and PROFS mesonetwork-derived observations also discussed earlier, and (3) is just six hours before the first in a series of tornadic convective storms is observed over central Nebraska and Kansas. It was also reported by McGinley (1973), Tegtmeier (1974), and Koch (1979) that tornadic convective storms typically form along so-called 'bulges' in the dryline accompanying regions of large downward momentum transport.

There are at least three aspects to the process of dryline formation which are simulated by the 6 km MASS and the TASS models which are terrain-induced and are intimately coupled to ageostrophic along-stream frontogenesis. First, as indicated in Figure 16, the downstream hydraulic jump (E2) simulated by MASS between 0600 and 0900 UTC produces a surface pressure perturbation which becomes the locus of dryline formation. Second, the 6 km MASS simulation produces the ageostrophic along-stream front depicted in Figure 1 (FE3) which is just upstream from the simulated 1500 UTC surface dryline position depicted in Figure 21. Third, the TASS simulation produces features accompanying the nonhydrostatic front (FE3a) which are formed by the vertical transport of kinetic energy at nonhydrostatic length scales (FE3am1 and FE3am2) which are very similar in structure and location relative to the dryline 'bulges' observed by McGinley (1973), Tegtmeier (1974), and Koch (1979). These bulges are depicted in Figure 22. It is quite apparent from this figure, earlier figures, and Figure 21 that there is an intriguing juxtaposition among the observed dryline, the simulated dryline, the observed surface vorticity, the observed profiler-derived wind maxima, the simulated dryline bulges, the simulated hydrostatic ageostrophic

along-stream front, and the observed tornadoes all of which occur over northeastern Colorado, southwestern and southcentral Nebraska, and northwestern and northcentral Kansas between 1500 and 2300 UTC 13 April 1986. It is interesting that in the most recent issue of Monthly Weather Review (Martin et al., 1990) that investigators are finding evidence linking dryline formation to the effects of the Rocky Mountains on the atmosphere. The findings in our research strongly suggest that this coupling is indeed occurring in nature.

(c) Publications:

The following journal articles either have been submitted for publication or are in the process of being prepared for submission:

1) Kaplan, M. L., and V. M. Karyampudi, 1990: Mesoscale Perturbations in the Jet Stream Forced by the Rocky Mountains Part I: Analyses of a Hydraulic Jump and an Inertia-Gravity Wave. In preparation for submission to the Journal of Atmospheric Sciences.

2) Kaplan, M. L., and V. M. Karyampudi, 1990: Mesoscale Perturbations in the Jet Stream Forced by the Rocky Mountains Part II: Numerical Simulations of a Downslope Windstorm, Hydraulic Jump, and an Inertia-Gravity Wave. In preparation for submission to the Journal of Atmospheric Sciences.

3) Kaplan, M. L., and V. M. Karyampudi, 1990: Mesoscale Perturbations in the Jet Stream Forced by the Rocky Mountains Part III: Three-Dimensional Numerical Simulations of Terrain-Induced Ageostrophic Along-Stream Frontogenesis. In preparation for submission to the Journal of Atmospheric Sciences.

4) Cram, J. M., M. L. Kaplan, C. A. Mattocks, and J. W. Zack, 1990: The Analysis and Use of Profiler Winds to Derive Mesoscale Height and Temperature Fields; Simulation and Real Data Experiments. Submitted to Monthly Weather Review.

The following conference papers have been presented and appear in the conference preprint volumes:

1) Kaplan, M. L., C. A. Mattocks, J. W. Zack, and M. D. Bousquet, 1987: A

Numerical Simulation of Meso-Beta Scale Midtropospheric Frontogenesis Resulting From The Interaction Between a Jet Streak and a Mountain Range. Presented at the XIX IUGG General Assembly Meeting, Vancouver, B. C. (Also presented at a symposium at this meeting entitled: Mesoscale Analysis and Forecasting, Incorporating Nowcasting).

2) Kaplan, M. L., 1988: A Numerical Simulation of Leaside Frontogenesis-Mountain Wave Development and its Implications for Convective Storm Initiation. Presented at the Eighth Conference on Numerical Weather Prediction, Baltimore, Md., J59-J66.

3) Cram, J. M., M. L. Kaplan, C. A. Mattocks, and J. W. Zack, 1988: The Use of Profiler Winds to Derive Mesoscale Height and Temperature Analyses. Presented at the Eighth Conference on Numerical Weather Prediction, Baltimore, Md., 339-345.

4) Kaplan, M. L., and V. Mohan Karyampudi, 1990: Mesoscale Perturbations in the Jet Stream Forced by the Rocky Mountains Part I: Numerical Simulations of Perturbations Forced by a Mountain Wave. To be presented at the Fourth Conference on Mesoscale Processes, Boulder, Co.

(d) Professional Personal:

- 1) Dr. M. L. Kaplan, Senior Research Scientist, Principal Investigator
- 2) Dr. J. W. Zack, Senior Research Scientist
- 3) Dr. V. M. Karyampudi, Research Scientist
- 4) J. M. Cram, Research Scientist/Consultant
- 5) P. E. Price, Research Scientist/Scientific Programmer
- 6) M. D. Bousquet, Scientific Programmer
- 7) Dr. C. A. Mattocks, Research Scientist
- 8) Dr. F. H. Proctor, Senior Research Scientist
- 9) Dr. K. H. Waight III, Research Scientist

(e) Interactions (Coupling Activities):

There were four researchers with whom significant scientific interactions occurred during the four year period of this contract. First, Professor Dale Durran of the University of Washington. Prof. Durran provided valuable input concerning the fidelity of the mountain wave

simulations produced by the MASS model and the intricacies of the dynamical processes they represent. Second, Professor David Houghton of the University of Wisconsin. Prof. Houghton aided greatly in our understanding of the hydraulic jump phenomena and low-level leeside shearing instability produced by the MASS model. Third, Dr. Steven Koch, of the NASA Goddard Laboratory for Atmospheres, was a source of valuable information concerning the characteristics of the observed and simulated gravity waves and he also reviewed the manuscripts submitted for publication. Fourth, Professor Yuh-Lang Lin of North Carolina State University was also a source of valuable information concerning the wave evolution to the lee of the Front Range and he also served as a reviewer of the manuscripts submitted for publication. Furthermore, we presented these results in a seminar to scientists at the NASA Goddard Laboratory for Atmospheres and North Carolina State University's Department of Marine, Earth, and Atmospheric Sciences.

(f) New Discoveries:

There were several physical phenomena whose genesis and evolution are much better understood as a result of this research project.

First, the process of ageostrophic along-stream frontogenesis. Heretofore, frontogenesis theory was largely limited to semi-geostrophic theory thus largely eliminating the role of the along-stream deviations from geostrophic balance on the evolution of fronts. By simulating the effects of large amplitude hydrostatic and nonhydrostatic gravity waves on frontogenesis, it is now possible to understand how fronts form which are perpendicular to, not parallel to, the jet stream at elevations which are directly decoupled from the surface frictional and diabatic forcing.

Second, the manner in which nonhydrostatic internal gravity waves form within along-stream fronts. The internal gravity wave, which is simulated by TASS within the ageostrophic front, is significant because it serves as a region of concentrated adiabatic expansion which could serve as a triggering mechanism for convection and because it establishes very large gradients of vertical velocity in proximity to gradients of temperature and horizontal velocity thus organizing turbulence. This may be a very prevalent mechanism for the organization of clear air turbulence.

Third, the phenomena of low-level shearing instability accompanying the leeslope vertical momentum transport is very likely a new discovery. Here, the proximity of low Richardson numbers accompanying shearing

unstable flow to a leeside critical level just above the terrain surface results in the generation of an inertia-gravity wave which propagates well downstream from its genesis position. In previous studies, gravity wave genesis through shearing instability was relegated to the levels of largest magnitude jet stream velocity shears typically within the upper troposphere.

Fourth, the hydraulic jump which is simulated by the MASS model downstream from the Front Range produces a surface pressure perturbation which results in the development of a surface dryline boundary. While people have associated dryline development with terrain-induced forcing, this may be the first time that the details of this coupling could be specified. Eventually, the downward momentum transport accompanying the along-stream front captures this surface perturbation and amplifies it.

Fifth, the evolution of the dryline after it has been organized by the hydraulic jump discussed in the previous paragraph is a function of downward momentum transport. The nonhydrostatic TASS simulation nested within the hydrostatic MASS simulation produces substantial magnitudes of downward momentum transport within meso-gamma scale regions. These meso-gamma scale regions $\sim 10 \times 10$ km lie within the volume of air in proximity to the surface dryline. These regions of vertical momentum transport between the middle troposphere and the PBL act to produce inhomogenities or 'bulges' within the dryline which serve as regions of maxima of vorticity. Again, while people have largely speculated about the process which produces these dryline 'bulges' because of limited data or inadequate theories, the simulations produce a new coherent sequence of dynamical processes which can explain the development of said phenomena. The process of dryline bulge formation is the same process accompanying nonhydrostatic frontogenesis which results in clear air turbulence.

Sixth, while experiments have been performed in an effort to retrieve mass information from wind information employing model-simulated internally consistent 'surrogate wind profiler' data sets, to our knowledge there has been no published work which indicated that coherent mesoscale height fields have been derived from an observational network of wind profilers. This represents two firsts because not only has the technique been proven feasible, but also a mesoscale feature, i.e., a leeslope front, has been retrieved from the wind profiler data verifying the existence of a simulated mesoscale feature.

Seventh, while many mountain wave simulation experiments have been performed which indicate the vertical flux of horizontal momentum, little published work has been performed on the downstream generation of kinetic energy accompanying mountain wave formation and the consequences for the structure of the jet stream.

All seven of these 'discoveries' represent pieces of the puzzle of why such extraordinary weather phenomena occur to the lee of major mountain barriers. These terrain-induced circulations are very likely responsible, at least in part, for the spectrum of violent mesoscale weather phenomena which occur over the central United States. Hence, what has been learned in this research study could be most applicable to studies of phenomena observed during the forthcoming Storm Central Program.

(g) Software Development:

It should be noted that a large portion of year three of this contract was devoted to transferring the MASS and TASS models as well as all of the pre and postprocessing software from the NASA Langley VPS-1 supercomputer system to the Air Force Weapons Laboratory Cray-2 supercomputer system. This effort was mandated by the contract monitor and it required many person-months and, hence, precluded some of the planned research tasks. It also represented, however, an extraordinary opportunity to utilize the Cray-2 supercomputer's extraordinary speed and memory at very low computational cost.

(h) References:

Ertel, H., 1942: Ein neuer hydrodynamischer Wirbelsatz. *Meteor. Z.*, **59**, 277-281.

Gidel, L. T., and M. A. Shapiro, 1979: The role of clear air turbulence in the production of potential vorticity in the vicinity of upper-tropospheric jet stream frontal systems. *J. Atmos. Sci.*, **36**, 2125-2138.

Gill, A. E., 1982: 'Atmosphere-Ocean Dynamics', Academic Press, New York, N. Y., 662 pp.

Haltiner, G. J., and F. L. Martin, 1957: 'Dynamical and Physical Meteorology', McGraw-Hill, New York, N. Y., 470 pp.

Kaplan, M. L., J. W. Zack, V. C. Wong, and J. J. Tuccillo, 1982: Initial results from a mesoscale atmospheric simulation system and comparisons with the AVE-SESAME I data set. *Mon. Wea. Rev.*, **110**, 1564-1590.

Keyser, D., and M. A. Shapiro, 1986: A review of the structure and dynamics of upper-level frontal zones. *Mon. Wea. Rev.*, **114**, 452-499.

Koch, S. E., 1979: Mesoscale gravity waves as a possible trigger of severe convection along a dryline. Ph. D. Thesis, University of Oklahoma, 195 pp.

_____, and J. McCarthy, 1982: The evolution of an Oklahoma dryline. Part II: Boundary layer forcing of meso convective systems. *J. Atmos. Sci.*, **39**, 237-257.

_____, and P.J. Dorian, 1988: A mesoscale gravity wave event observed during CCOPE. Part III: Wave environment and possible source mechanisms. *Mon. Wea. Rev.*, **116**, 2527-2544.

Kuo, Y-H, and R. A. Anthes, 1985: Calculation of geopotential and temperature fields from an array of nearly continuous wind observations. *J. Atmos. Oceanic. Technol.*, **2**, 22-34.

Lindzen, R.S., and K.-K. Tung, 1976: Banded convective activity and ducted gravity waves. *Mon. Wea. Rev.*, **104**, 1602-1617.

Martin, J. E., J. D. Locatelli, and P. V. Hobbs, 1990: Organization and structure of clouds and precipitation on the Mid-Atlantic coast of the United States. Part III: The evolution of a middle tropospheric cold front. *Mon. Wea. Rev.*, **118**, 195-217.

McCarthy, J. and S. E. Koch, 1982: The evolution of an Oklahoma dryline. Part I: A meso-and subsynoptic-scale analysis. *J. Atmos. Sci.*, **39**, 225-236.

McGinley, J., 1973: Environmental energy fields associated with severe storms. M. S. Thesis, University of Oklahoma, Norman, Oklahoma, 130 pp.

Miller, J. E., 1948: On the concept of frontogenesis. *J. Meteor.*, **5** 169-171.

Proctor, F. H., 1987a: 'The Terminal Area Simulation System. Volume I: Theoretical Formulation'. NASA Contractor Rep. 4046, NASA, Washington, D.C., 176 pp.

_____, 1987b: 'The Terminal Area Simulation System. Volume II: Verification Experiments'. NASA Contractor Rep. 4047, NASA, Washington, D. C., 112 pp.

Stobie, J.G., F. Einaudi, and L.W. Uccellini, 1983: A case study of gravity waves - convective storms interaction: 9 May 1979. *J. Atmos. Sci.*, **40**, 2804-2830.

Tegtmeier, S. A., 1974: The role of the surface subsynoptic low pressure system in severe weather forecasting. M. S. Thesis, University of Oklahoma, Norman, Oklahoma, 65 pp.

(i) List of Tables:

1. Specifications of Numerical Model Simulations Employed in Papers I, II, and III
2. 1500 UTC Maxima of Frontogenesis Equation Terms Among All Simulations (Over Profiler Network)
3. TASS-Simulated Frontogenesis Equation Terms
4. 1500 UTC Maxima of Vorticity Equation Terms Among All Simulations (Over Profiler Network)
5. TASS-Simulated Vorticity Equation Terms
6. 'Spinup' Factors Among Simulations
7. Highest Pressure of the Potential Vorticity Values Exceeding $1.0 \times 10^{-5} \text{ Kmb}^{-1}\text{s}^{-1}$ as a Function of Simulation and West-East Location at 1500 UTC

(j) List of Figures:

1. MASS simulation B 50 kPa temperature ($^{\circ}\text{C}$) valid at (a) 1200 UTC, (b) 1300 UTC, (c) 1400 UTC, and (d) 1500 UTC 13 April 1986. Superposition of MASS simulation B maximum acceleration vector (black vector), maximum of 50 kPa Laplacian of height term (solid), maximum of 50 kPa convergence forcing function in Miller's (1948) equation (large dashed), and maximum of 50 kPa total frontogenesis function in Miller's (1948) equation (stippled) all on the MASS simulation B 50 kPa temperature ($^{\circ}\text{C}$) (thin dashed) and valid at (e) 1200 UTC, (f) 1300 UTC, (g) 1400 UTC, and (h) 1500 UTC 13 April 1986. Large white vector on (e)-(h) represents 1500 UTC geostrophic 'stream' vector.

2. (a) Geographical location of the TASS model domain (NA) and TASS model domain subregion of nonhydrostatic 'turbulence' accompanying FE3a (stippled) (NB) and (b) its location relative to the MASS model simulation B domain. Dashed line in (a) represents the location of the cross sections displayed in Figures 3 and 4 at $Y=-10$ km.

3. TASS west-east cross sections at $Y=-10$ km of initial data from MASS simulation B (a) potential temperature (K), (b) u wind velocity component isotachs (ms^{-1}), (c) v wind velocity component isotachs (ms^{-1}), and (d) w wind velocity component (ms^{-1}) all valid at 1400 UTC 13 April 1986. Height of data is relative to ground level.

4. TASS-simulated west to east cross sections at $Y=-10$ km of potential temperature (K), (a,b,c,d,e,f), u wind velocity component isotachs (ms^{-1}) (g,h,i,j,k,l), v wind velocity component isotachs (m,n,o,p,q,r), and w wind velocity component isotachs (s,t,u,v,w,x) all valid at 1410 UTC, 1420 UTC, 1430 UTC, 1440 UTC, 1450 UTC, and 1500 UTC 13 April 1986. Height of data is relative to ground level. Stippled regions on 1500 UTC wind velocity component cross sections represent areas of nonconservation of potential vorticity.

5. TASS-simulated turbulence forcing function in Miller's (1948) equation centered on 50 kPa in $\text{Km}^{-2}\text{s}^{-2} \times 10^{13}$ valid at (a) 1410 UTC, (b) 1420 UTC, (c) 1430 UTC, (d) 1440 UTC, (e), 1450 UTC, and (f) 1500 UTC 13 April 1986 and TASS-simulated 50 kPa eddy heat flux ($\text{Ks}^{-1} \times 10^6$) valid at (g) 1410

UTC, (h) 1420 UTC, (i) 1430 UTC, (j) 1440 UTC, (k) 1450 UTC, and (l) 1500 UTC 13 April 1986 and displayed over NB, and TASS-simulated 50 kPa temperature (K) valid at (m) 1410 UTC, (n) 1420 UTC, (o) 1430, (p) 1440 UTC, (q) 1450 UTC and (r) 1500 UTC 13 April 1986. All maxima and minima regions on 1440 UTC, 1450 UTC, and 1500 UTC 50 kPa eddy heat flux figures represent highest magnitude areas, i.e., $\sim 10^{-8} \text{ Kmb}^{-1}\text{s}^{-2}$, of the nonconservation of potential vorticity as defined in Ertel's (1942) equation.

6. MASS simulation C (a) and simulation A1 (b) potential vorticity on the 310 K isentropic surface in $\text{Kmb}^{-1}\text{s}^{-1} \times 10^7$ for simulation C and $\text{Kmb}^{-1}\text{s}^{-1} \times 10^6$ for simulation A1 and both valid at 1500 UTC 13 April 1986. MASS simulation B potential vorticity ($\text{Kmb}^{-1}\text{s}^{-1} \times 10^5$) cross sections valid at (c) 0900 UTC and (d) 1200 UTC between Craig, Colorado (CAG) and Grand Island, Nebraska (GRI) and valid at (e) 1300 UTC, (f) 1400 UTC, and (g) 1500 UTC between the Front Range and Fleming, Colorado (FLM) on 13 April 1986.

7. TASS-simulated 50 kPa ($\sim 4.2 \text{ km AGL}$) wind velocity vectors and isotachs (ms^{-1}) valid at 1500 UTC 13 April 1986 and displayed over (a) NA and (b) NB.

8. TASS-simulated 50 kPa vertical advection of absolute vorticity ($\text{s}^{-2} \times 10^9$) valid at 1500 UTC 13 April 1986 over NB.

9. Profiler-derived 60 kPa temperature (K) (a,b) and wind vectors and isotachs (ms^{-1}) (c,d) valid at 1030 UTC and 1430 UTC 13 April 1986. Rawinsonde-derived comparisons obtained from linear time interpolation for these same four fields are depicted in panels e, f, g, and h.

10. (a) Derived height change at 600 mb (m) and wind velocity (ms^{-1}) from profilers at the center analysis point between 1030 and 1930 UTC 13 April 1986. (b) Observed surface pressure traces (mb) at PROFS mesonetwork stations from 1200-1700 UTC 13 April 1986.

11. Composite temperature soundings ($^{\circ}\text{C}$) constructed from five high terrain mesonetwork surface observations for the layer between 1600 and 3500 m for each hour during the period from (a)-(g) 0600-1200 UTC 13

April 1986.

12. Composite U and V wind component velocity profiles (ms^{-1}) constructed from five high terrain mesonetwork surface observations for the layer between 1600 and 3500 m for each hour during the period from (a)-(g) 0600-1200 UTC 13 April 1986.

13. Composite Scorer Parameter profiles (m^{-2}) constructed from five high terrain mesonetwork surface observations for the layer between 1600 and 3500 m for each hour during the period from (a)-(g) 0600-1200 UTC 13 April 1986.

14. Time sections of superimposed mesonetwork observed mean sea level pressure ($\text{kPa} \times 10$) and surface wind velocity (ms^{-1}) (bottom) and superimposed mesonetwork surface temperature ($^{\circ}\text{C}$) and surface dewpoint ($^{\circ}\text{C}$) (top) for stations (a) BOU, (b) ERI, and (c) BRI for the time period from 1200 to 2200 UTC 13 April 1986.

15. Time versus height sections of observed profiler-derived wind velocity (ms^{-1}) for the period from 0030 UTC 13 April 1986 to 0030 UTC 14 April 1986 valid at (a) Platteville, Colorado, (b) Denver, Colorado, (c) Fleming, Colorado, and (d) Flagler, Colorado. (e) Observed profiler-derived values for the vertical component of the absolute vorticity ($\text{s}^{-1} \times 10^5$) at the 6 km level valid at 1430 UTC 13 April 1986. Station wind vectors are in ms^{-1} with a full barb equal to 10 ms^{-1} and a half barb equal to 5 ms^{-1} .

16. MASS model-simulated (B) potential temperature (K) along the cross section from near Craig, Colorado to near Grand Island, Nebraska valid at (a) 0600 UTC, (b) 0700 UTC, (c) 0800 UTC, and (d) 0900 UTC 13 April 1986 and MASS model-simulated (B) wind velocity (ms^{-1}) along the cross section from near Craig, Colorado to near Grand Island, Nebraska valid at (e) 0600 UTC, (f) 0700 UTC, (g) 0800 UTC, and (h) 0900 UTC 13 April 1986.

17. MASS model-simulated (B) potential temperature (K) and omega ($\text{kPa s}^{-1} \times 10^4$) along the cross section from near the top of the Front Range to extreme eastern Colorado valid at (a) 0900 UTC, (b) 1000 UTC, and (c) 1100 UTC 13 April 1986. MASS model-simulated (B) wind velocity (ms^{-1}) along the cross section from near the top of the Front Range to extreme eastern Colorado valid at (d) 0900 UTC, (e) 1000 UTC, and (f) 1100 UTC 13

April 1986. Points 154, 157, 160, 163, 166, 169, and 172 refer to locations 6, 24, 42, 60, 78, 96, and 114 km downstream from the start of the Front Range, respectively. The stippling on the potential temperature and omega cross sections mark the location of simulated Richardson number values less than 1.0 for the entire model atmosphere. The stippling on the wind velocity cross sections mark the location of simulated downward momentum flux values in excess of $.002 \text{ kgm}^{-1}\text{s}^{-2}$ for the 30-70 kPa layer. DUCT refers to the gravity wave duct and CLVL to the critical level. The number in parentheses to the right of the 50 kPa represents the maximum static stability within the DUCT in Kkm^{-1} and the maximum vertical wind shear within the DUCT in $\text{ms}^{-1}\text{km}^{-1}$ for the theta and wind cross sections, respectively.

18. MASS model-simulated (B) potential temperature (K) and omega ($\text{kPa s}^{-1} \times 10^4$) along the cross section from near the top of the Front Range to extreme eastern Colorado valid at (a) 1200 UTC, (b) 1300 UTC, (c) 1400 UTC, and (d) 1500 UTC 13 April 1986. MASS model-simulated (B) wind velocity (ms^{-1}) along the cross section from near the top of the Front Range to extreme eastern Colorado valid at (e) 1200 UTC, (f) 1300 UTC, (g) 1400 UTC, and (h) 1500 UTC 13 April 1986. Positions 154-172, DUCT, CLVL, (), and stippling as in Fig. 17.

19. MASS model-simulated (B) 30 minute interval time sections of surface pressure - the model upper boundary pressure (π in $\text{kPa} \times 10$) at grid points along the 40 deg N latitude line approximately (a) 6 km, (b) 24 km, (c) 42 km, (d) 60 km, (e) 78 km, and (f) 96 km from the start of the Front Range valid from 1200 to 1800 UTC 13 April 1986.

20. MASS model-simulated 50 kPa height (m) and vertical component of absolute vorticity ($\text{s}^{-1} \times 10^5$) valid at 1500 UTC 13 April 1986 employing simulations (a) C, (b) A2, and (c) B, MASS model-simulated 50 kPa wind vectors and isotachs (ms^{-1}) valid at 1500 UTC 13 April 1986 employing simulations (d) C, (e) A2, and (f) B, MASS model-simulated wind velocity (ms^{-1}) along the cross section from near Craig, Colorado to near Grand Junction, Colorado valid at 1500 UTC 13 April 1986 when employing simulations (g) C, (h) A2, and (i) B, and MASS model-simulated mean sea level pressure ($\text{kPa} \times 10$) valid at 1800 UTC 13 April 1986 employing simulations (j) C, (k) A2, and (l) B. PGF refers to the direction in which the

x-space component of the pressure gradient force is acting.

21. MASS model-simulated 50 kPa sigma level 1 dewpoint ($^{\circ}\text{C}$) valid at 1500 UTC 13 April 1986.

22. Locations and times of development of 1) the 1500 UTC TASS-simulated dryline bulges (FE3am1 and FE3am2 below horizontal arrows), 2) the 1500 UTC and 1800 UTC observed positions of the dryline (designated as the 8°C surface dewpoint temperature line in thick dashed lines), 3) the 1800 UTC observed surface absolute vorticity (thin dashed lines in $\text{s}^{-1} \times 10^5$), 4) the observed position of profiler-derived middle-upper tropospheric wind and absolute vorticity maxima between 1300 and 1700 UTC (FLM and FLG), 5) the radar-derived location of the genesis of mesoscale convective complex systems between 1835 UTC and 0035 UTC (stippled), and 6) the subsequent location of confirmed tornadoes and funnel clouds between 2112 and 0008 UTC (slanted arrows). All times are for the period between 1300 UTC 13 April 1986 and 0035 UTC 14 April 1986.

(k) List of Journal Articles Prepared During this Research Project:

A - Mesoscale Perturbations in the Jet Stream Forced by the Rocky Mountains Part I: Analyses of a Hydraulic Jump, and an Inertia-Gravity Wave. M. L. Kaplan and V. M. Karyampudi. In preparation for submission to the Journal of Atmospheric Sciences, 1990.

B - Mesoscale Perturbations in the Jet Stream Forced by the Rocky Mountains Part II: Numerical Simulations of a Downslope Windstorm, Hydraulic Jump, and an Inertia-Gravity Wave. M. L. Kaplan and V. M. Karyampudi. In preparation for submission to the Journal of Atmospheric Sciences, 1990.

C - Mesoscale Perturbations in the Jet Stream Forced by the Rocky Mountains Part III: Three-Dimensional Numerical Simulations of Terrain-Induced Ageostrophic Along-Stream Frontogenesis. M. L. Kaplan and V. M. Karyampudi. In preparation for submission to the Journal of Atmospheric Sciences, 1990.

D - The Analysis and Use of Profiler Winds to Derive Mesoscale Height and

Temperature Fields: Simulation and Real Data Experiments. J. M. Cram, M. L. Kaplan, C. A. Mattocks, and J. W. Zack. Submitted to Monthly Weather Review, 1990.

TABLE 1

SPECIFICATIONS OF NUMERICAL MODEL SIMULATIONS EMPLOYED IN
PAPERS I, II, AND III

<u>SIMULATION</u>	<u>HORIZONTAL MESH (KM)</u>	<u>VERTICAL LAYERS</u>	<u>TERRAIN</u>	<u>HYDROSTATIC</u>	<u>PERIOD (HOURS)</u>
S	156	14	YES	YES	24
C	48	14	NO	YES	24
A1	48	14	YES	YES	24
A2	24	20	YES	YES	24
B	6	20	YES	YES	18
G	1.5	20	NO	NO	1

/

TABLE 2

1500 UTC MAXIMA OF FRONTOGENESIS EQUATION TERMS
AMONG ALL SIMULATIONS
(ALL OVER PROFILER NETWORK EXCEPT FOR SIMULATION C)

<u>TERM</u>	<u>SIMULATION</u>				
	C	A1	A2	B	G
VERSHR	3.2	40	30	2970	9530
CONV	4.4	40	133	1680	14800
TILT	2.4	35	50	710	4190
HORSHR	.4	20	40	410	7270
TOTFRT	.014	.07	.15	2.1	3.3

M1 - FE3AM1, M2 - FE3AM2, VERSHR - VERTICAL SHEARING TERM, CONV- CONVERGENCE TERM, TILT - TILTING TERM, HORSHR - HORIZONTAL SHEARING TERM, TURB - TURBULENCE TERM, TOTFRT - TOTAL FRONTOGENESIS. ABSOLUTE VALUES OF ALL TERMS IN $\text{KM}^{-1}\text{S}^{-1} \times 10^{10}$. TOTFRT IN $\text{K}^2\text{M}^{-2}\text{S}^{-1} \times 10^{11}$ DOES NOT INCLUDE TURBULENCE FORCING FUNCTION.

TABLE 3

TASS-SIMULATED FRONTOGENESIS EQUATION TERMS

TERM	TIME (UTC)											
	1410		1420		1430		1440		1450		1500	
	M1	M2	M1	M2	M1	M2	M1	M2	M1	M2	M1	M2
VERSHR	83	85	-186	-130	-576	878	599	953	464	704	594	501
CONV	150	200	599	587	900	604	1480	740	1250	790	-387	739
TILT	-101	203	167	172	-209	413	303	334	338	419	321	273
HORSHR	-41	-40	-727	-500	81	-188	83	-274	-120	-244	-84	-183
TURB	40	-68	555	270	102	-125	145	-155	-102	-125	-115	-56
TOTFRT	-10	-10	-5	-5	-160	-334	-279	-334	-222	-280	-50	-200

M1 - FE3AM1, M2 - FE3AM2, VERSHR - VERTICAL SHEARING TERM, CONV - CONVERGENCE TERM, TILT - TILTING TERM, HORSHR - HORIZONTAL SHEARING TERM, TURB - TURBULENCE TERM, TOTFRT - TOTAL FRONTOGENESIS. ALL TERMS IN $\text{KM}^{-1}\text{S}^{-1} \times 10^9$. TOTFRT IN $\text{K}^2\text{M}^{-2}\text{S}^{-1} \times 10^{11}$ DOES NOT INCLUDE TURBULENCE FORCING FUNCTION.

TABLE 4

1500 UTC MAXIMA OF VORTICITY EQUATION TERMS AMONG ALL SIMULATIONS
(OVER PROFILER NETWORK)

<u>TERM</u>	<u>SIMULATION</u>				
	C	A1	A2	B	G
VAD	.01	.28	.40	2.2	53.5
HAD	.12	.08	.77	4.0	40.6
TILT	.02	.10	.20	1.2	12.1
CONV	.18	1.8	.90	3.9	59.
TEND	.31	1.9	2.5	6.5	34.9
VORT	14	21	33	52	116

M1 - FE3AM1, M2 - FE3AM2, VAD - VERTICAL ADVECTION TERM, HAD - HORIZONTAL ADVECTION TERM, TILT - TILTING TERM, CONV - CONVERGENCE TERM, TEND - LOCAL TENDENCY, VORT - ABSOLUTE VORTICITY. ALL TERMS IN $S^{-2} \times 10^8$. ABSOLUTE VORTICITY IN $S^{-1} \times 10^5$.

TABLE 5

TASS-SIMULATED VORTICITY EQUATION TERMS

TERM	TIME (UTC)											
	1410		1420		1430		1440		1450		1500	
	M1	M2	M1	M2	M1	M2	M1	M2	M1	M2	M1	M2
VAD	59	26	69	85	205	516	380	426	400	412	479	535
HAD	12	25	41	52	108	121	129	-154	-348	-233	-406	-338
TILT	-22	-30	33	-79	-47	63	-56	114	-116	-121	-117	103
CONV	19	25	51	37	193	52	353	149	593	295	128	295
VTEND	-252	-99	213	119	-1300	-632	-1876	736	2489	1320	-3485	3413
VORT	29	10	34	17	63	32	89	53	116	75	86	105

M1 - FE3AM1, M2 - FE3AM2, VAD - VERTICAL ADVECTION TERM, HAD HORIZONTAL ADVECTION TERM, TILT - TILTING TERM, CONV - CONVERGENCE TERM, TEND - LOCAL TENDENCY, VORT - ABSOLUTE VORTICITY . ALL TERMS IN $S^{-2} \times 10^9$. ABSOLUTE VORTICITY IN $S^{-1} \times 10^5$.

TABLE 6

'SPINUP' FACTORS AMONG SIMULATIONS

SIMULATION	G	B	A2	A1
VORTICITY INCREASE	100	50	25	15
TIME REDUCTION	1/6	1/2	1	1
SPINUP FACTOR	600	100	25	15

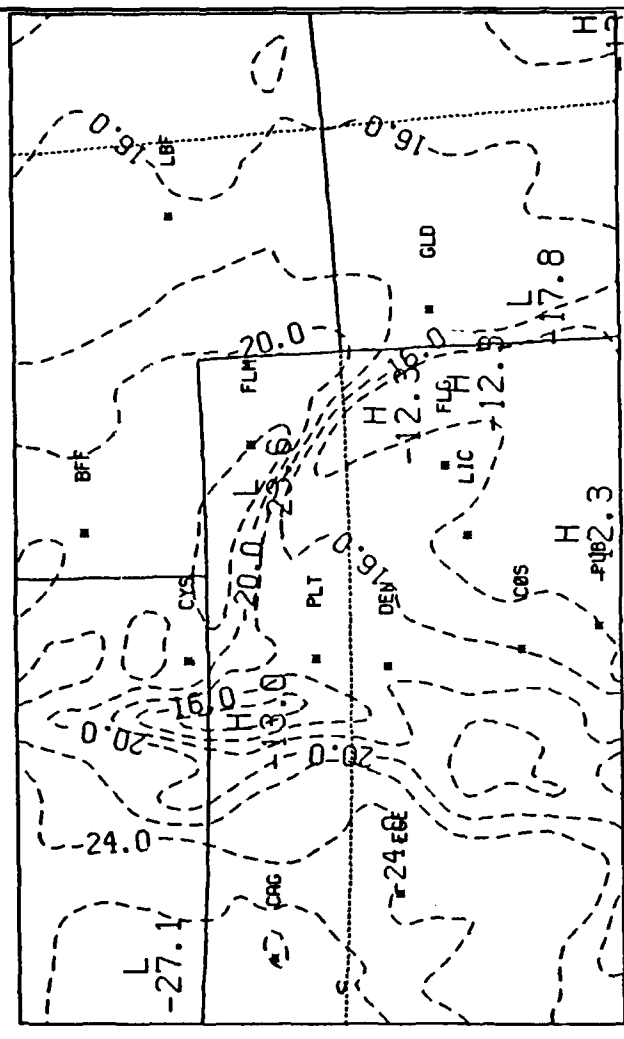
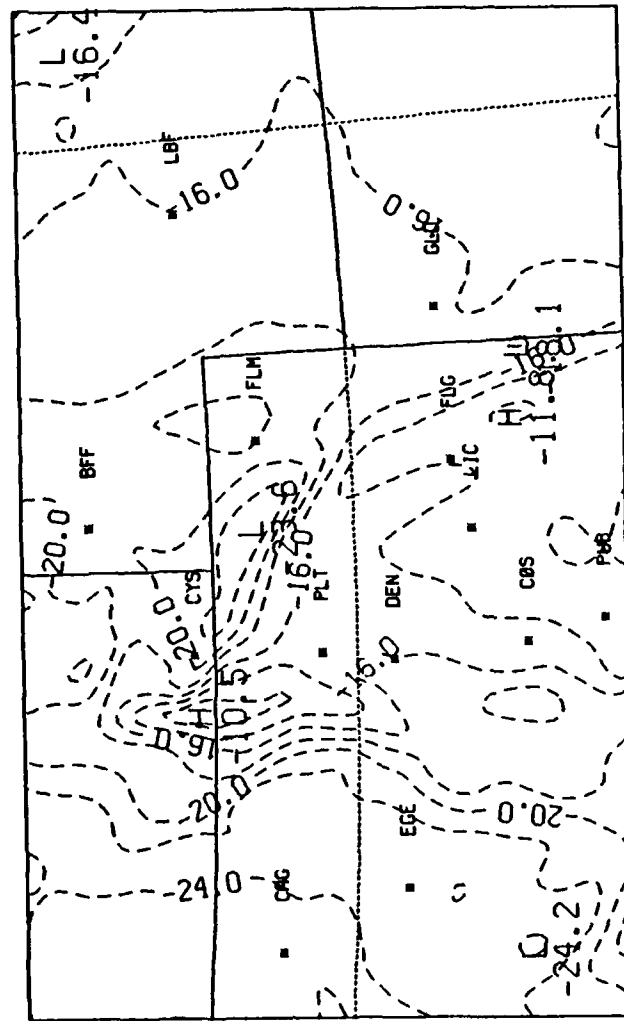
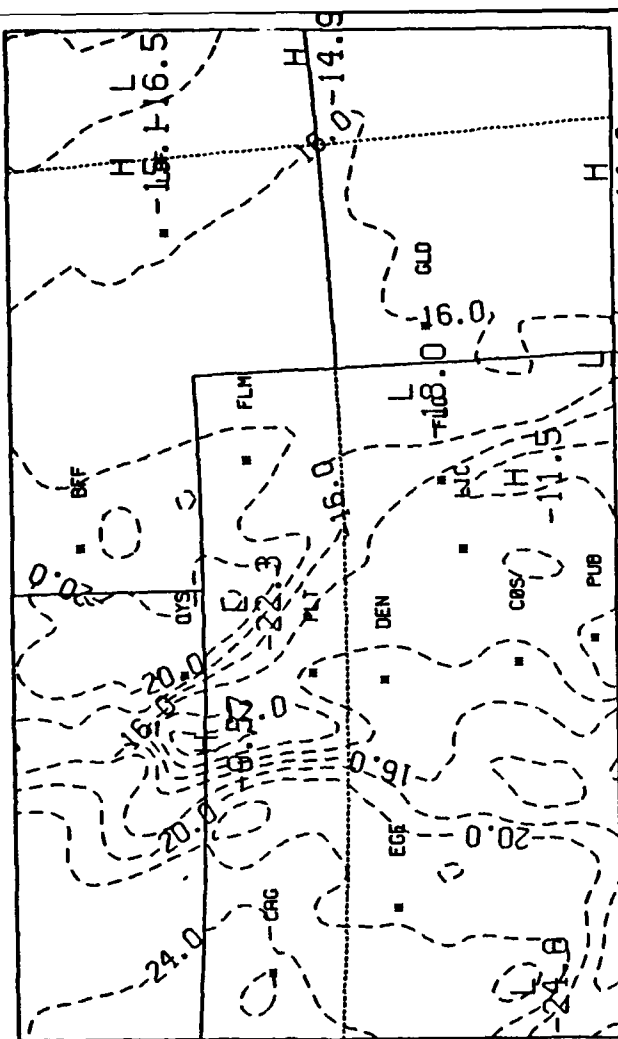
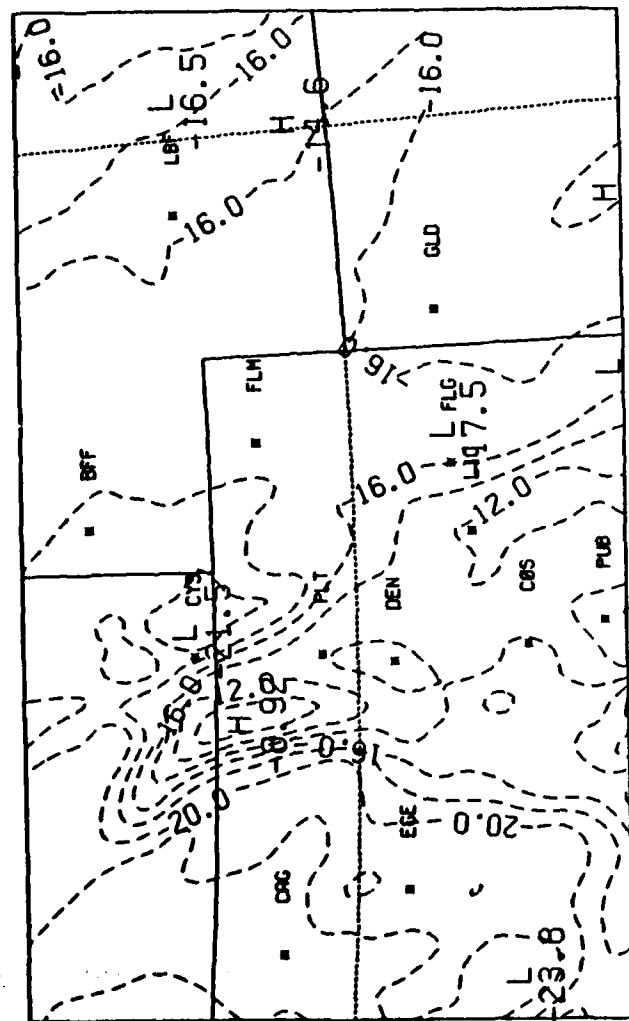
ALL SIMULATIONS COMPARED TO SIMULATION C

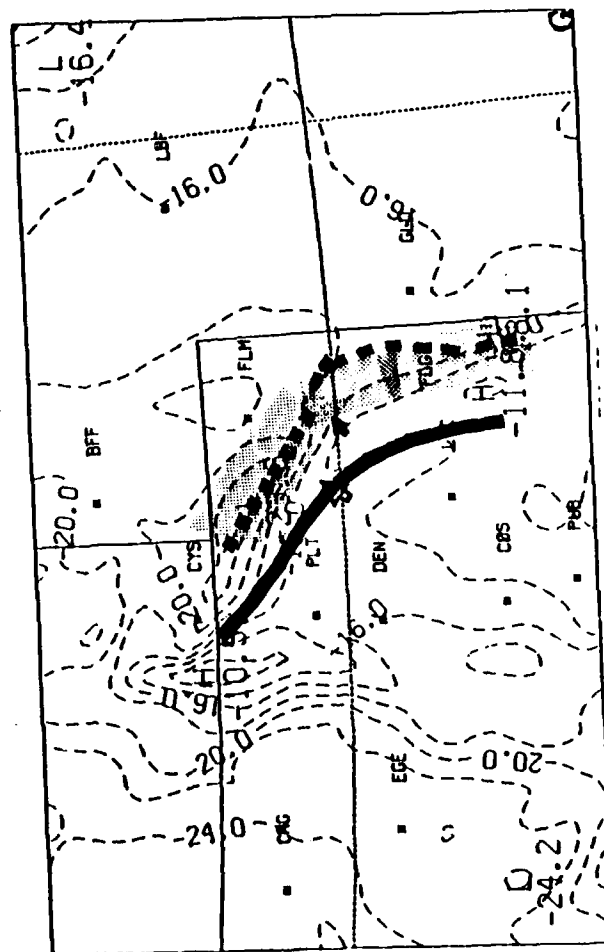
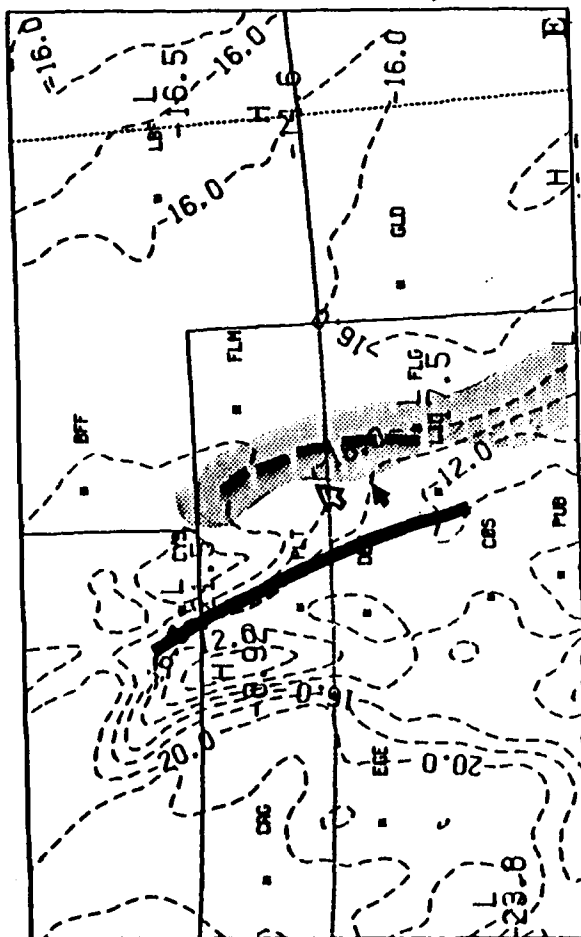
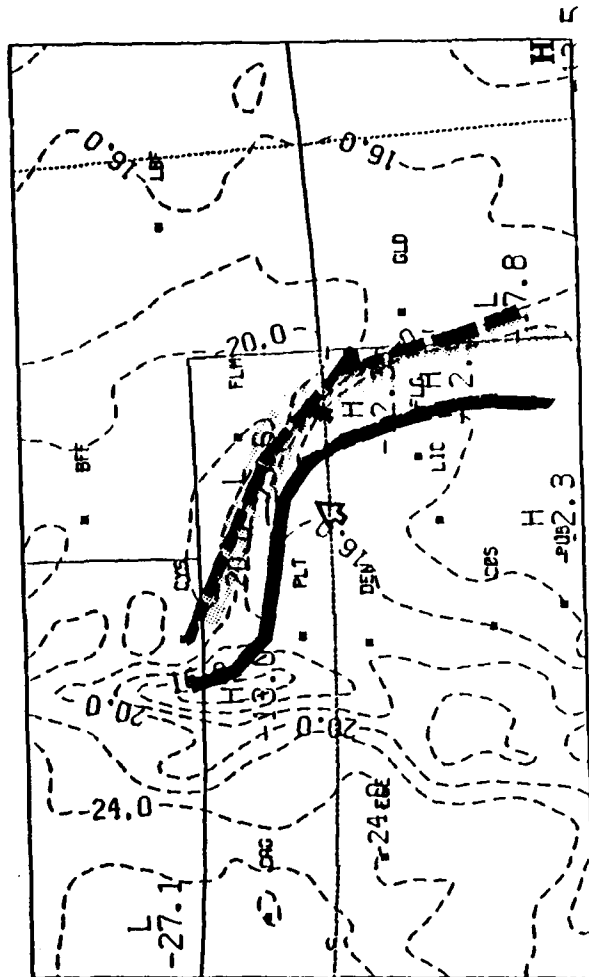
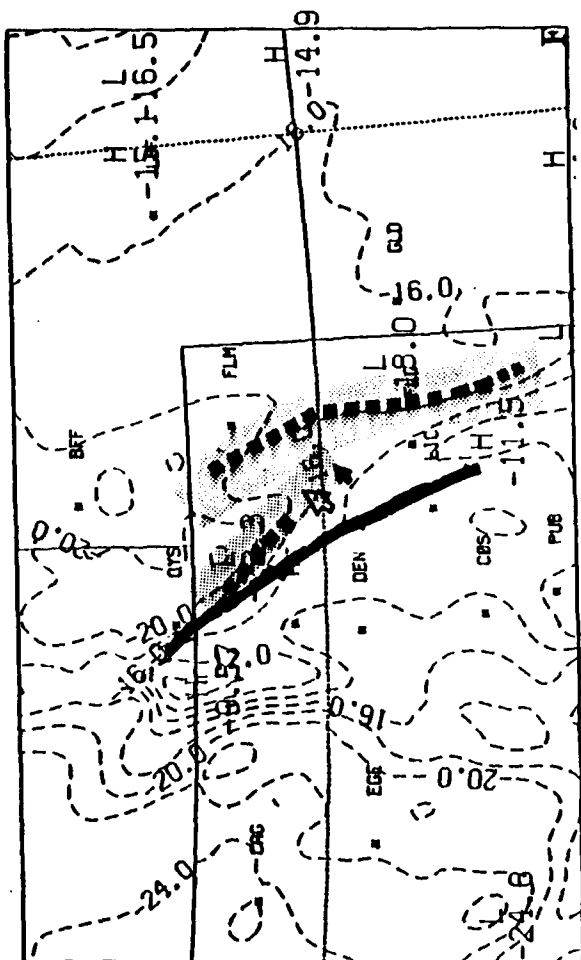
TABLE 7

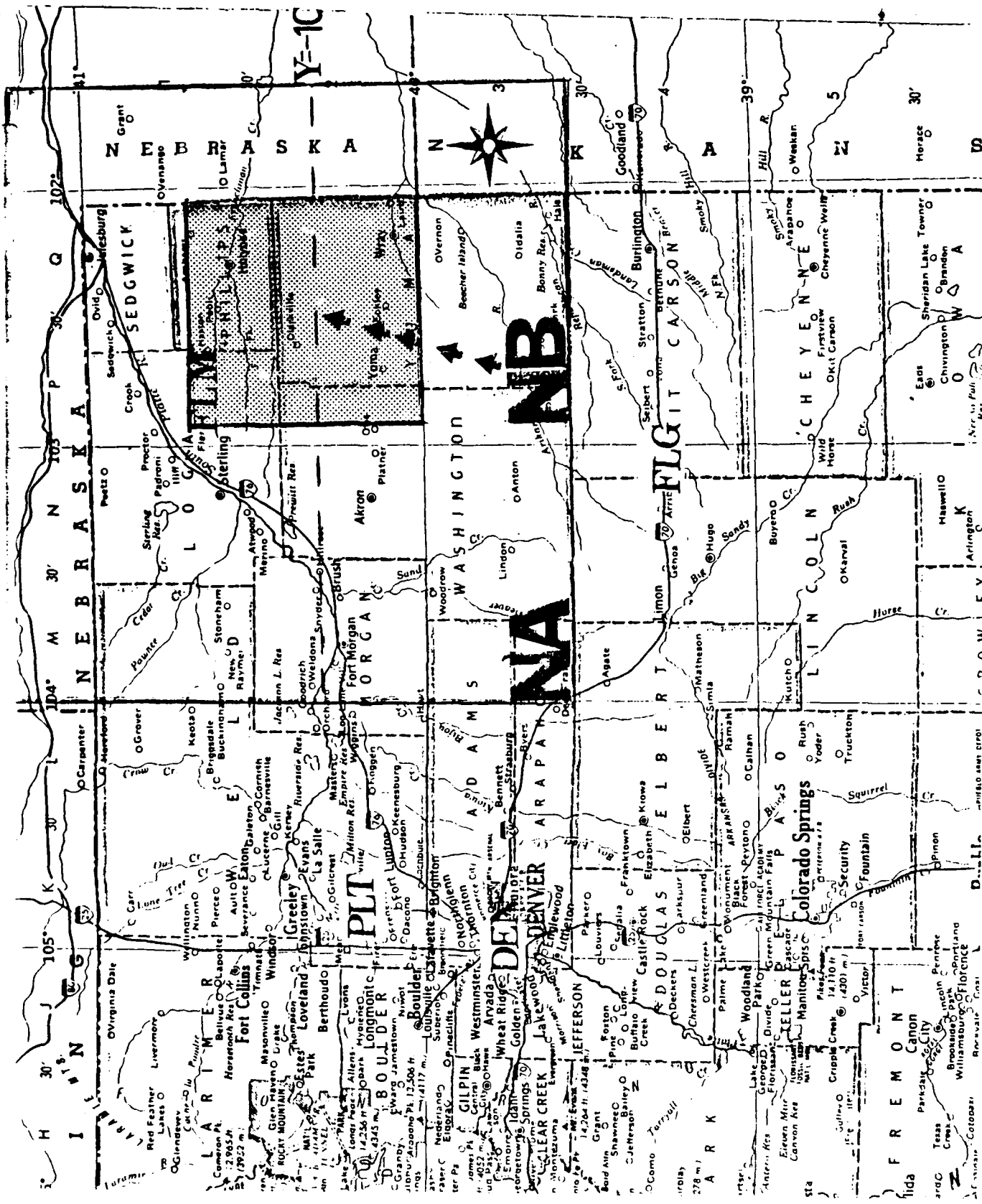
HIGHEST PRESSURE (MB) OF THE POTENTIAL VORTICITY VALUES EXCEEDING
 $1.0 \times 10^{-5} \text{ Kmb}^{-1}\text{s}^{-1}$ AS A FUNCTION OF SIMULATION AND WEST-EAST
LOCATION AT 1500 UTC

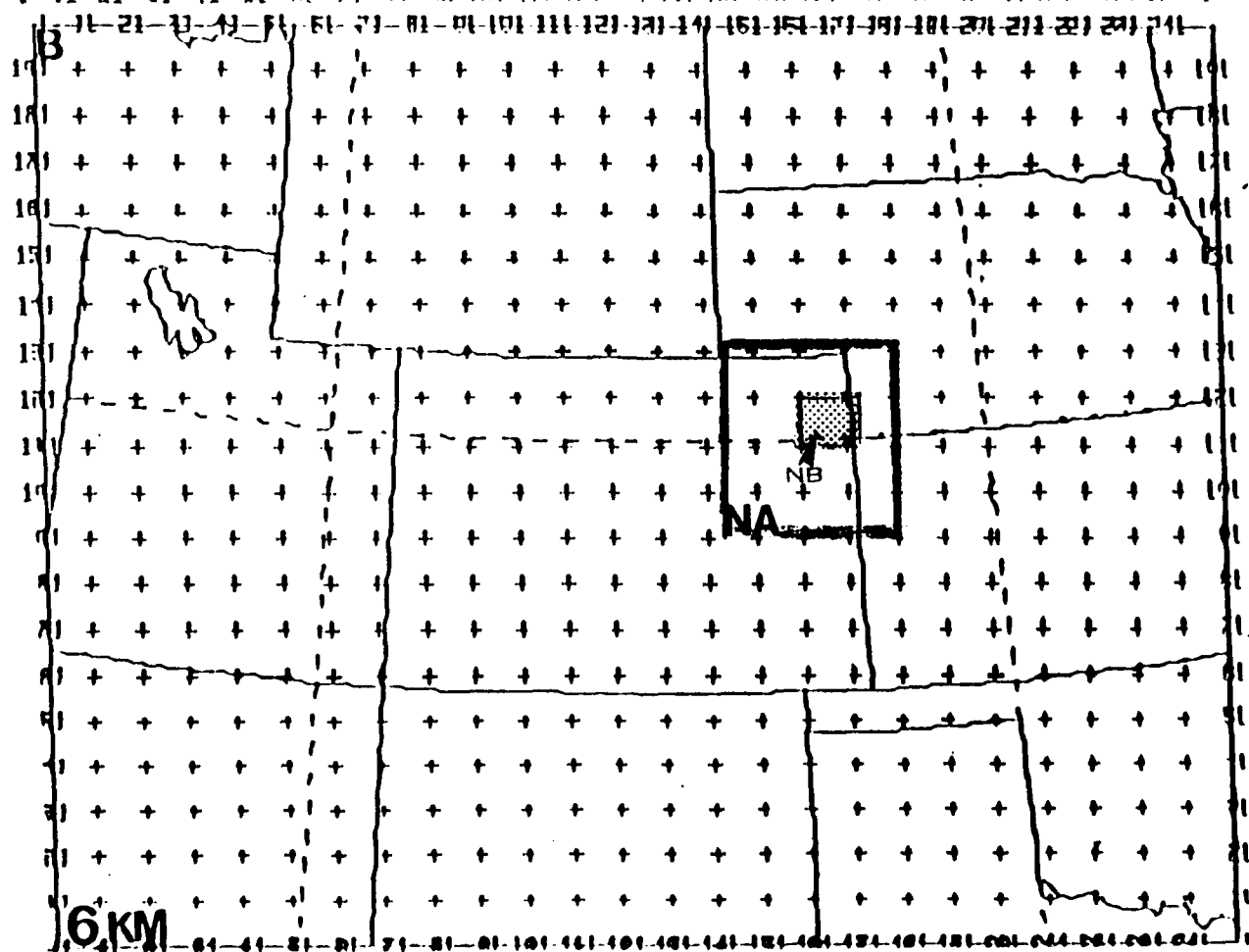
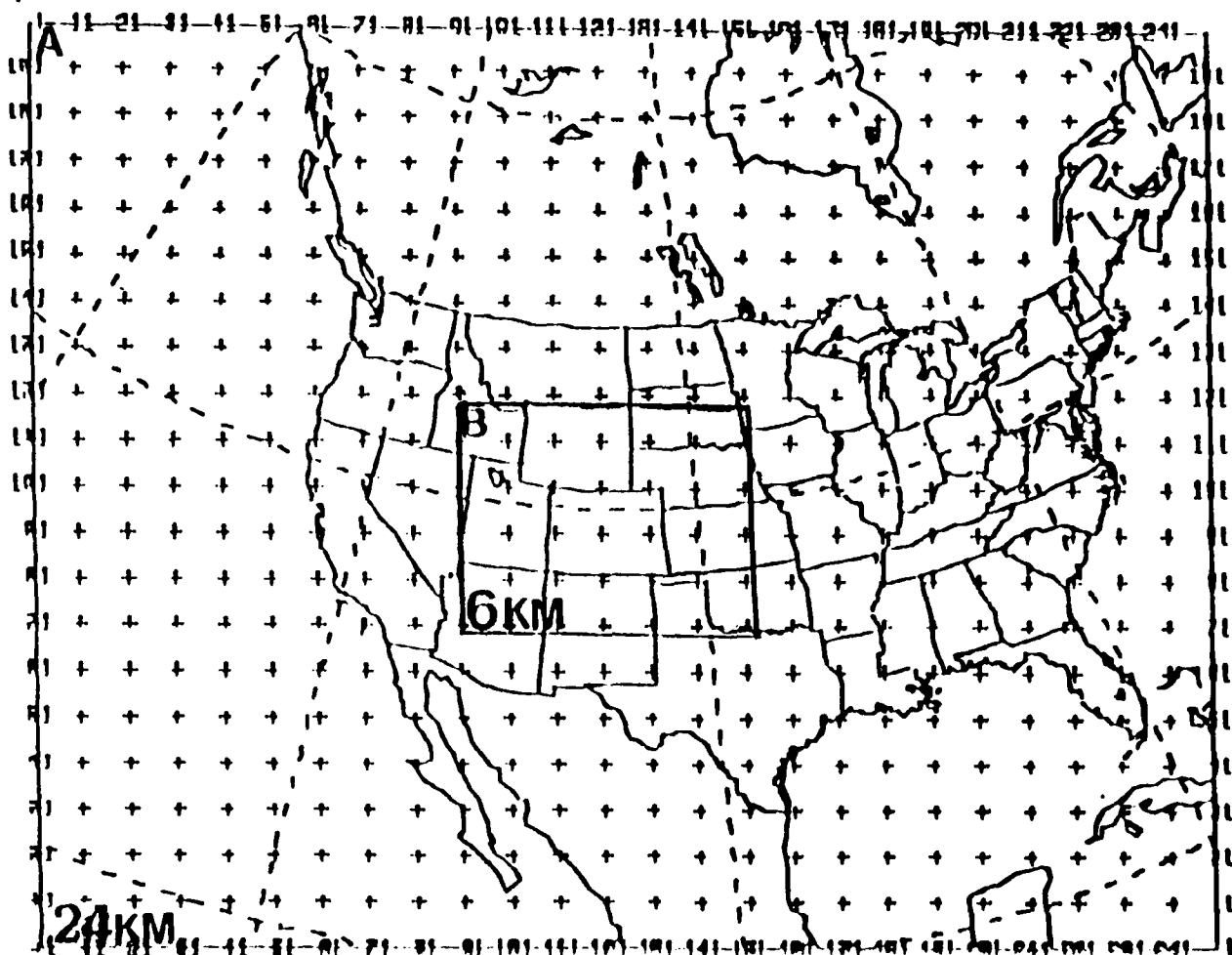
<u>SIMULATION</u>	<u>LOCATION</u>		
	UTAH/COLORADO BORDER	BASE OF COLORADO FRONT RANGE	FLM
C	520	500	350
A1	530	590	370
A2	540	600	500
B	610	630	640
G	XXXXXXXXXX	XXXXXXXXXX	760

XXXXXXXXXX INDICATES LOCATION OUTSIDE OF SIMULATION DOMAIN

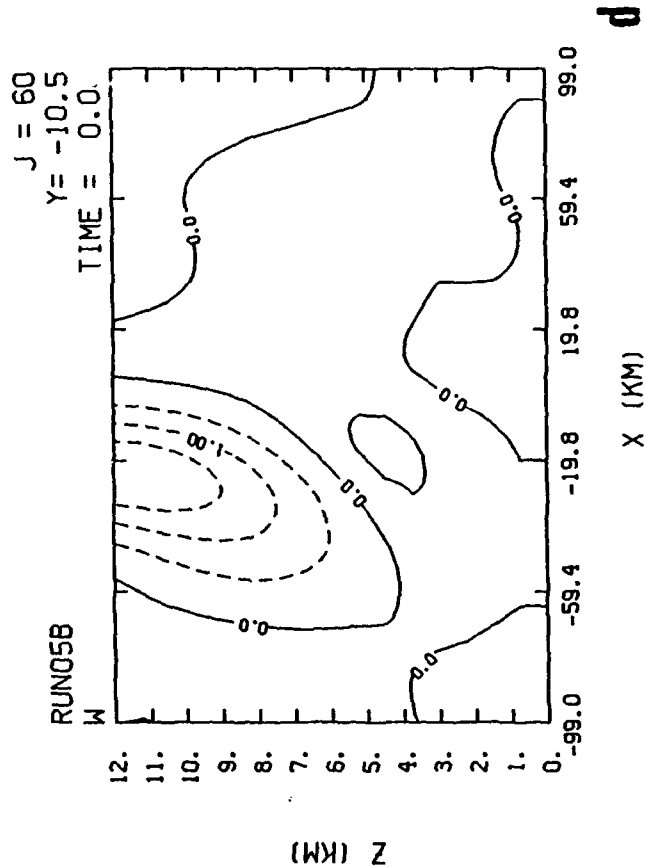
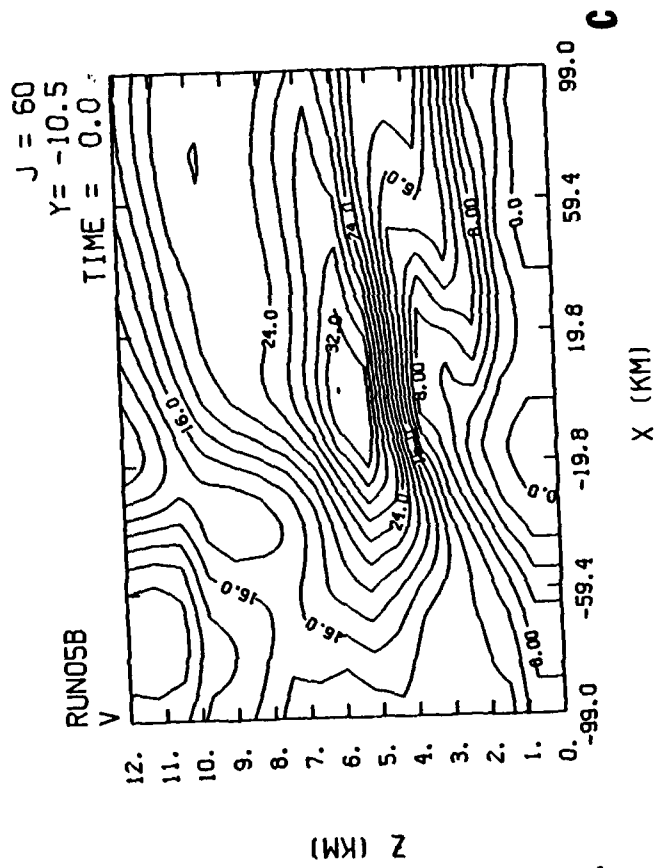
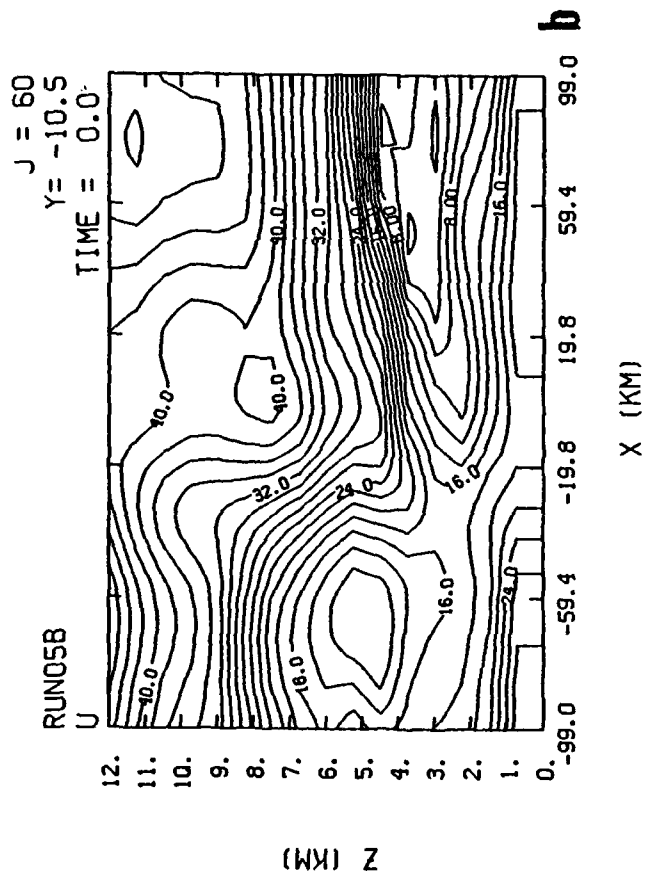
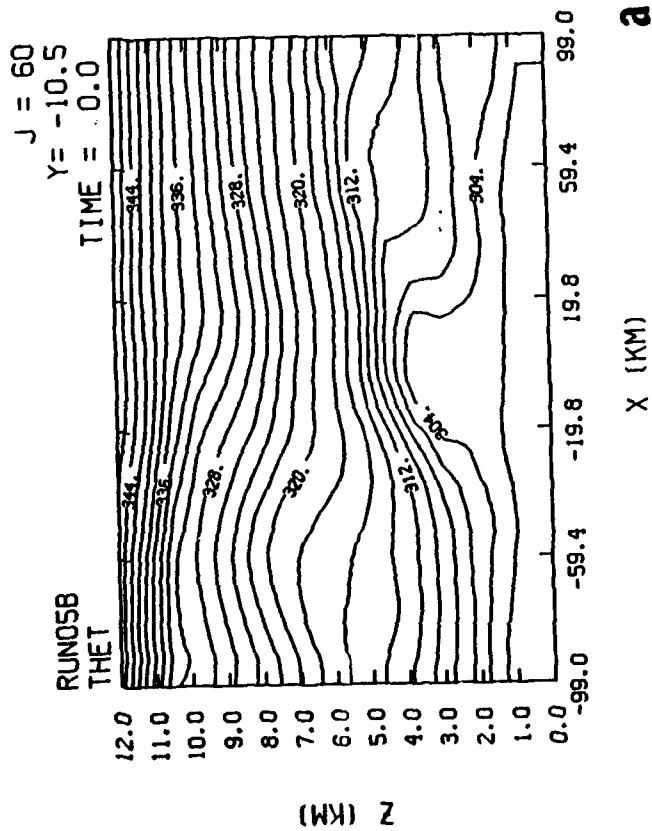


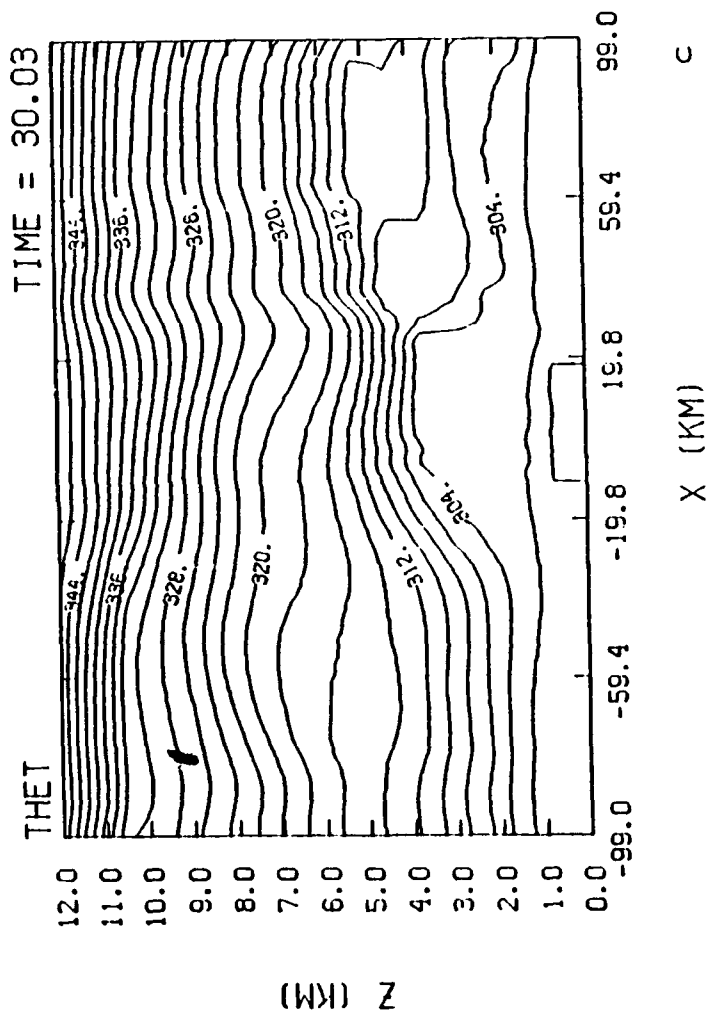
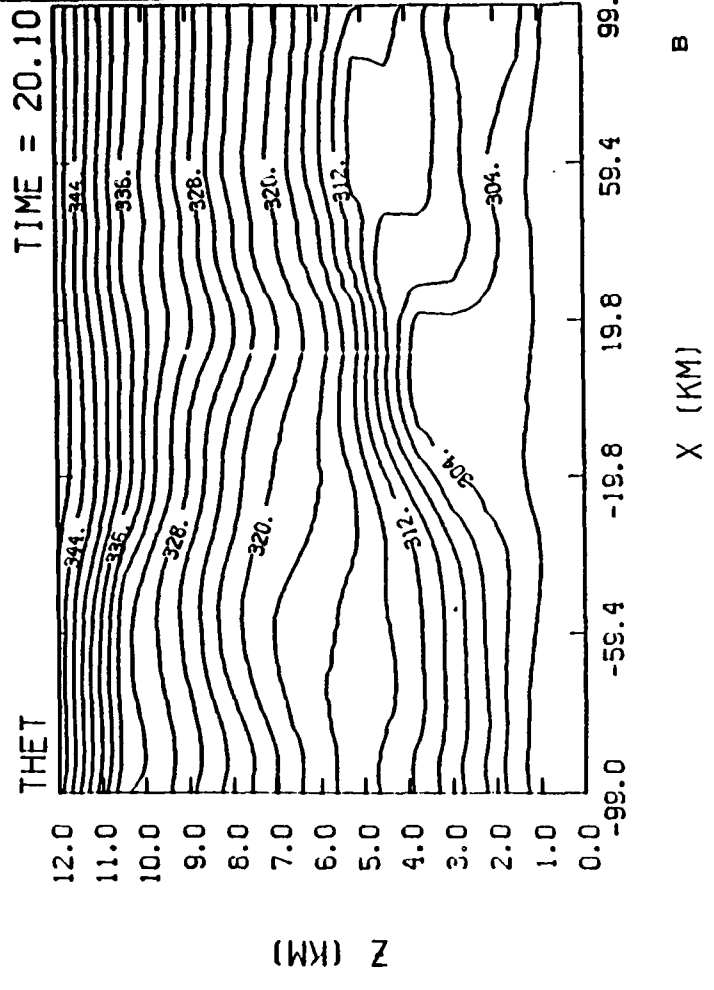
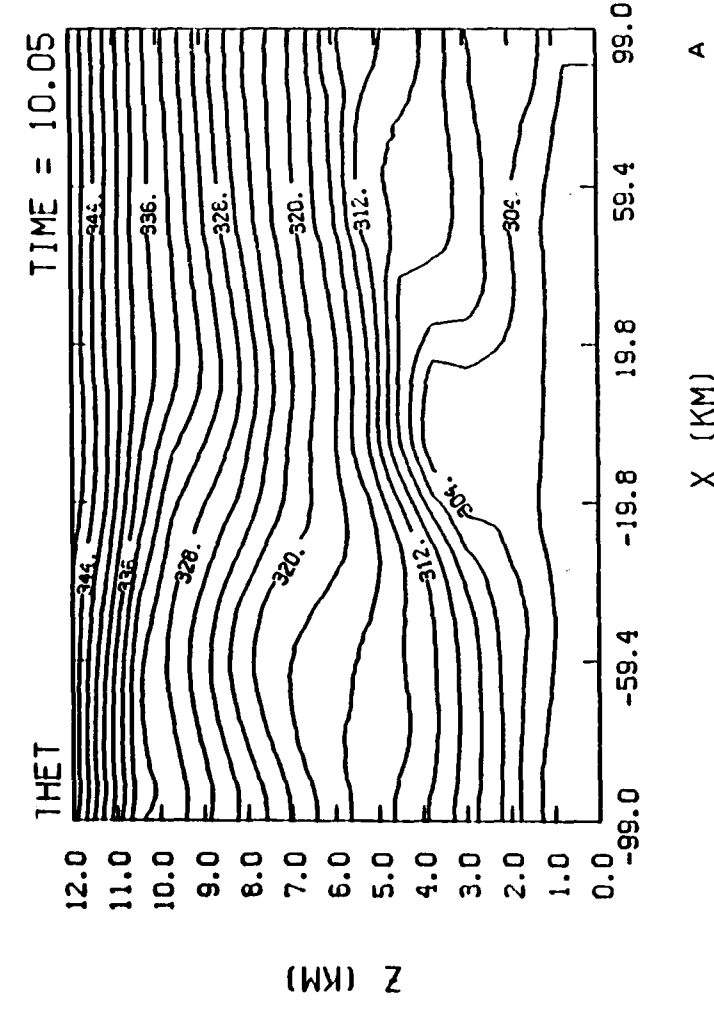


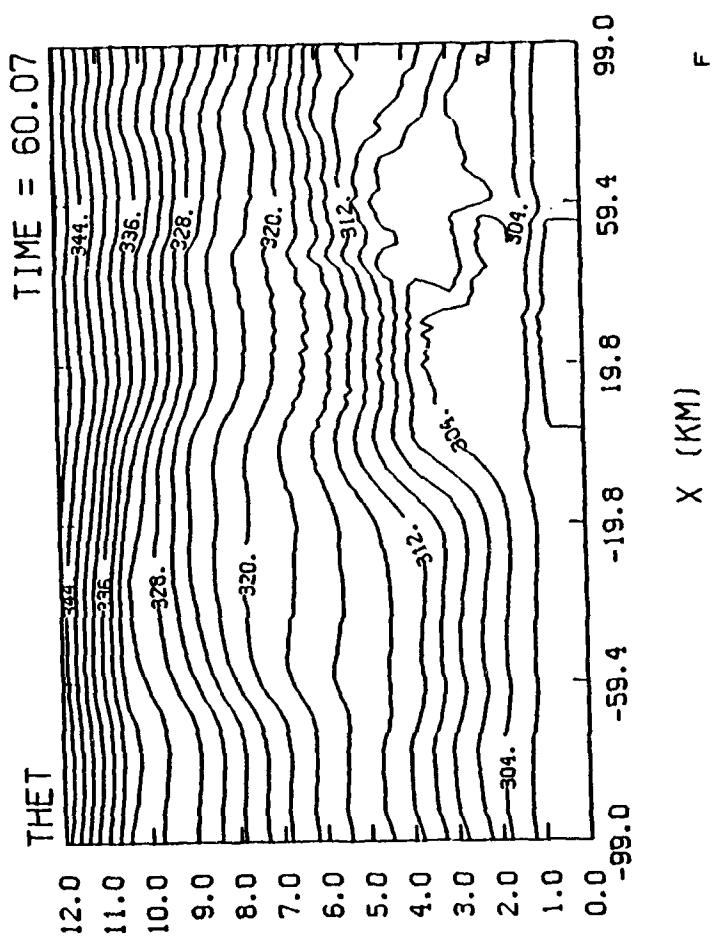
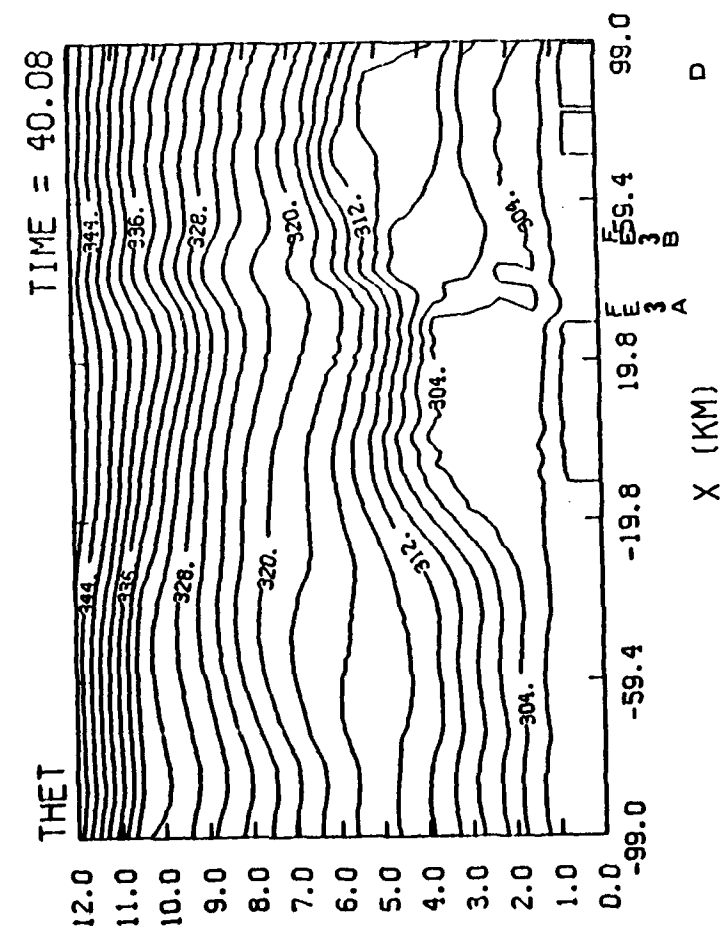
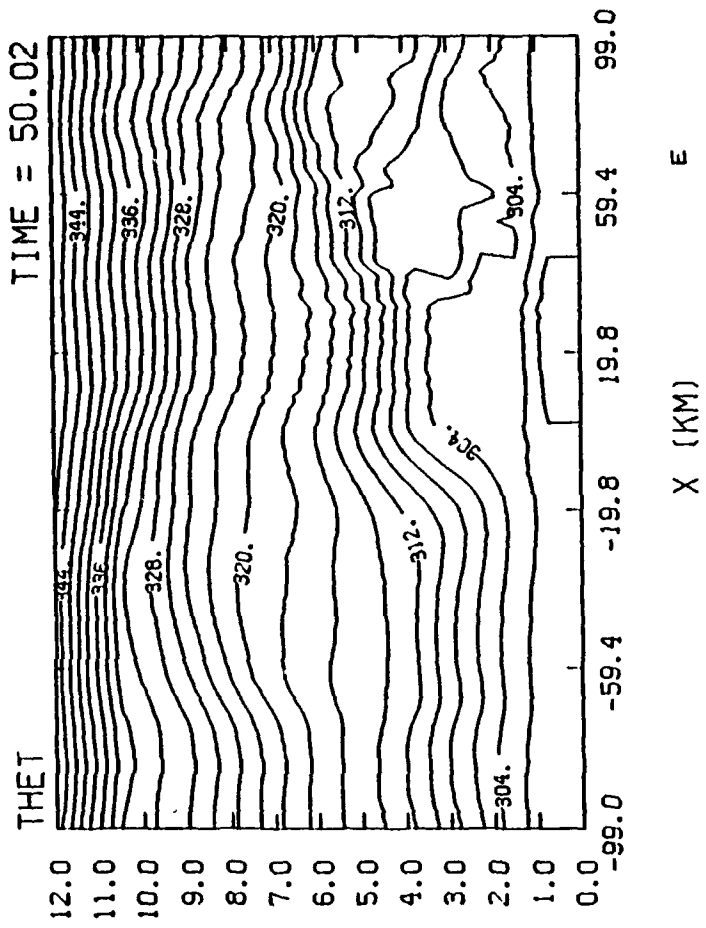


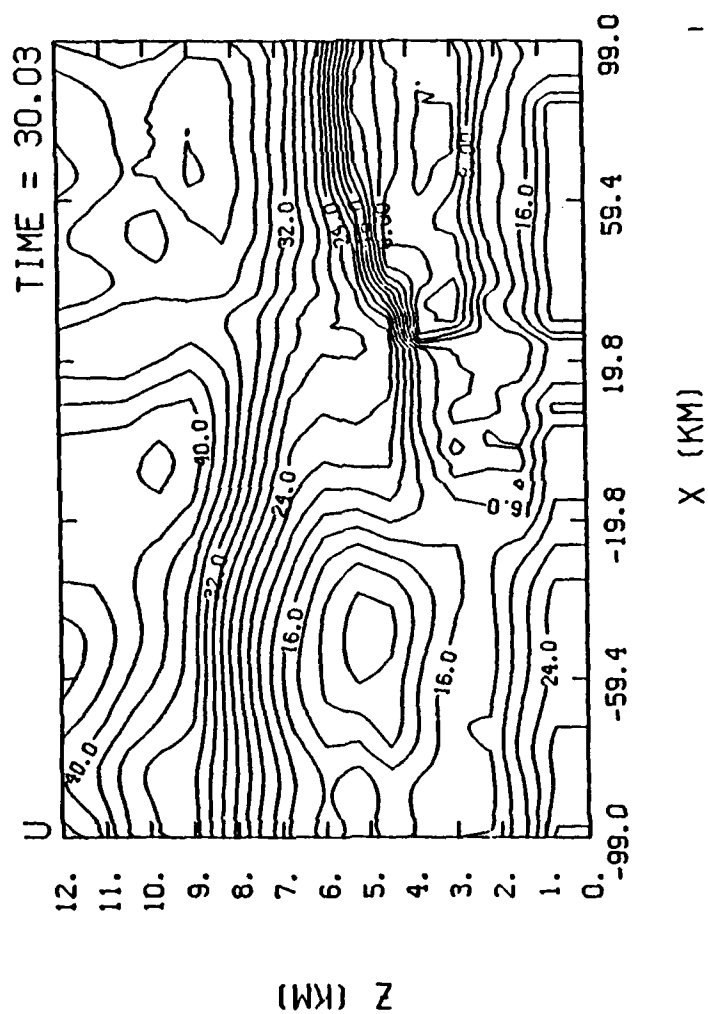
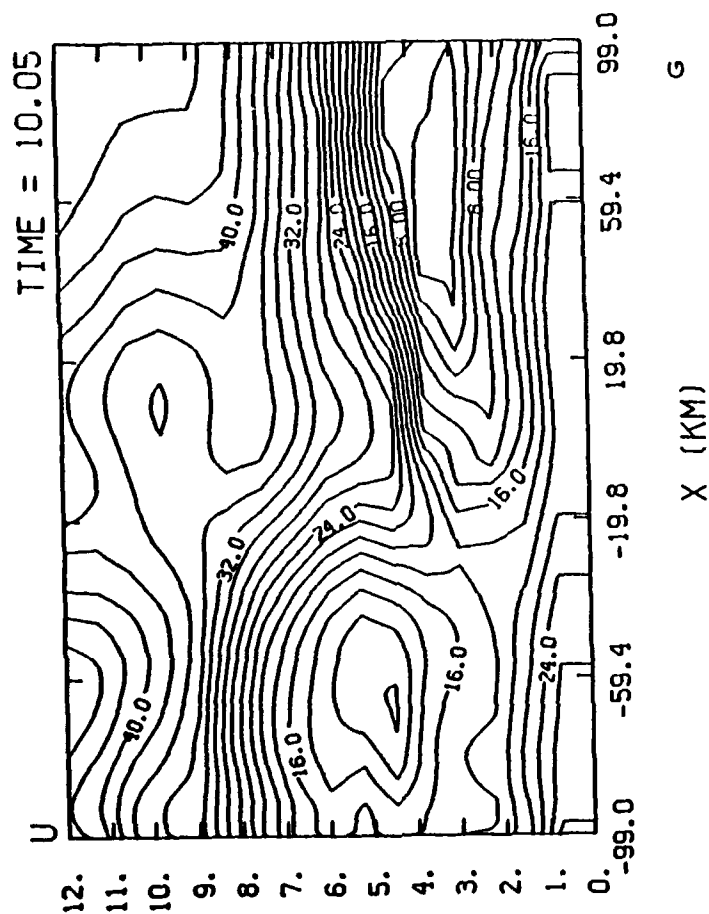
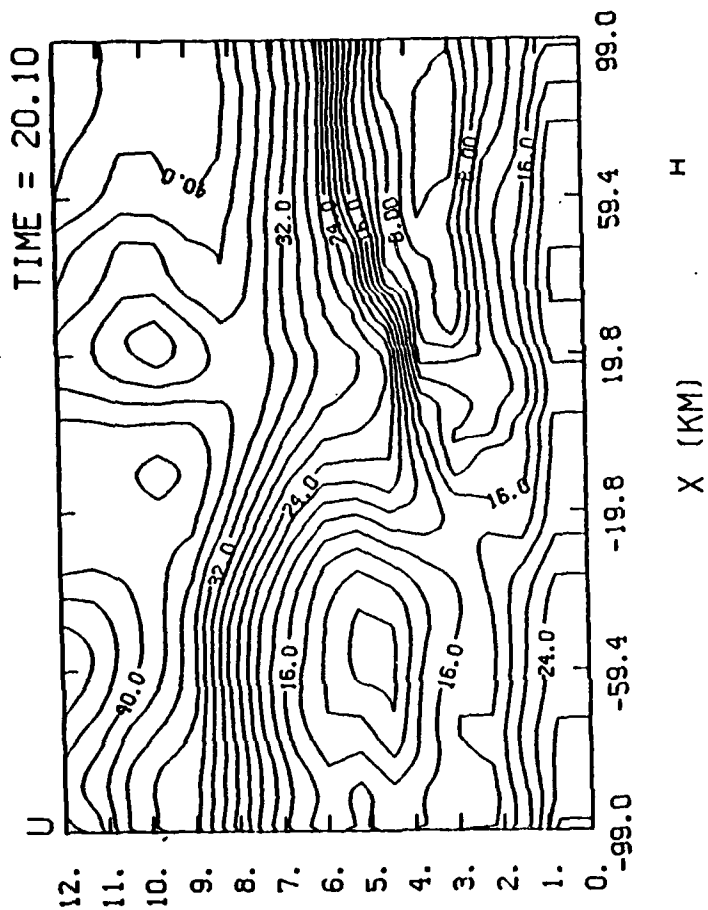


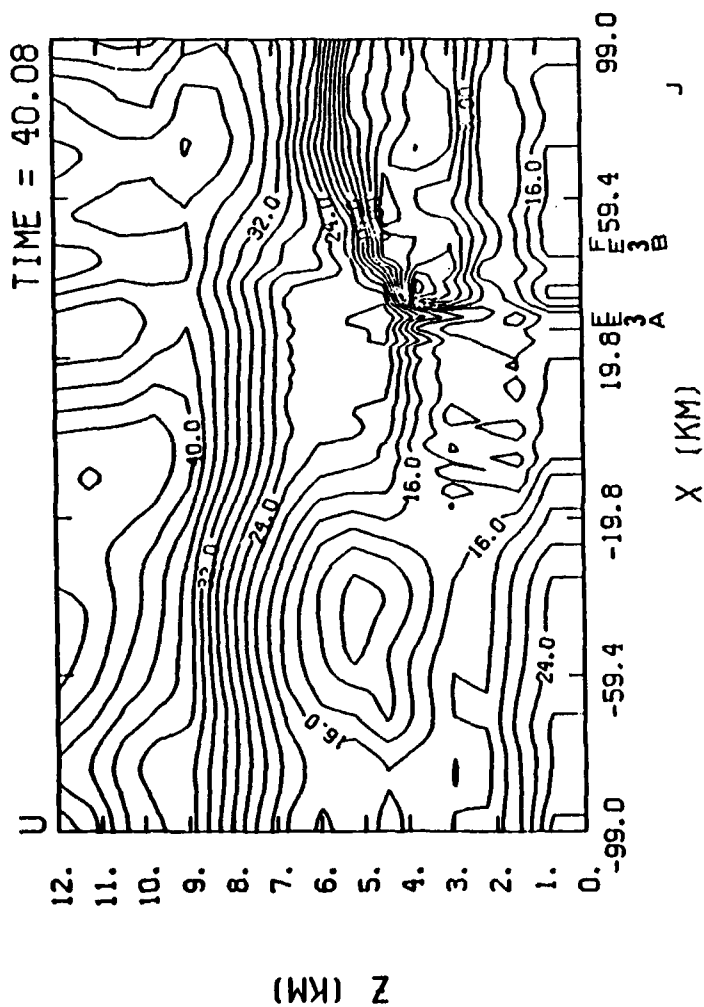
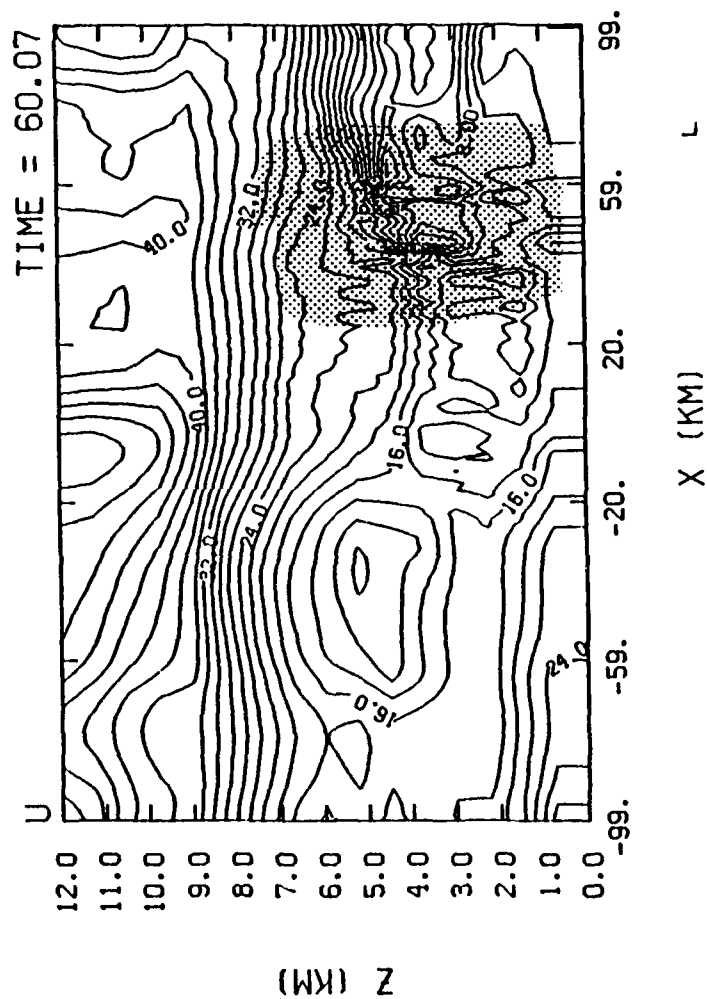
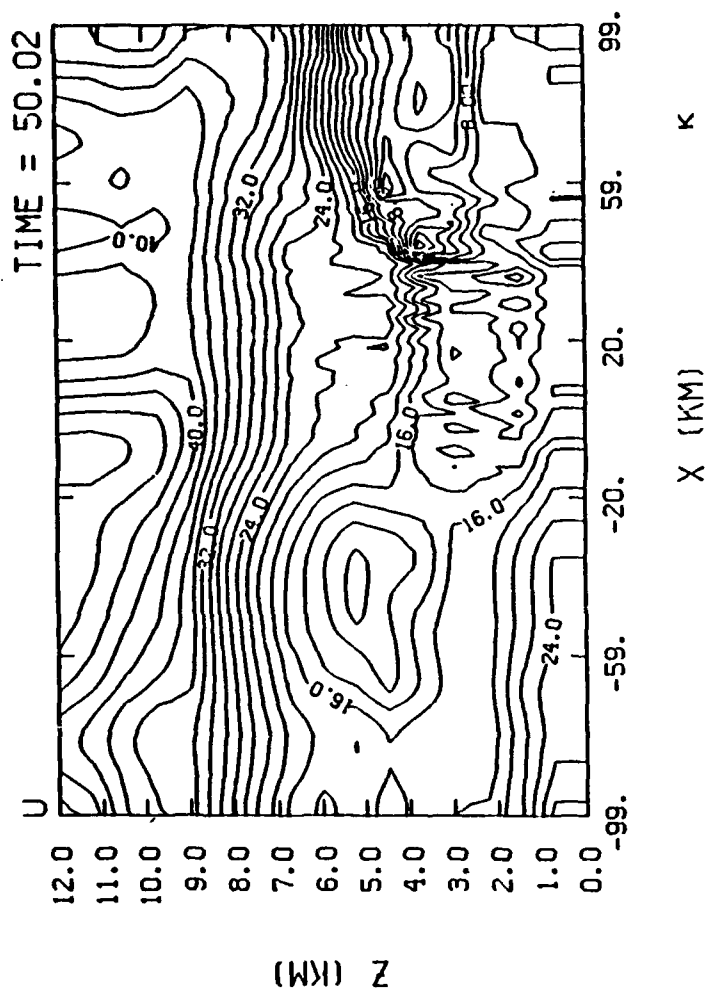
b

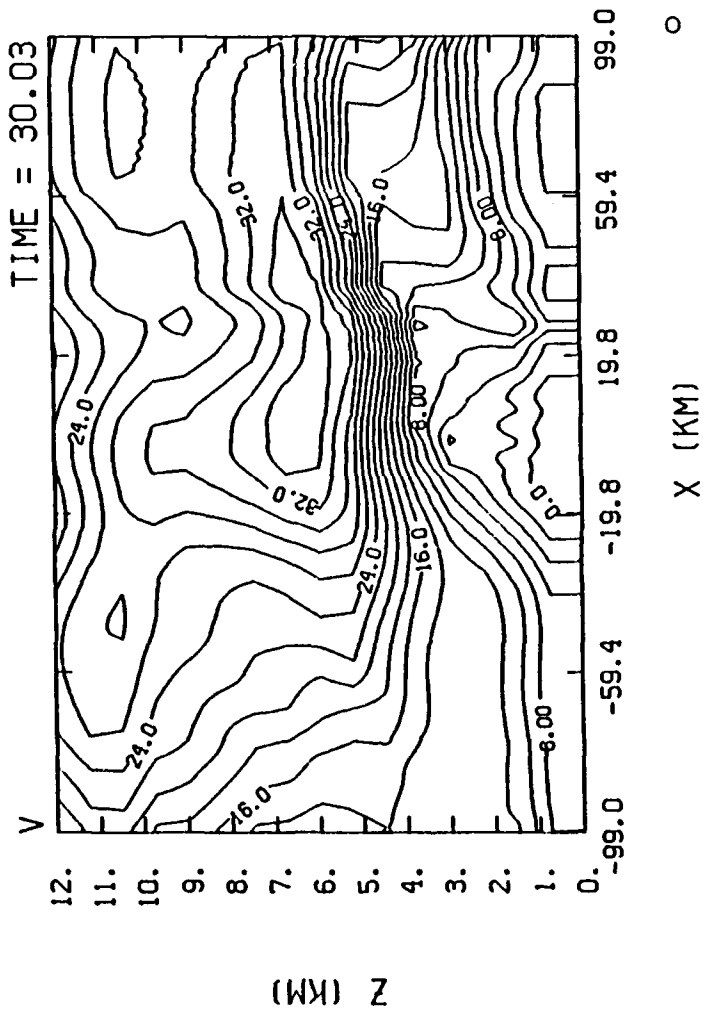
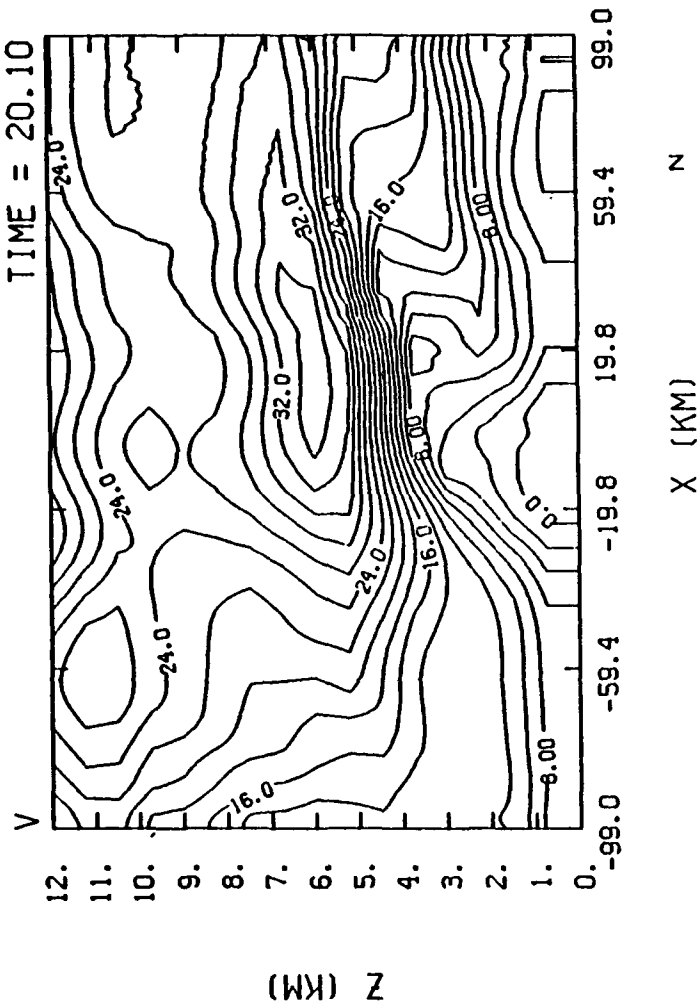
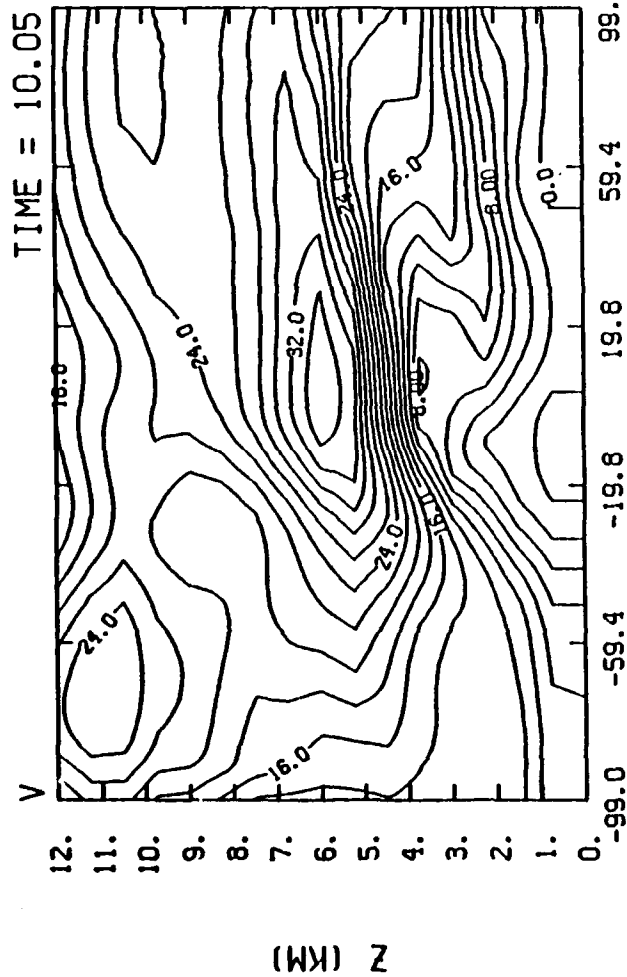


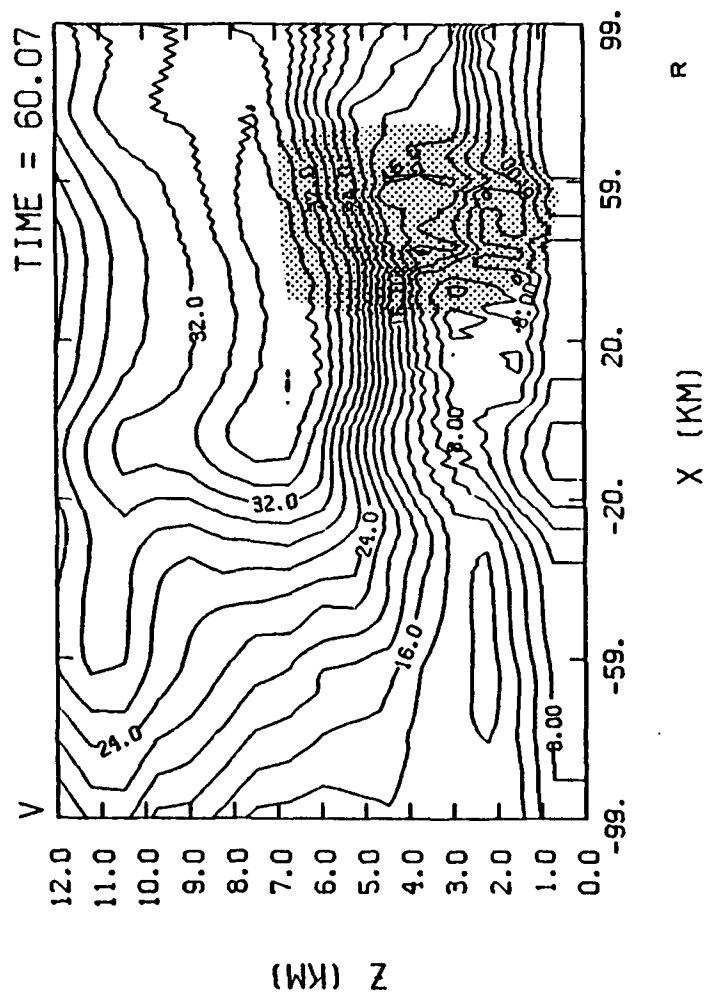
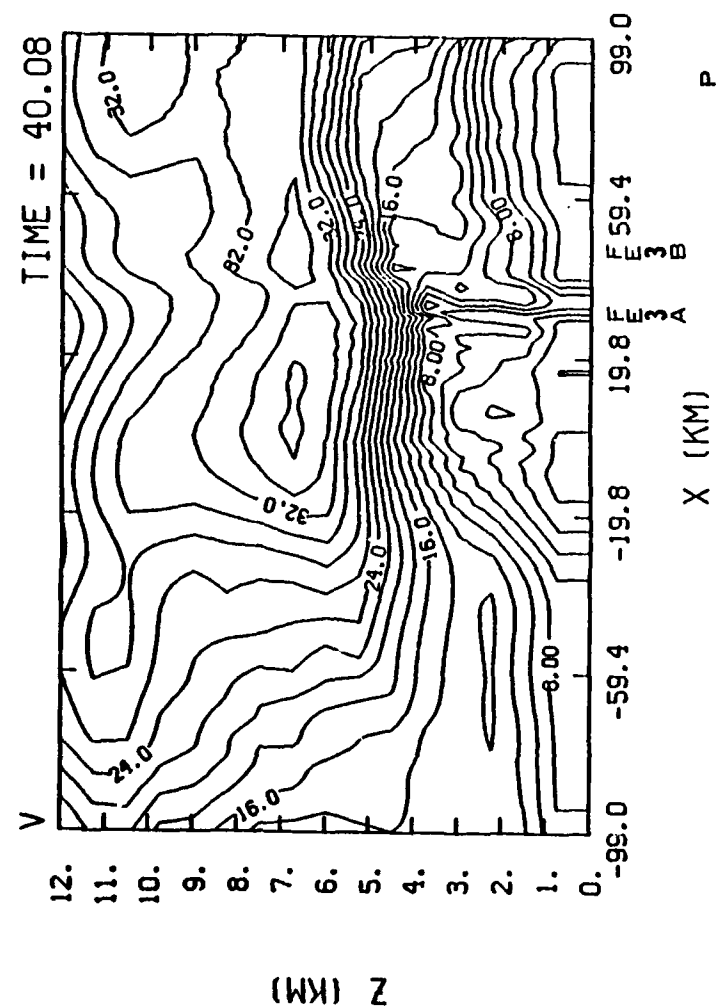
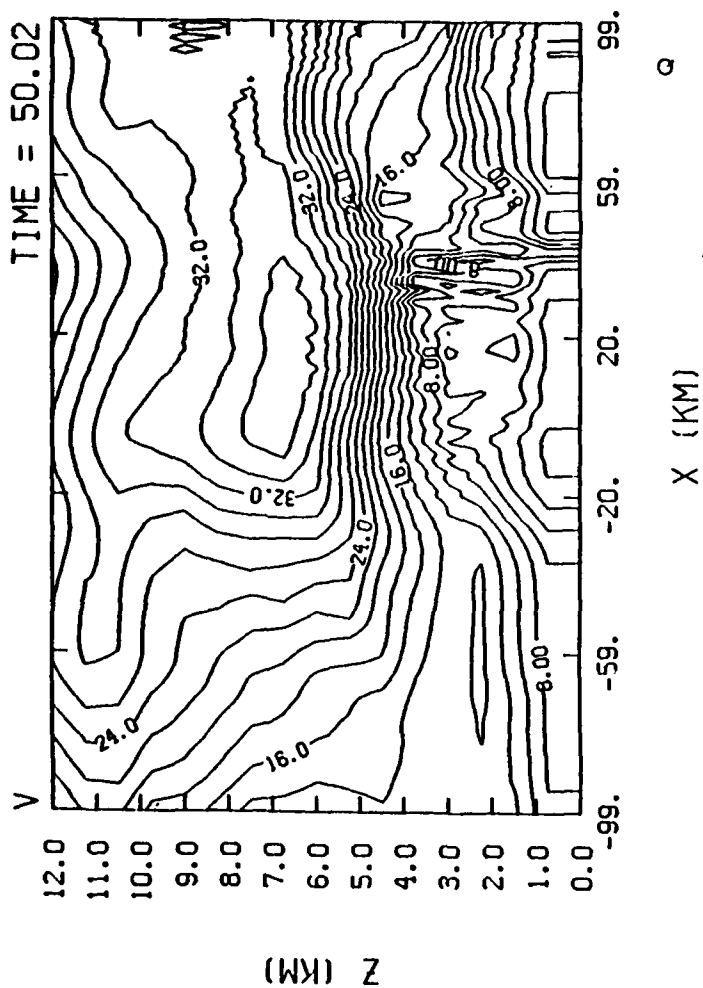




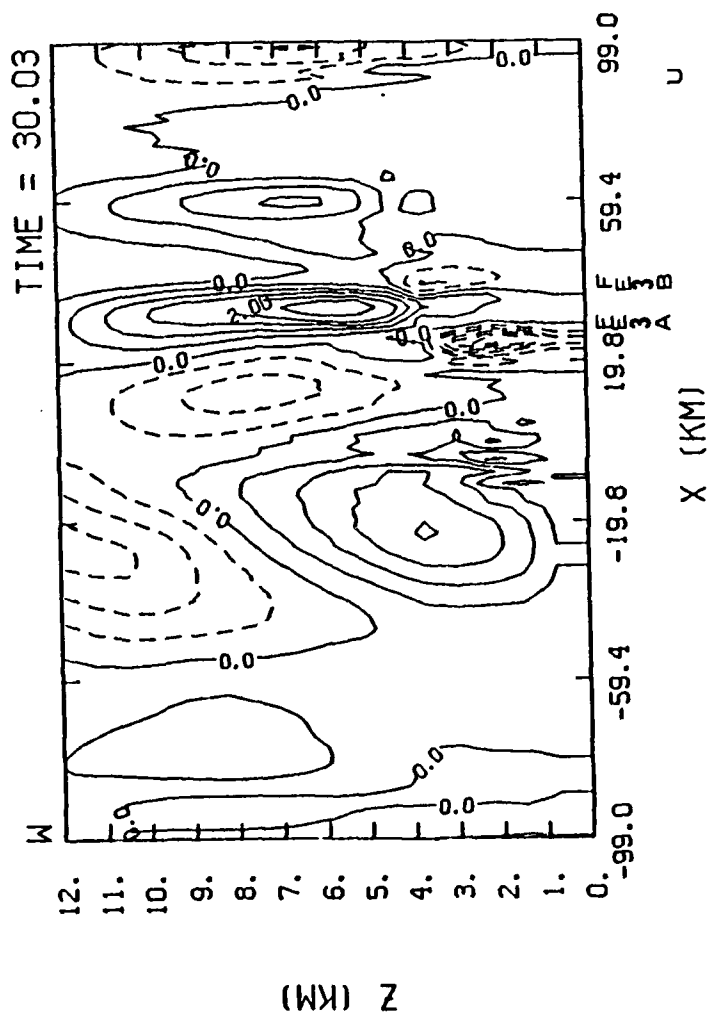
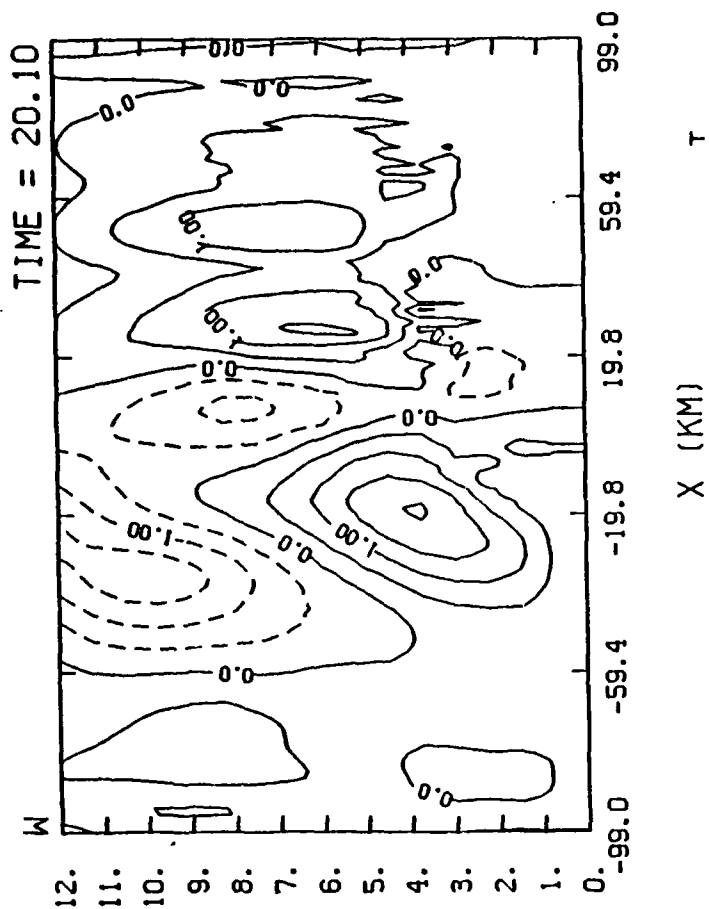
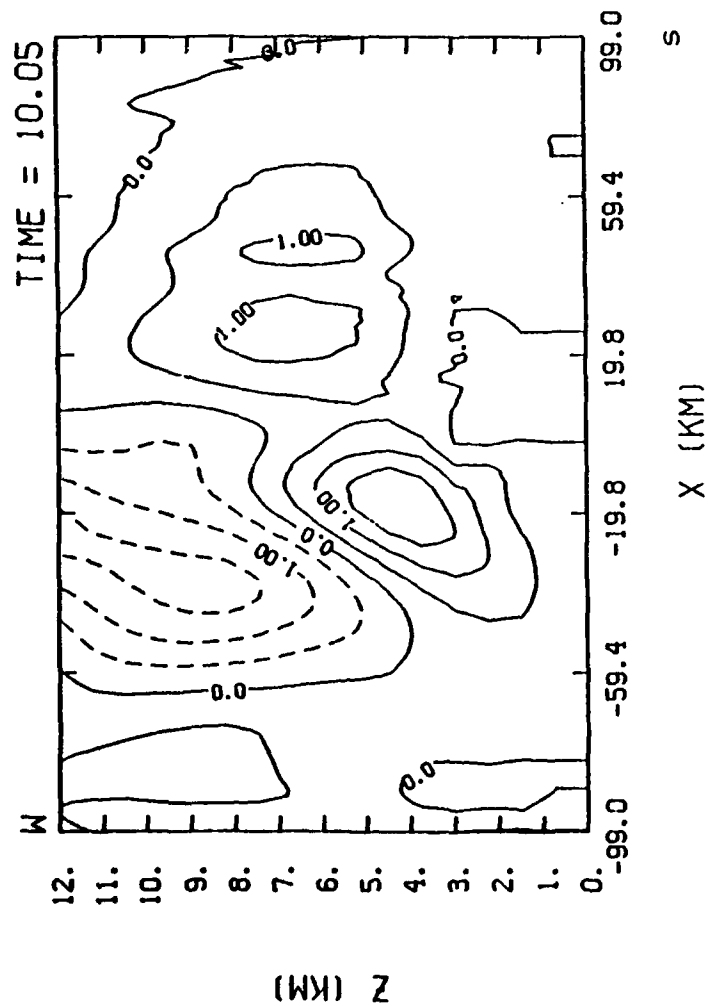


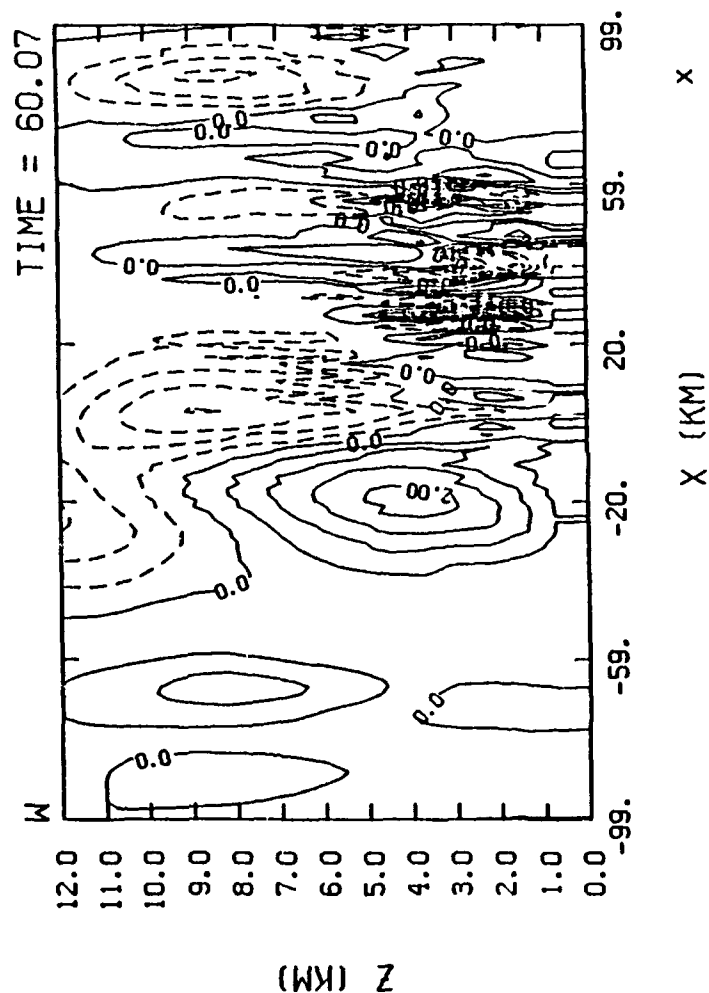
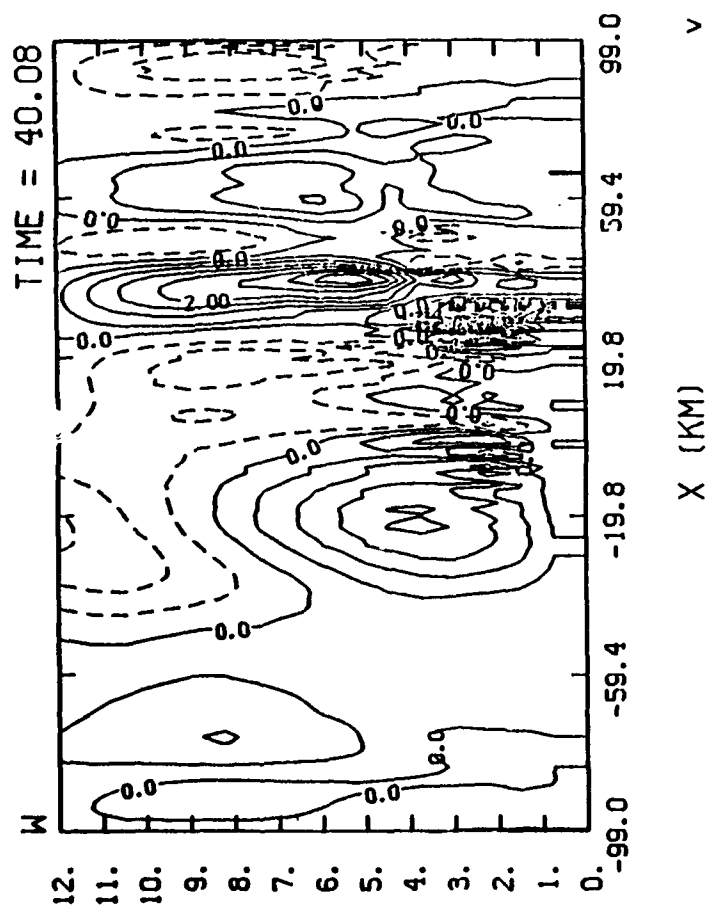
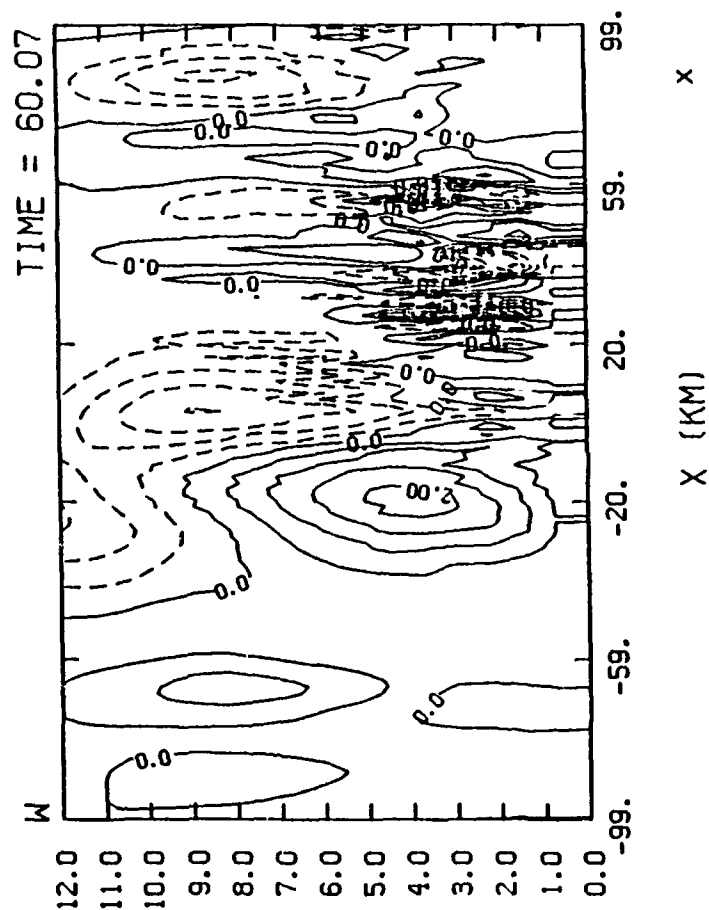
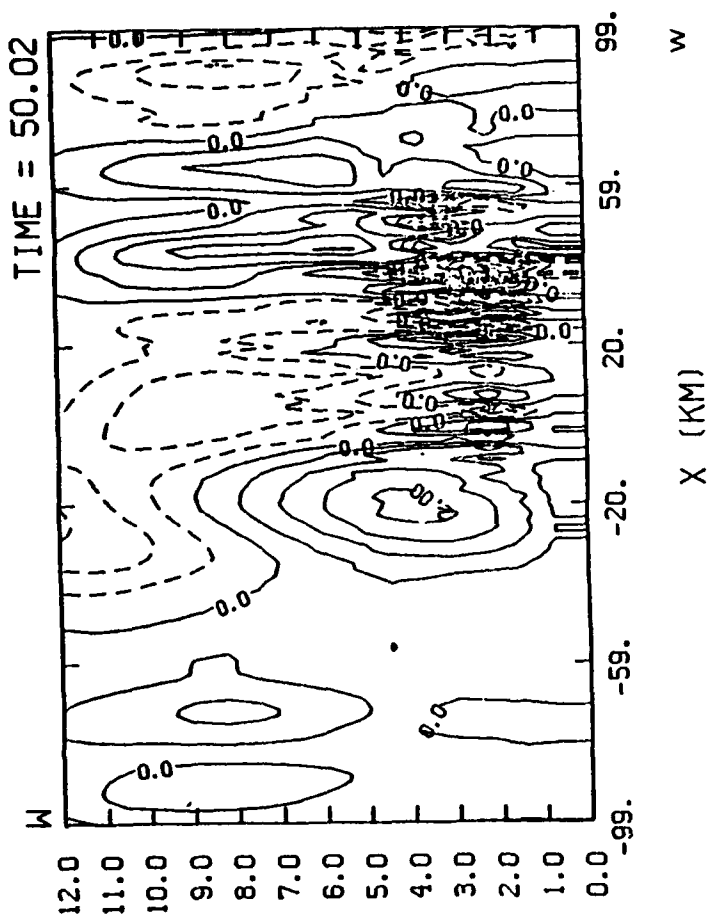


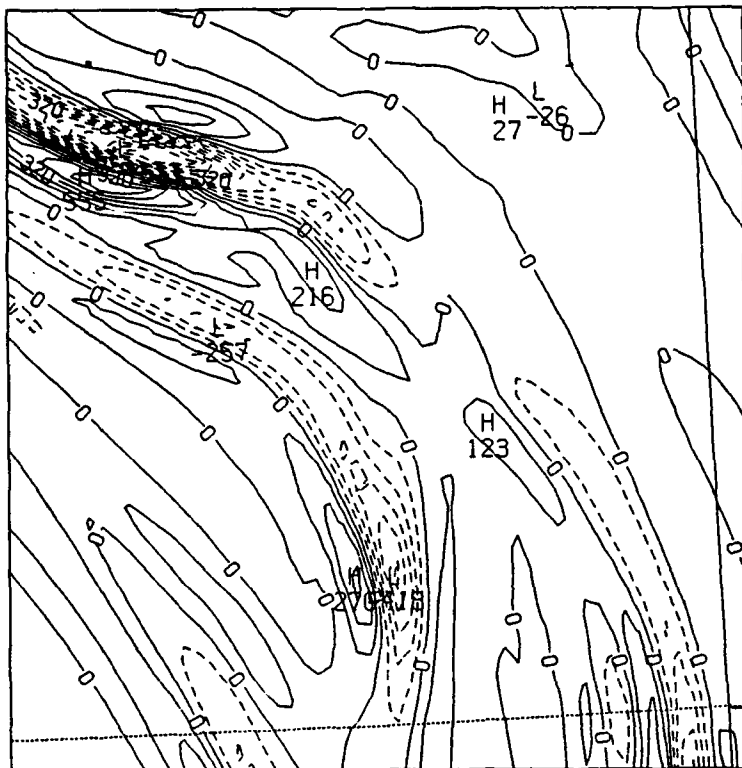




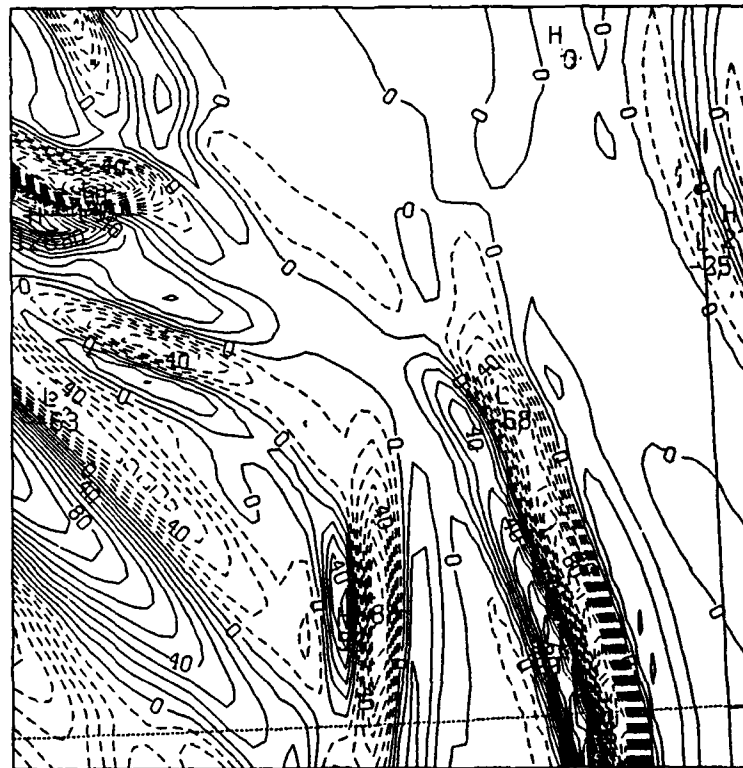
R



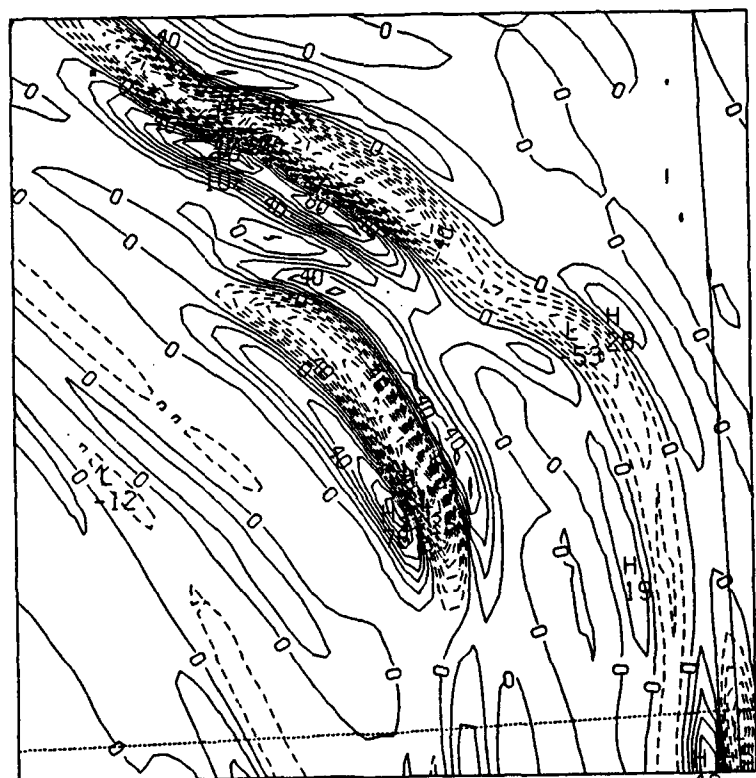




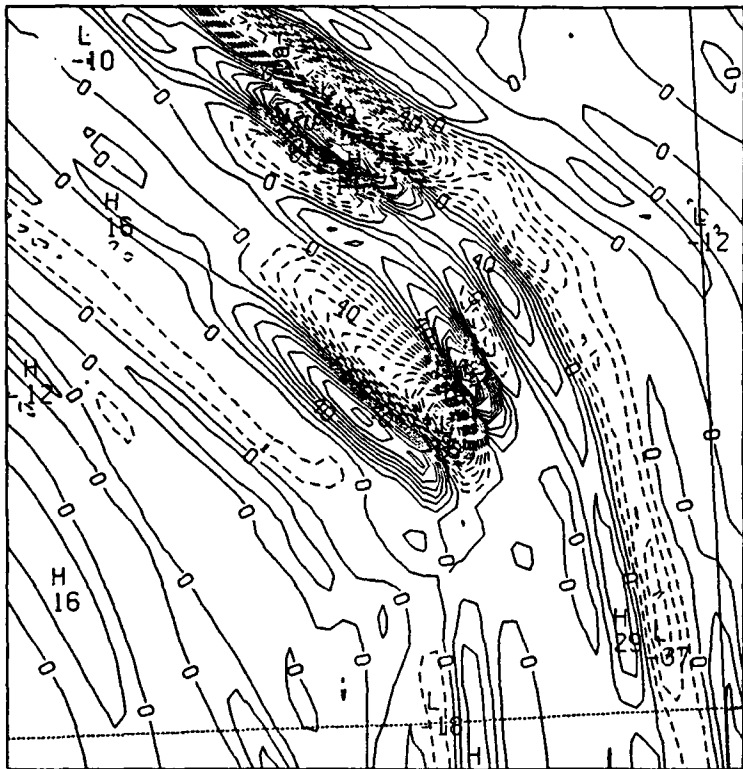
a



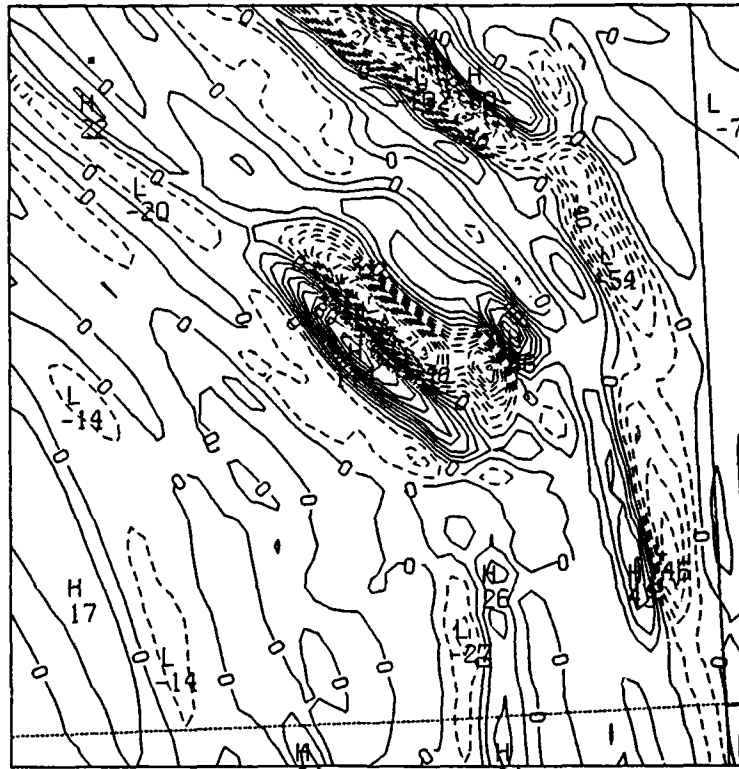
b



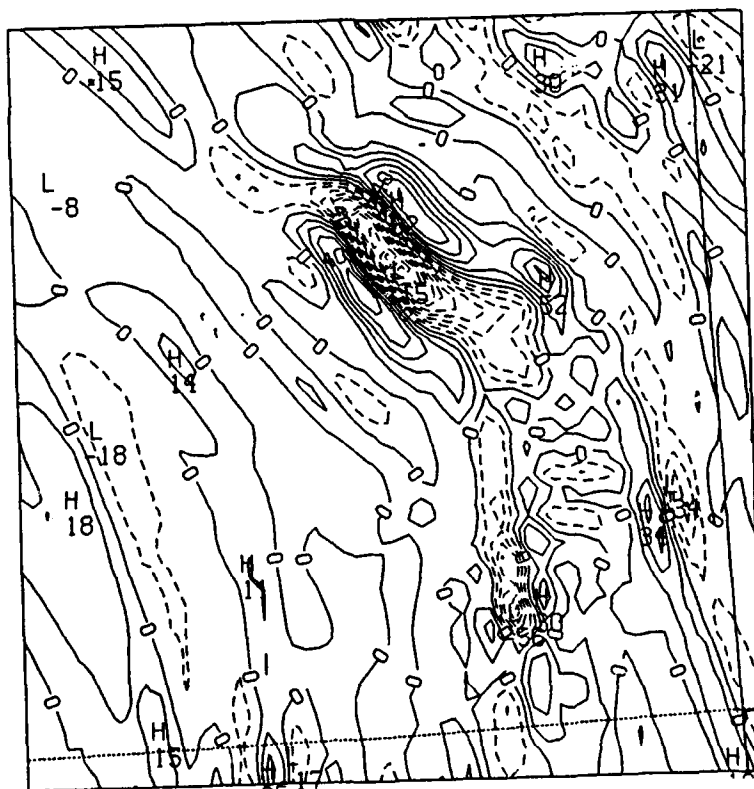
c



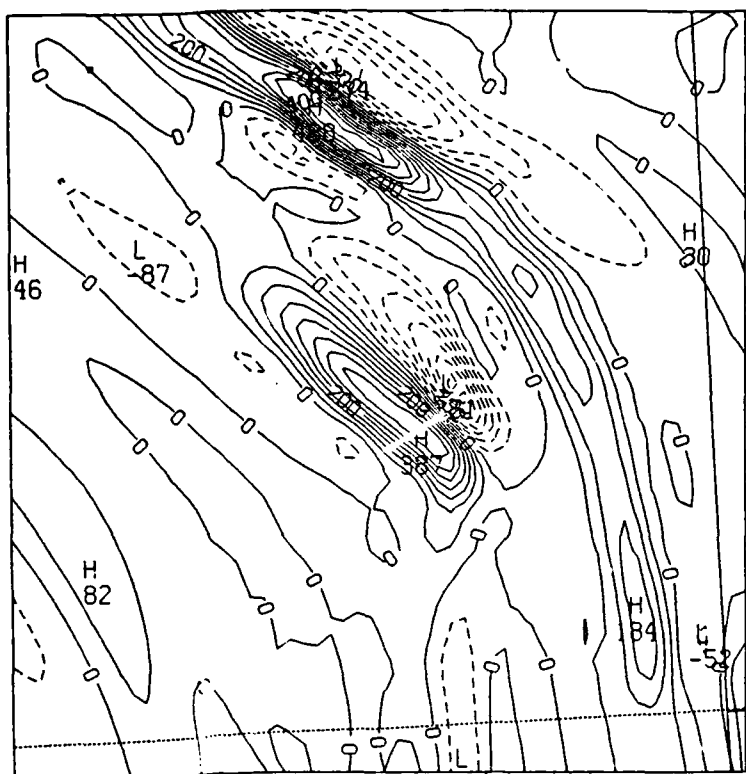
d



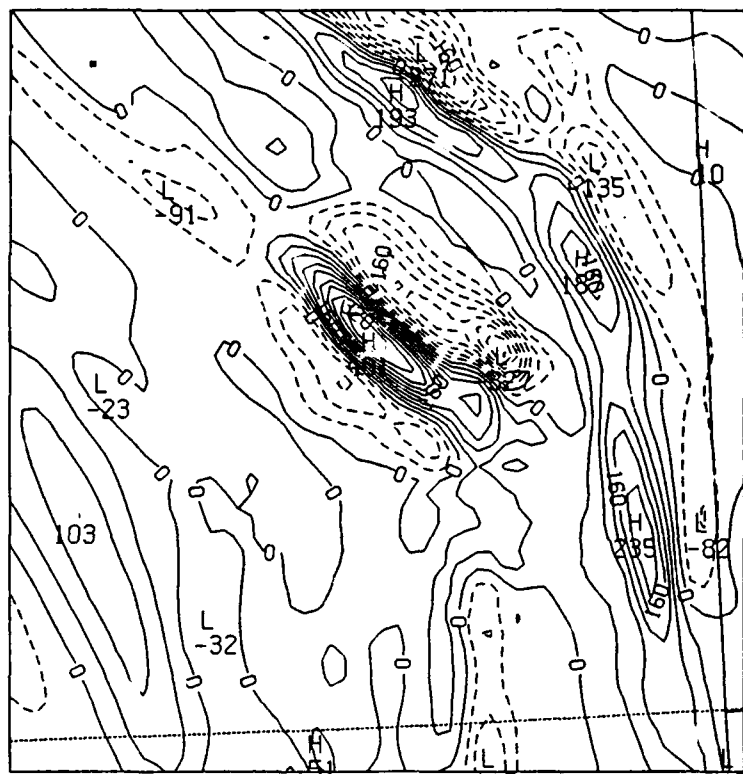
e



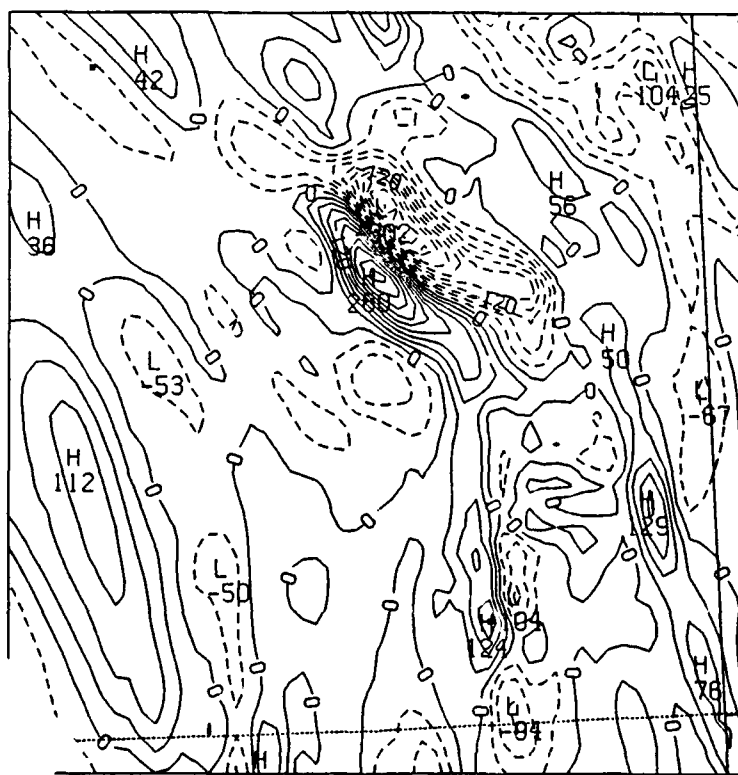
f



j

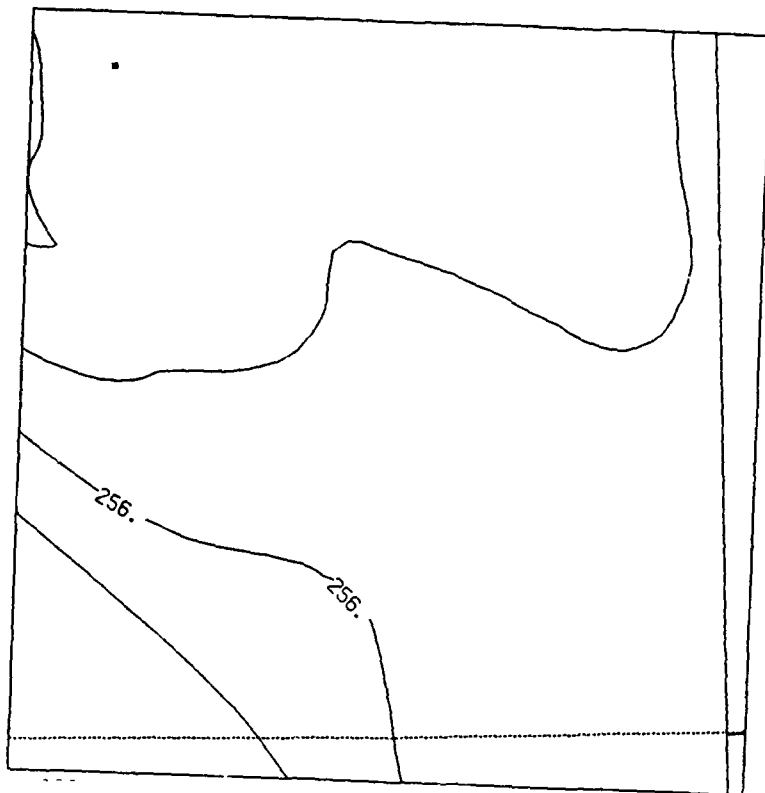


k

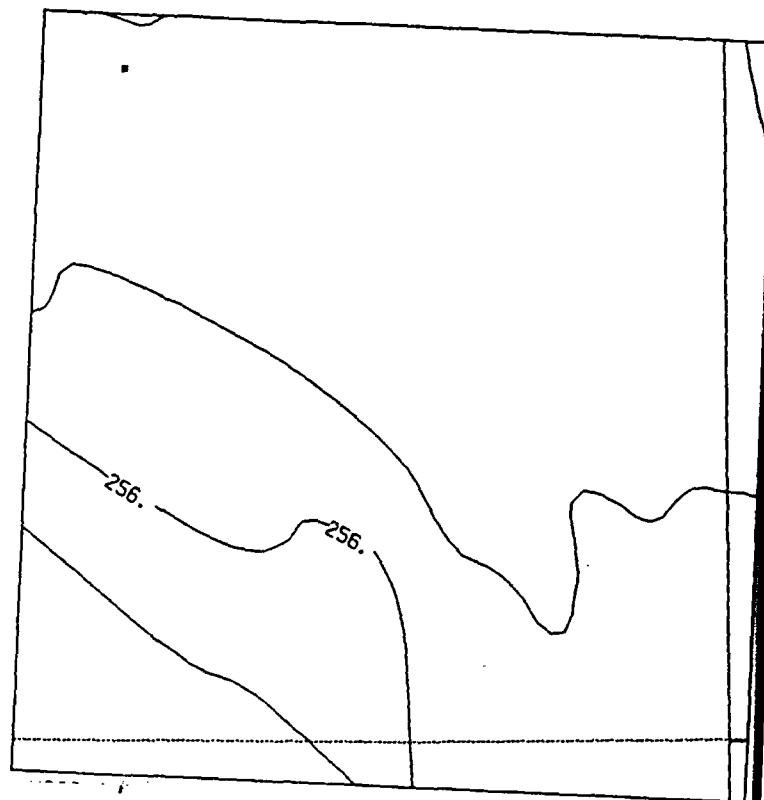


5

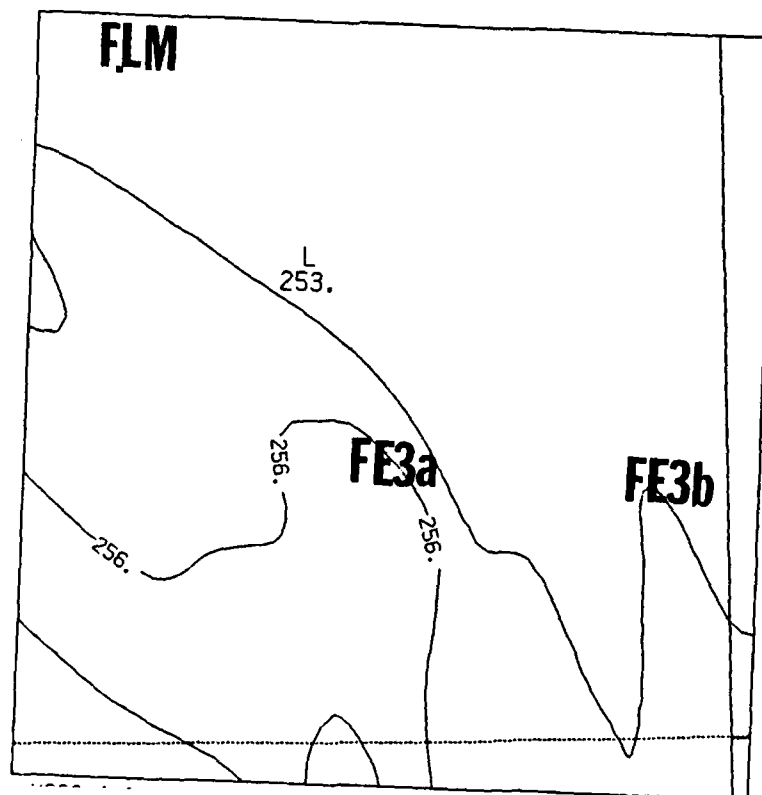
l



m

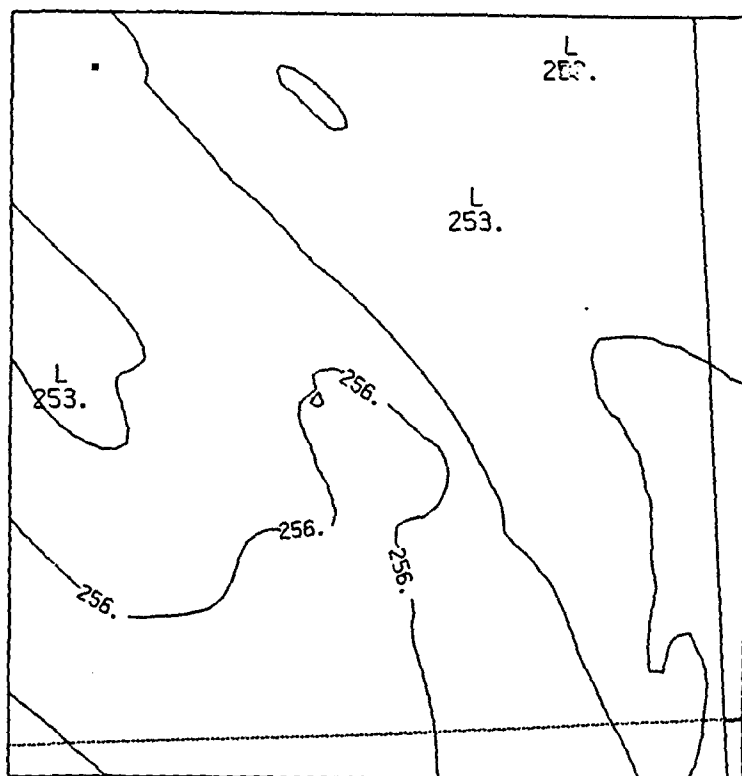


n

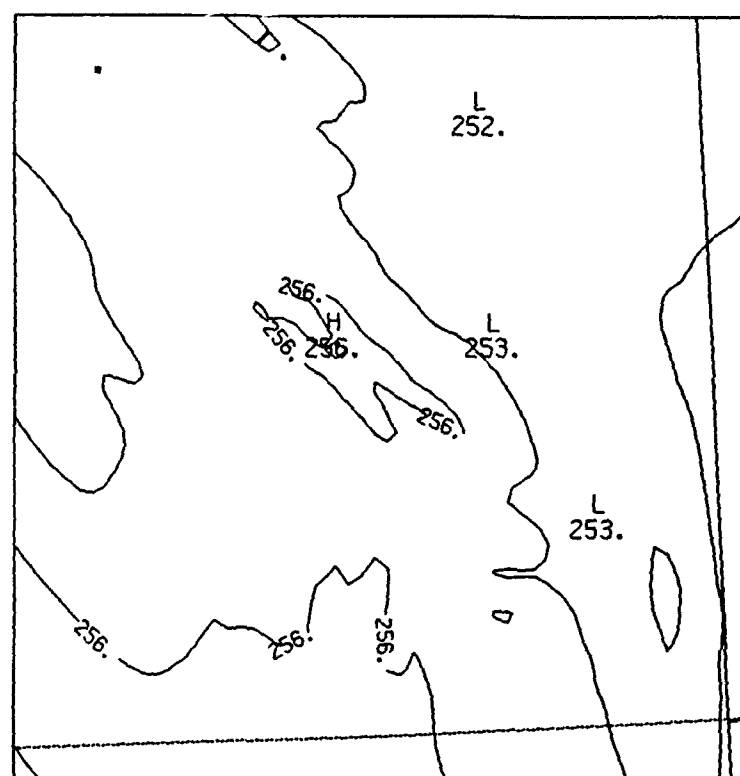


5

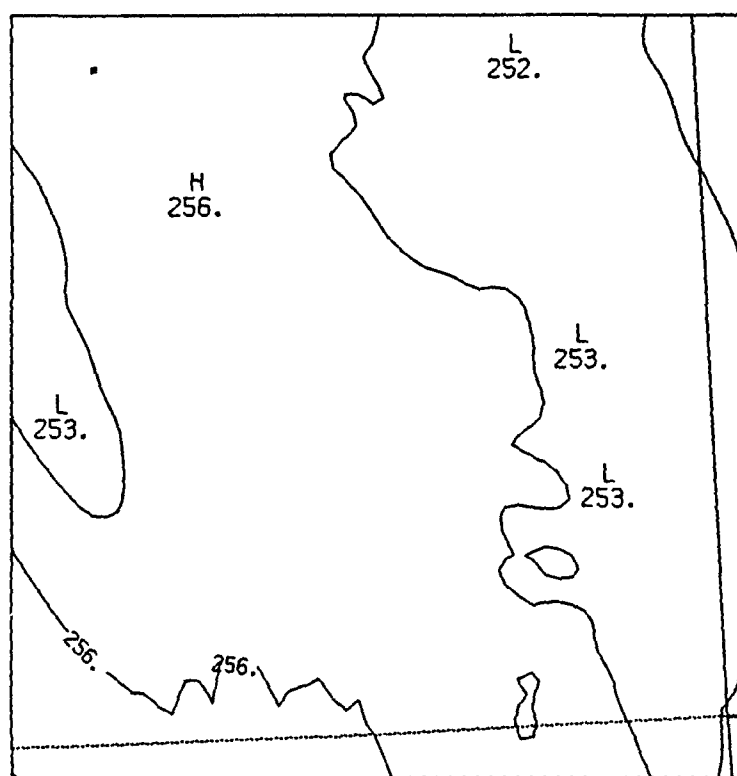
0



p

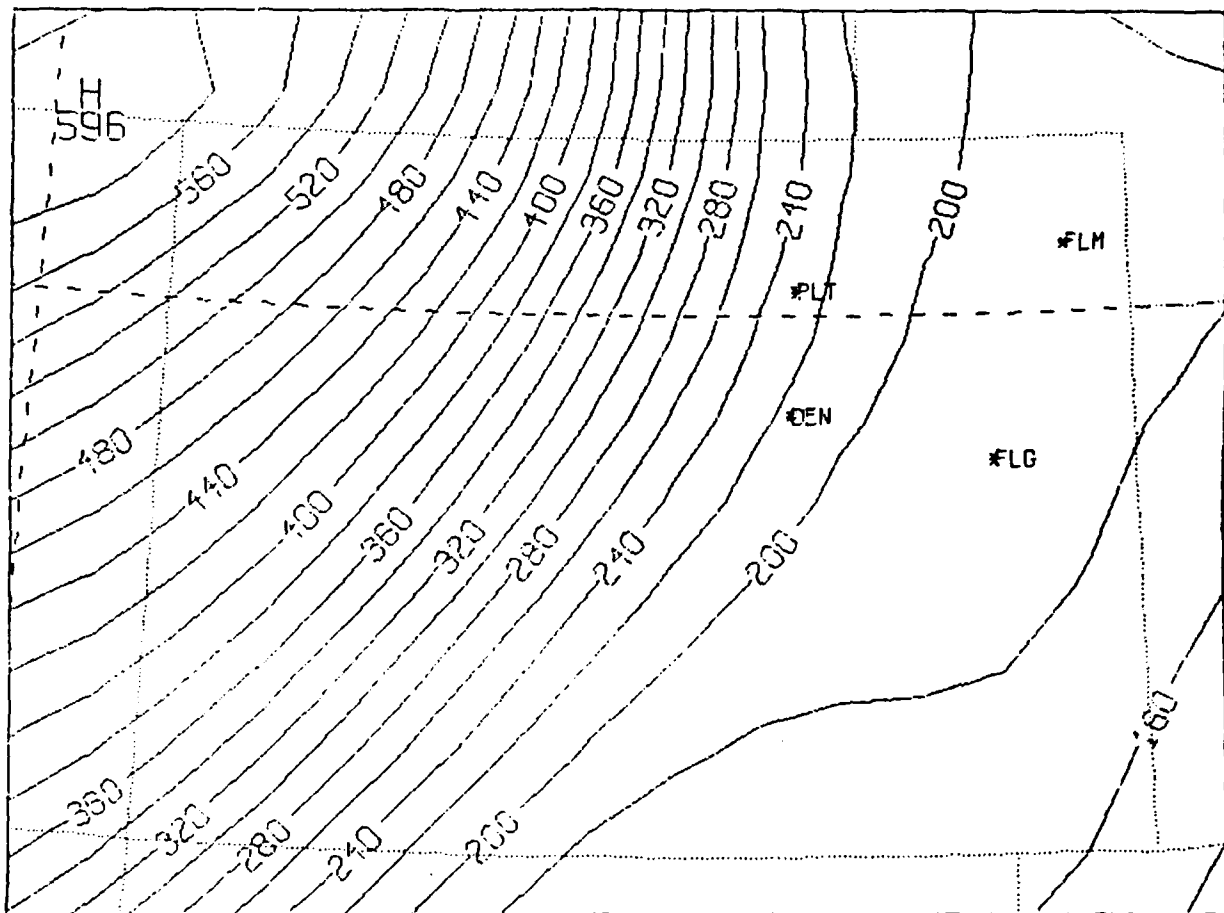


q

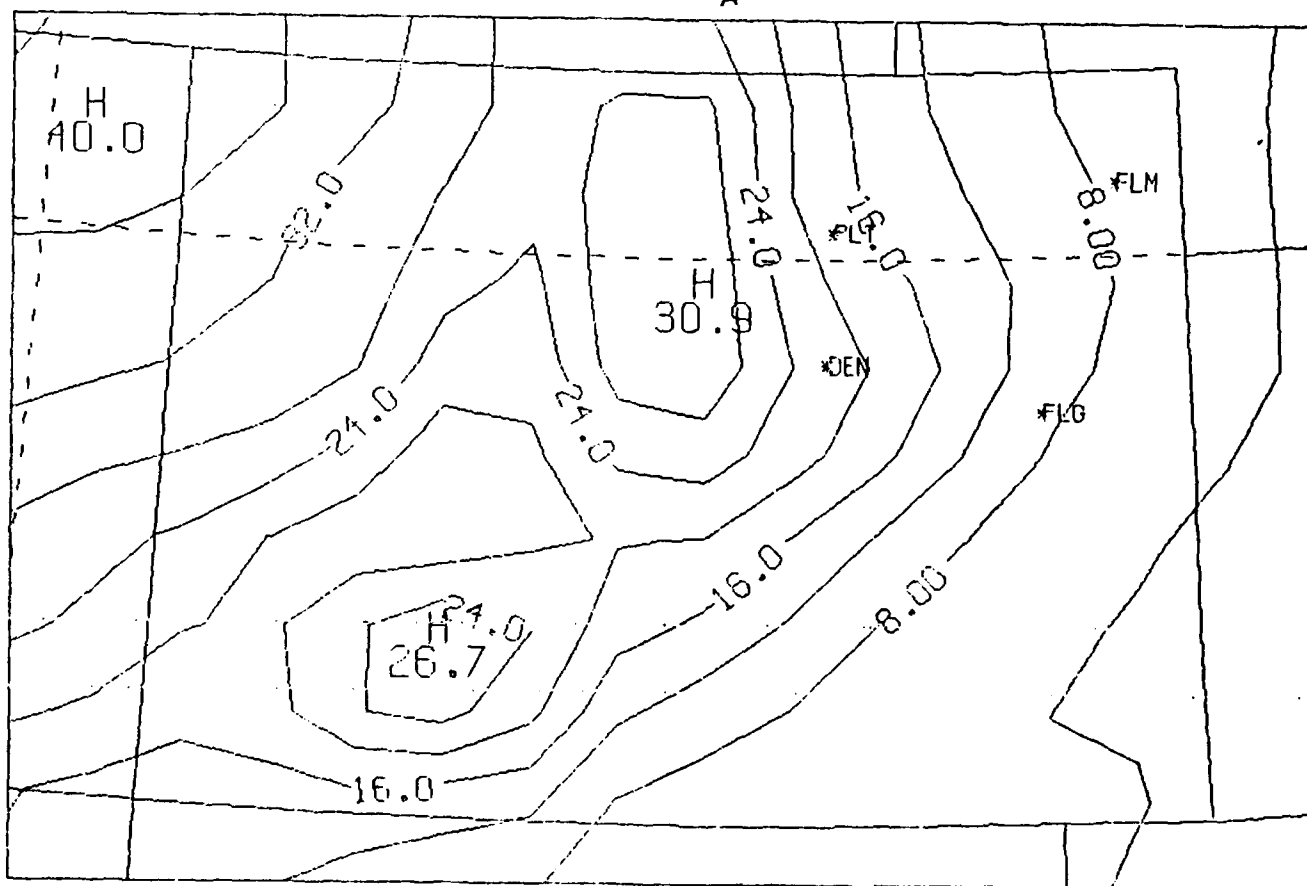


5

r



A

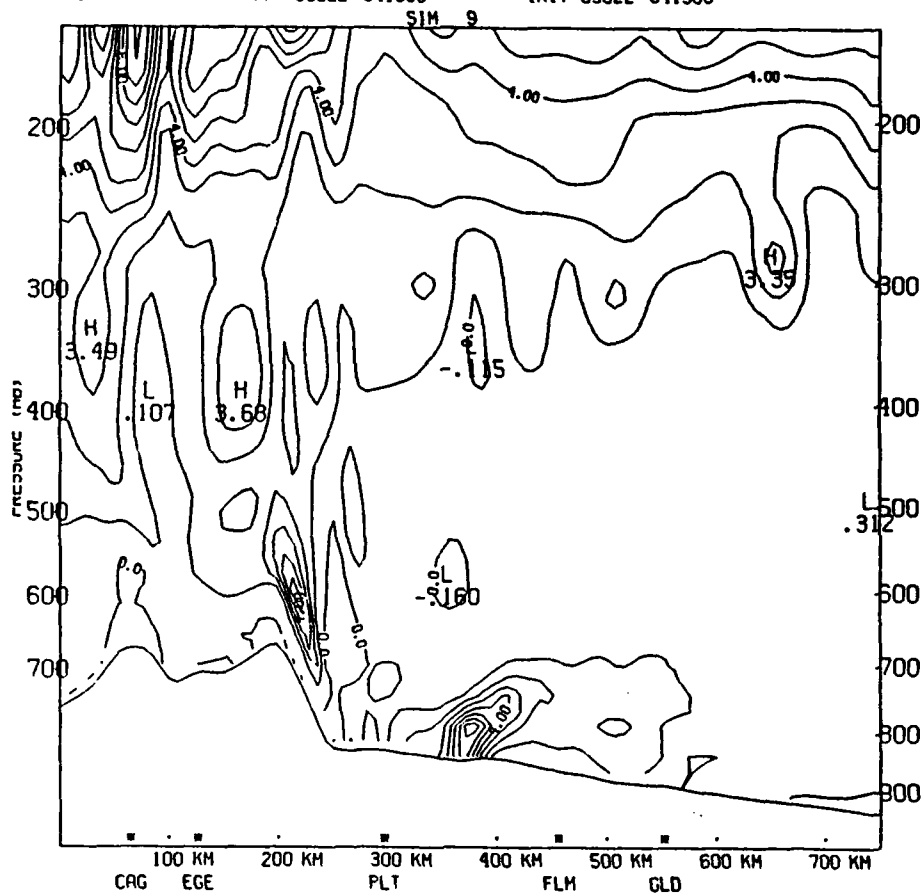


B

FVORT

VT 0902Z 041386

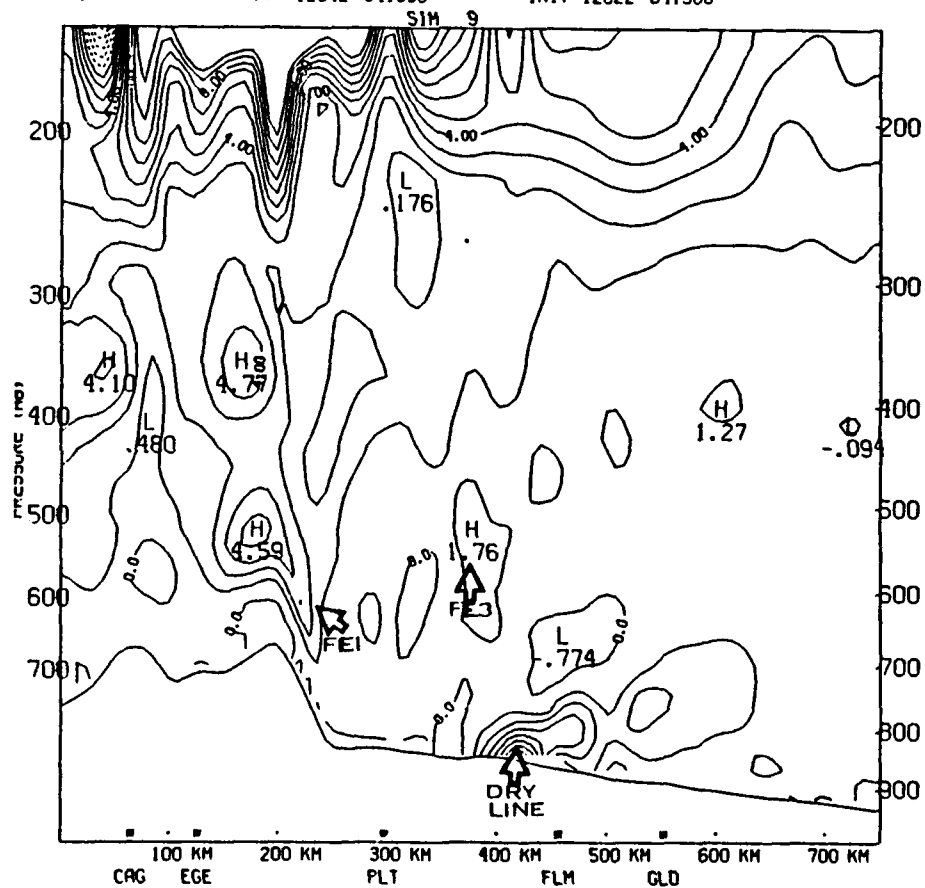
INIT 0902Z 041386

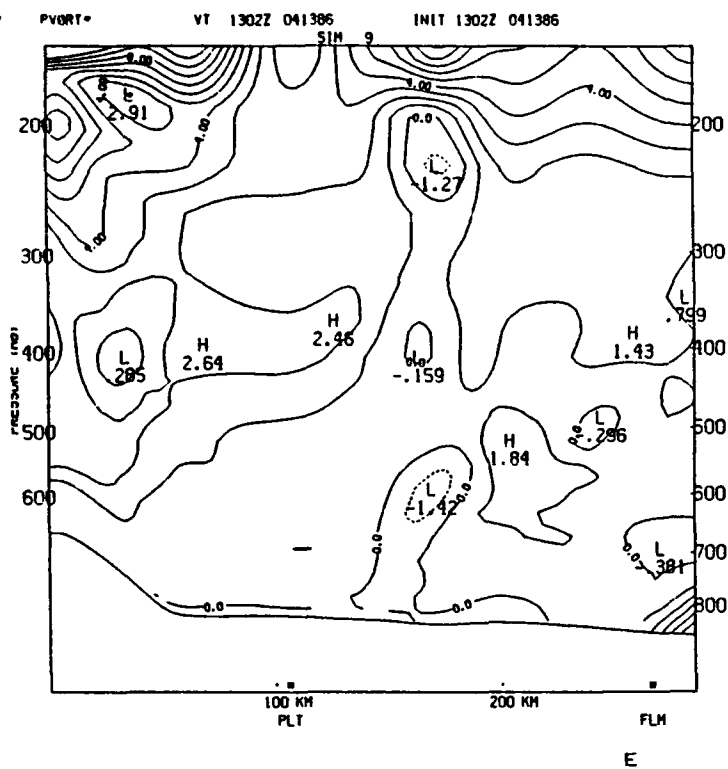


FVORT

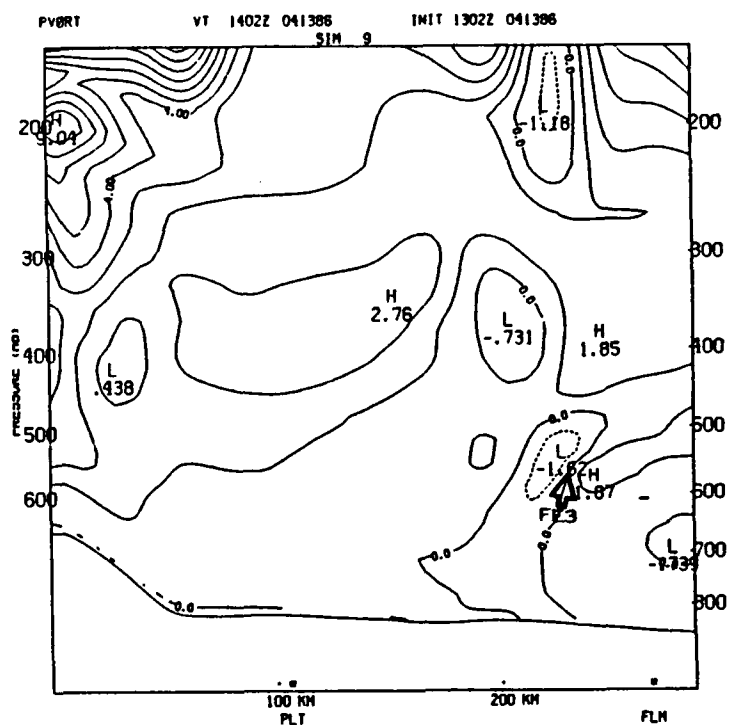
VT 1202Z 041386

INIT 1202Z 041386

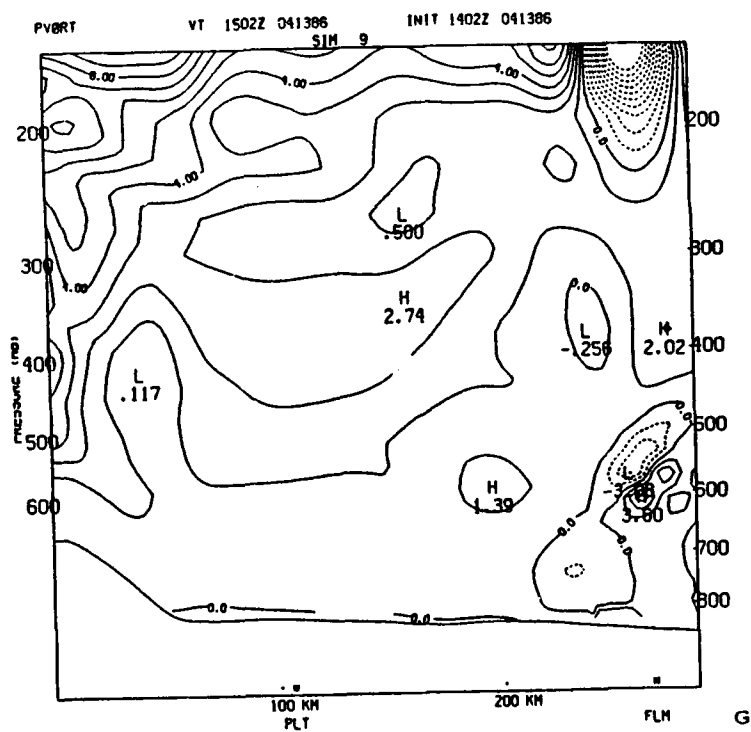




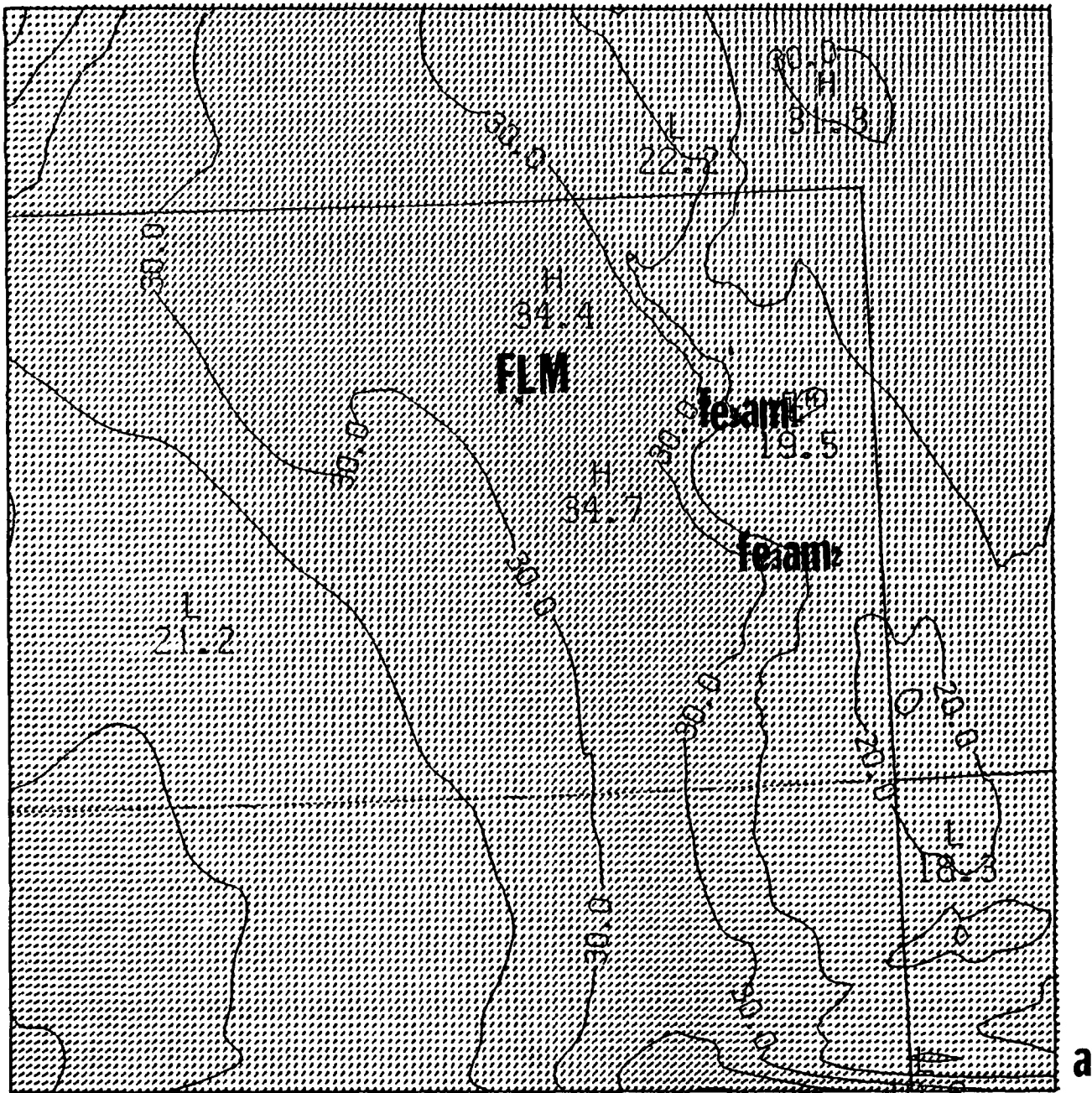
E

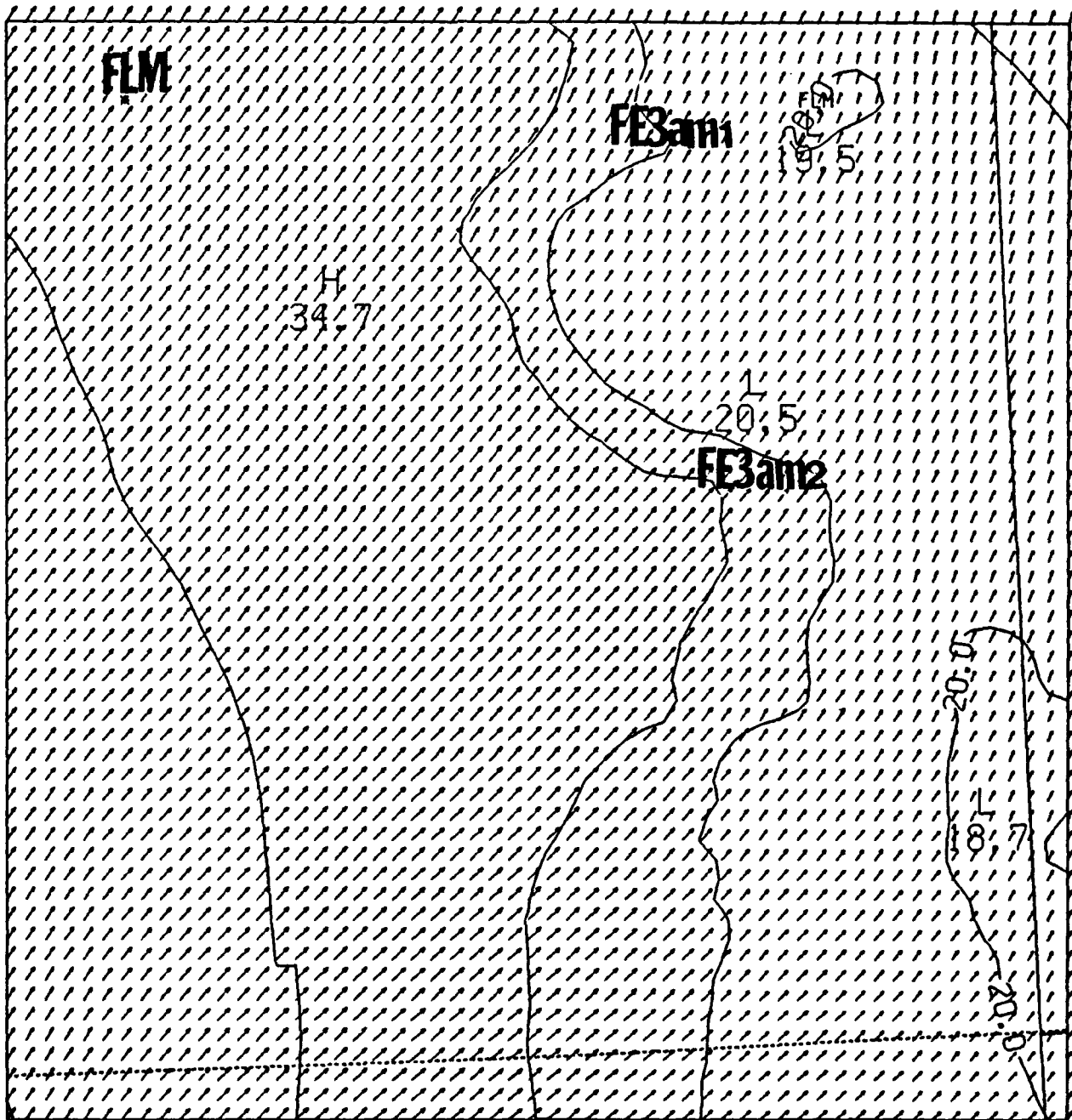


F

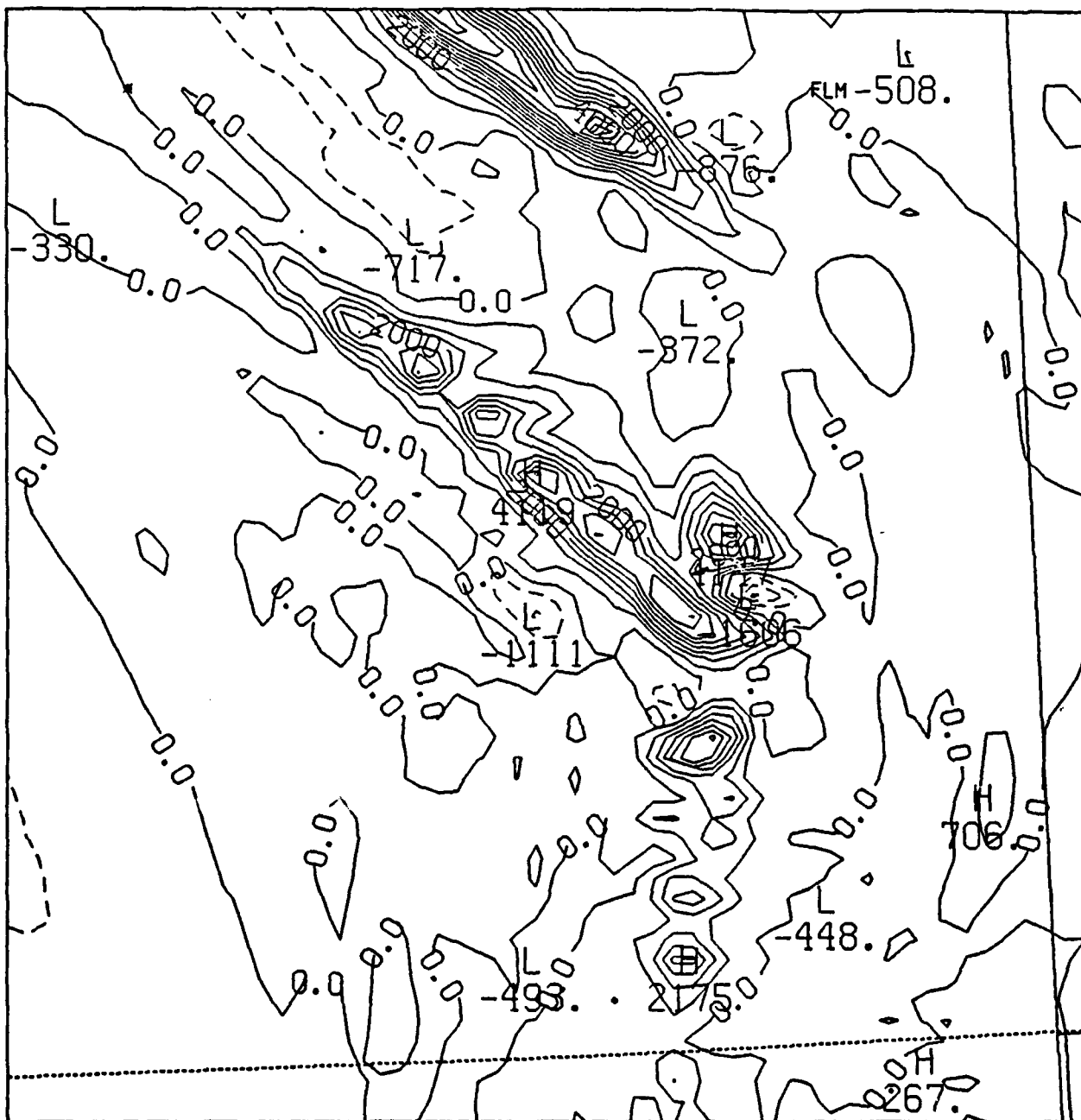


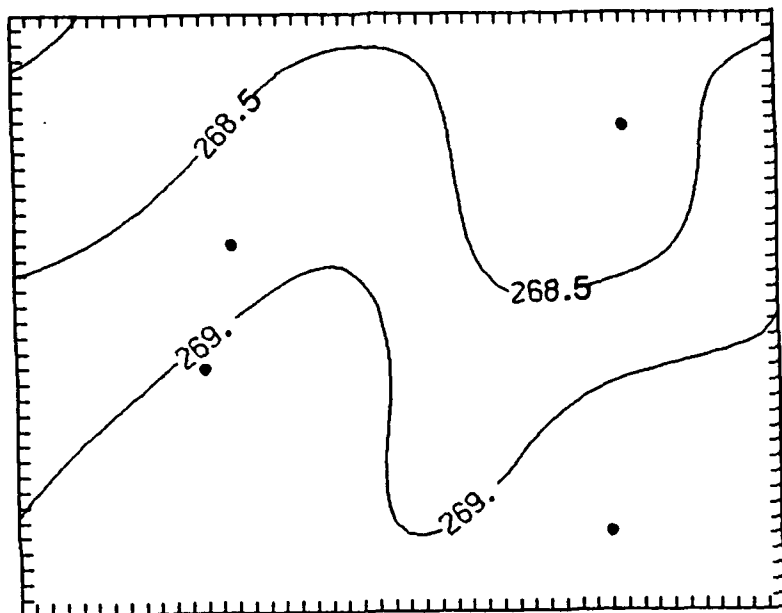
G



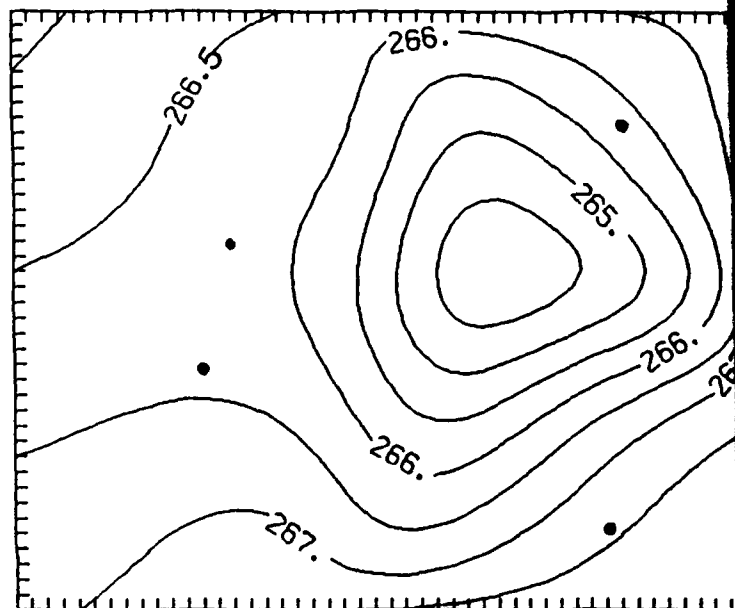


b

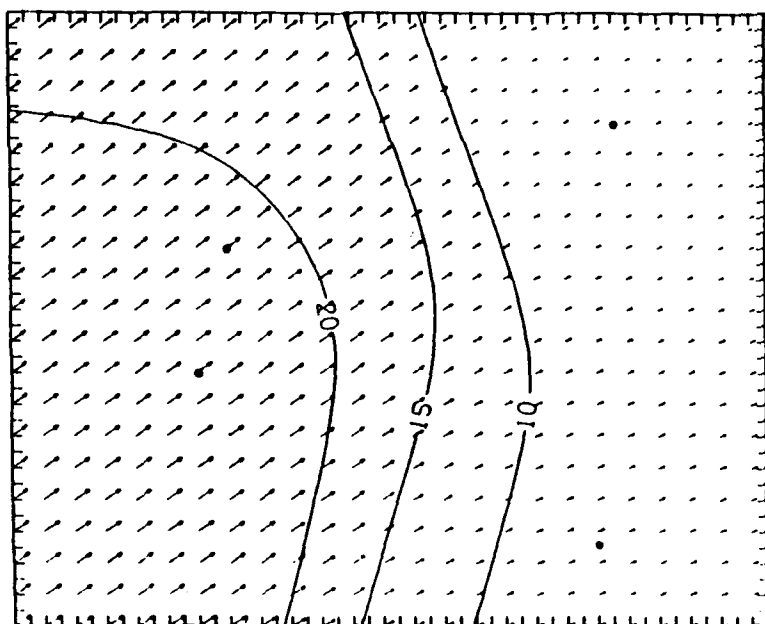




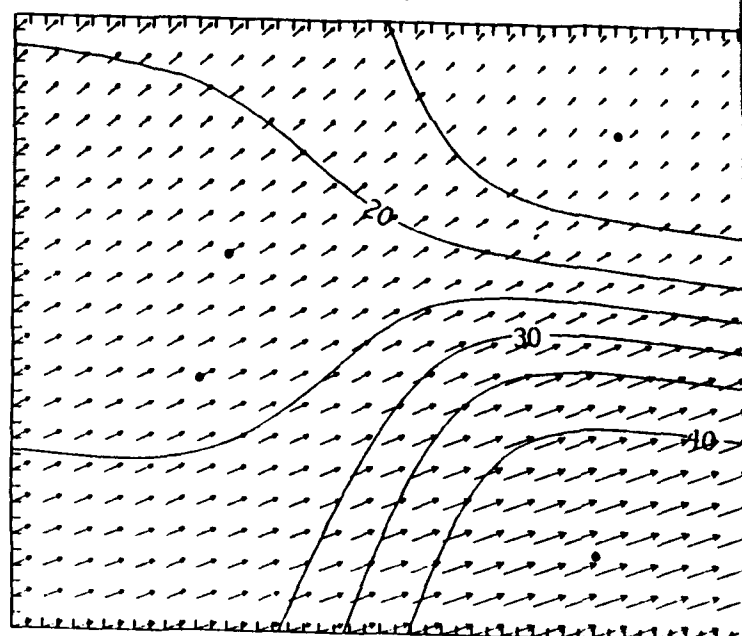
a



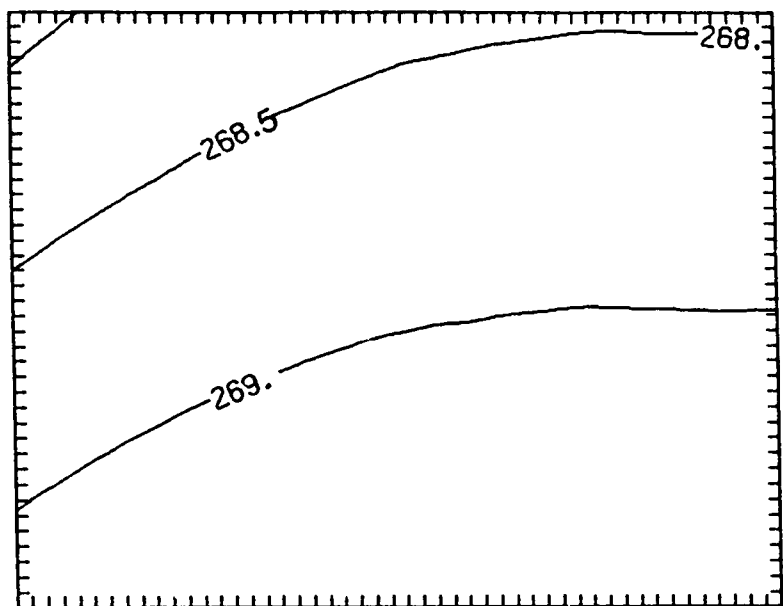
b



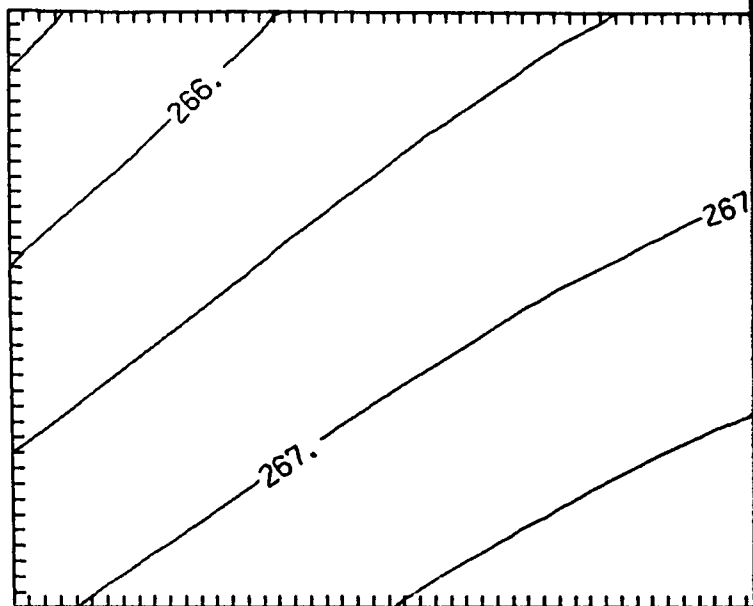
c



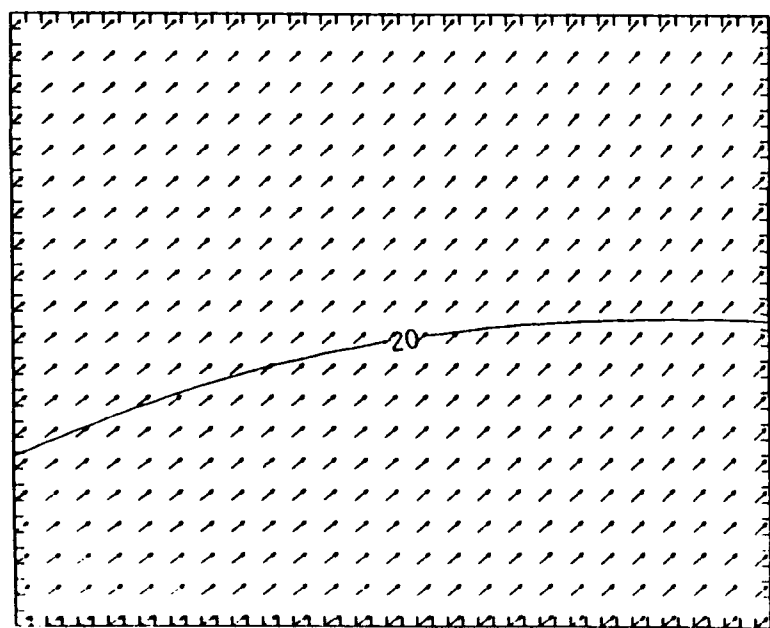
d



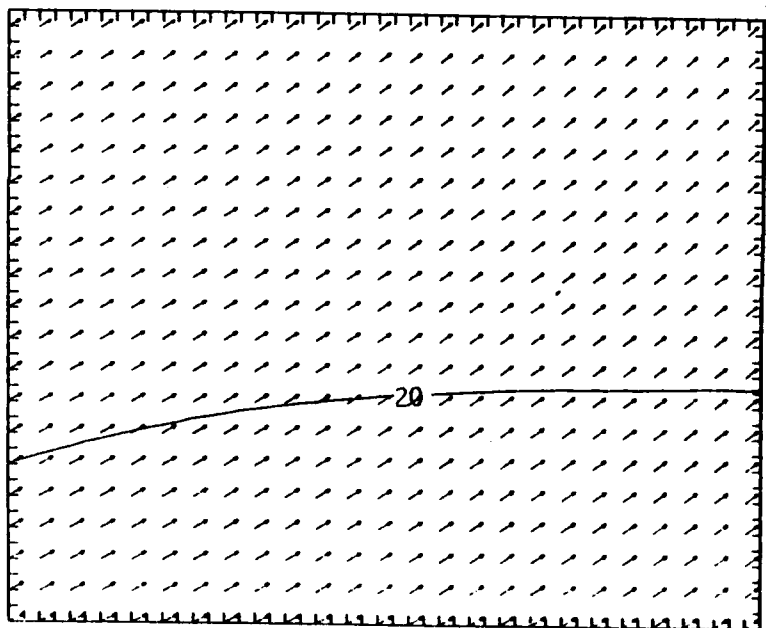
e



f

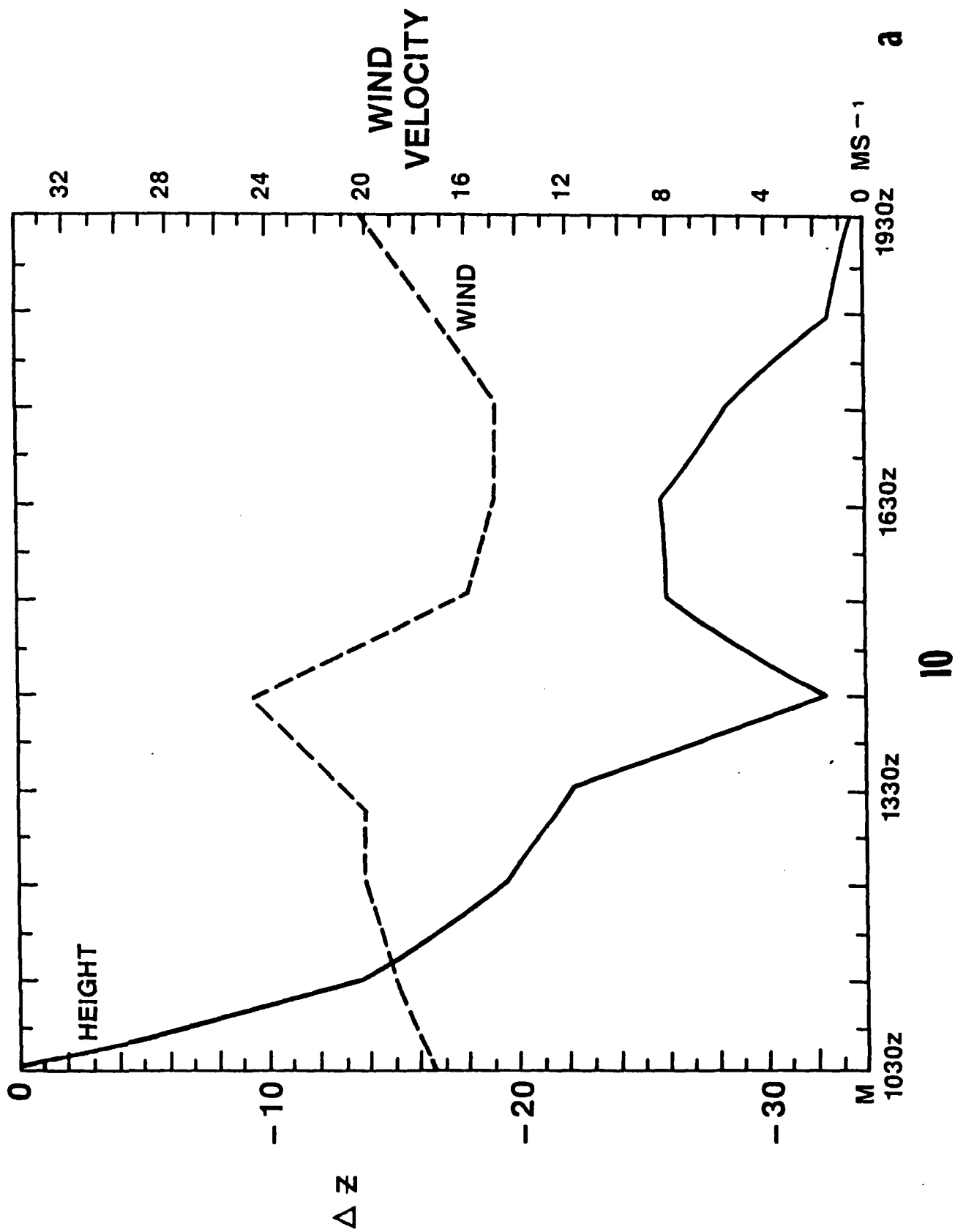


g



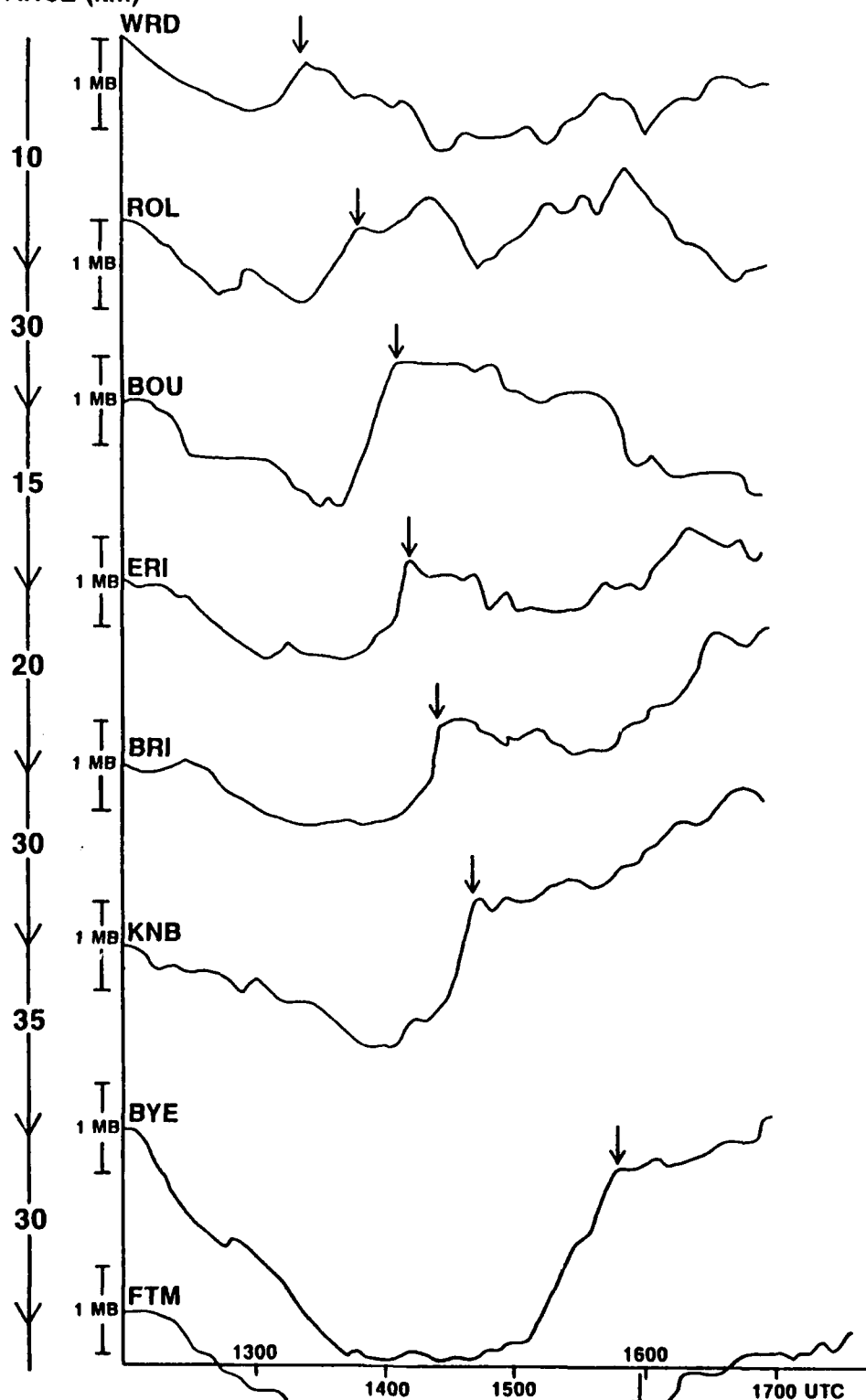
h

60 kPa PROFILER HEIGHT AND WIND CHANGE



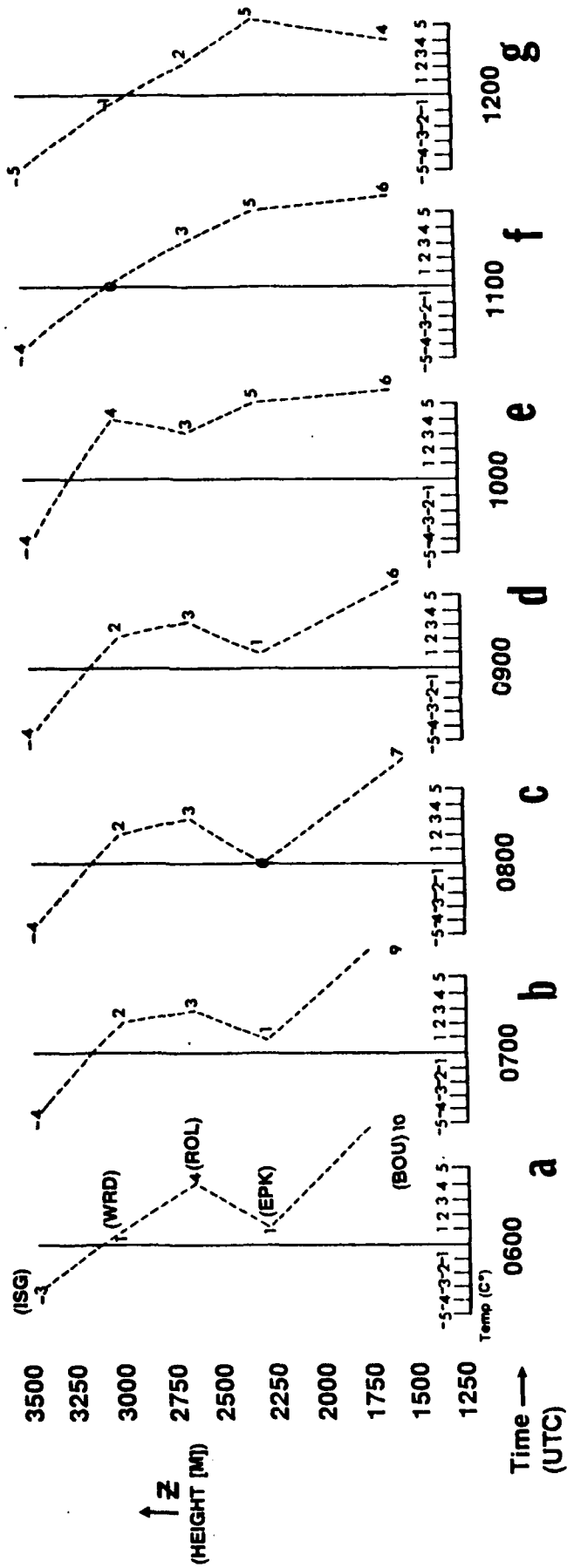
MESONETWORK MICROBAROGRAPH TRACES

WEST—EAST
DISTANCE (km)



b

RECONSTRUCTED SOUNDING ABOVE FRONT RANGE



RECONSTRUCTED FRONT RANGE SOUNDING WIND PROFILE

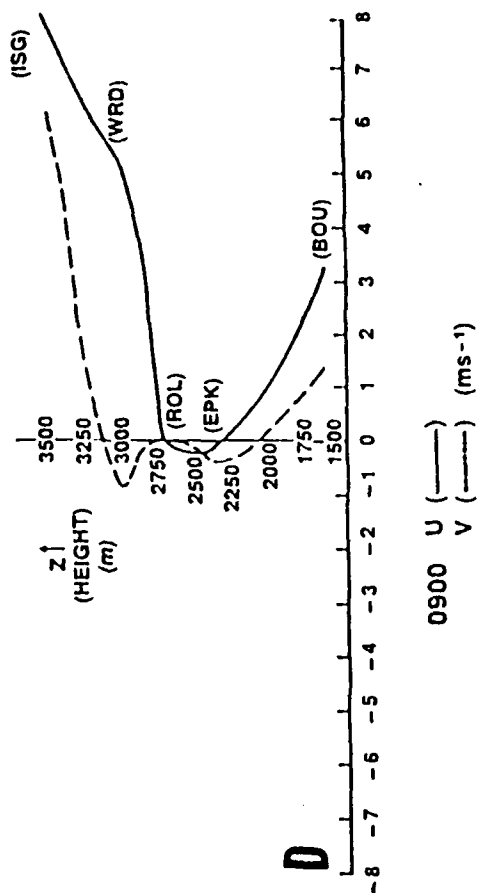
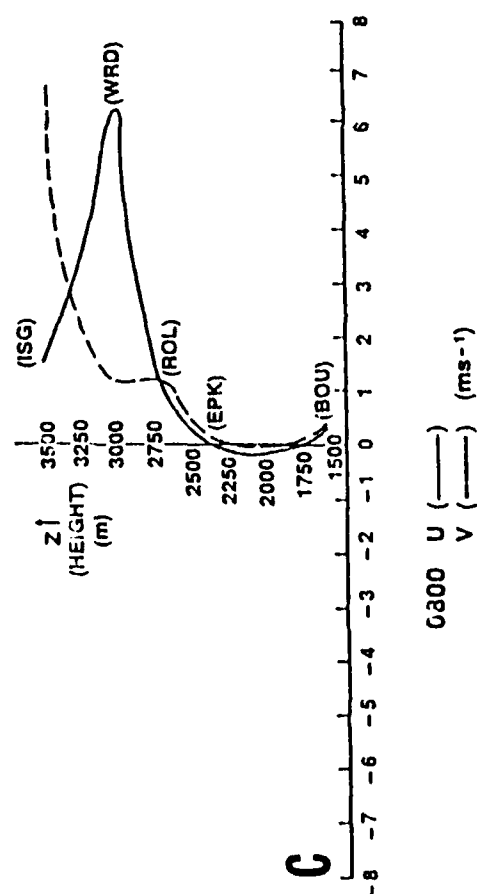
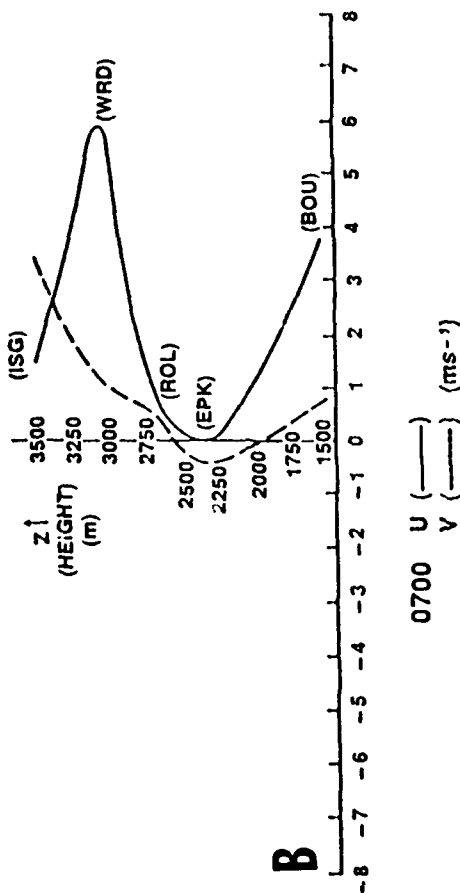
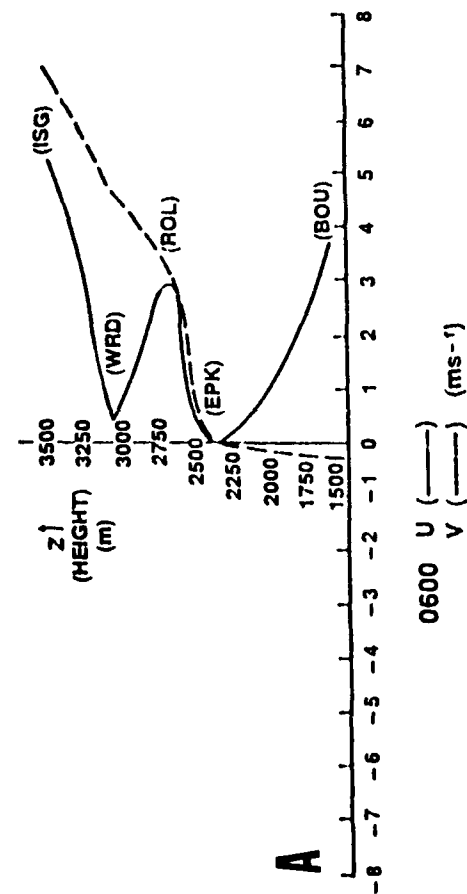
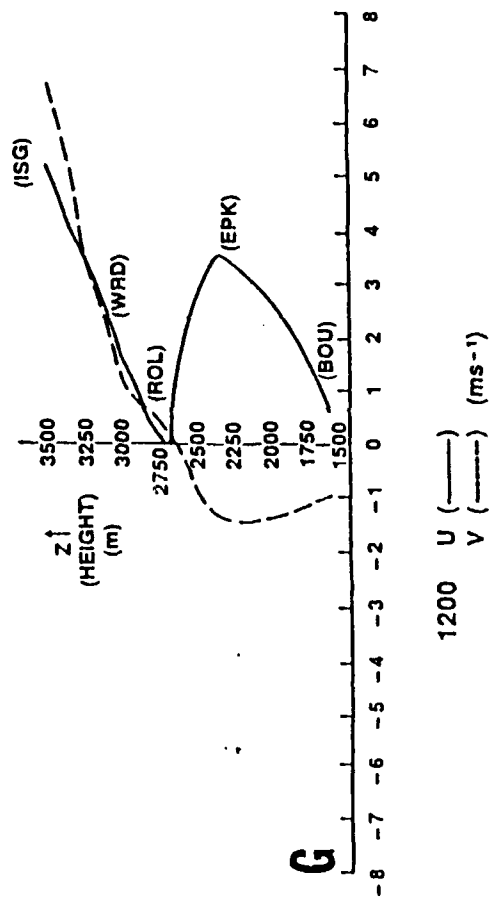
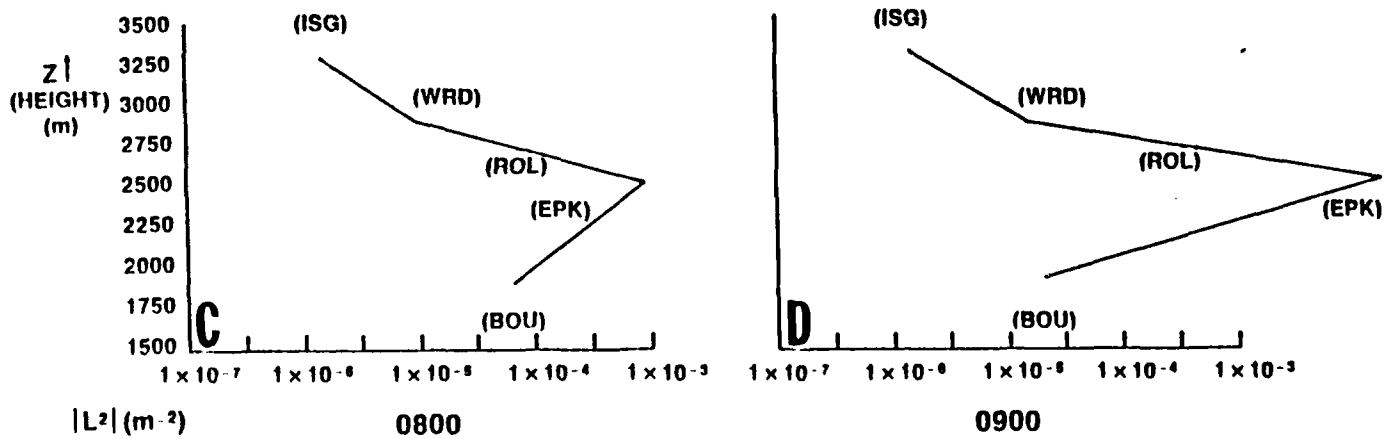
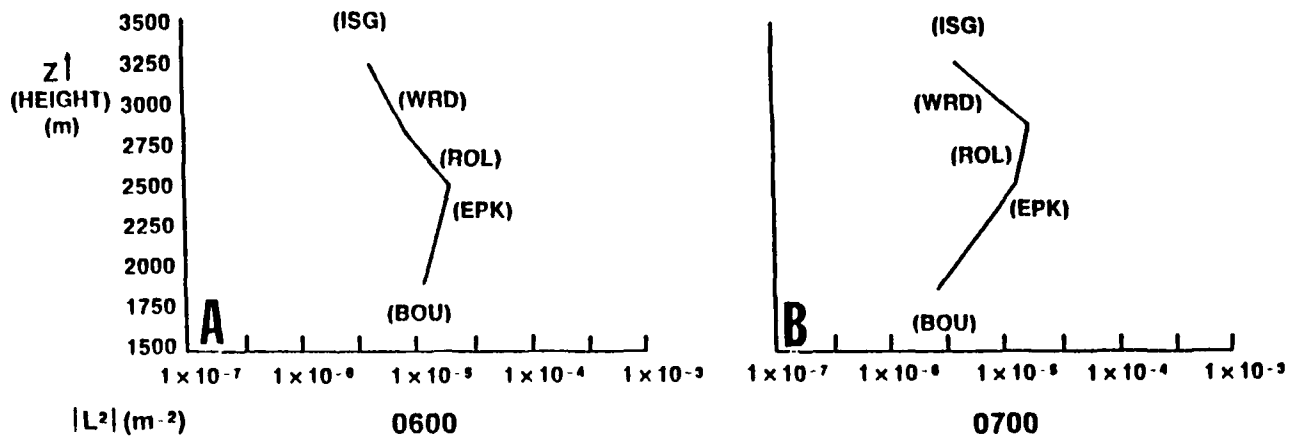


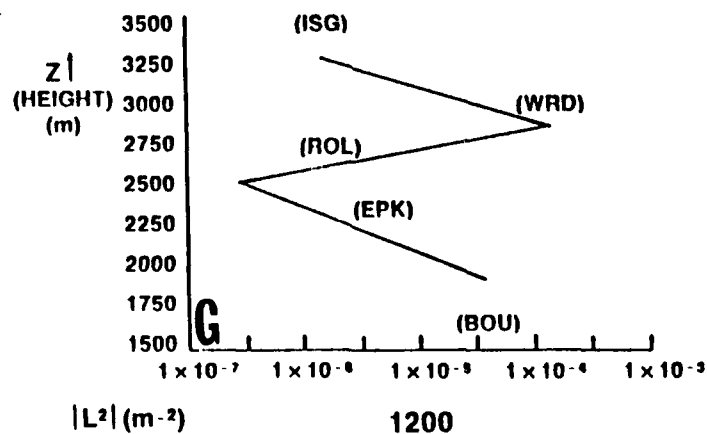
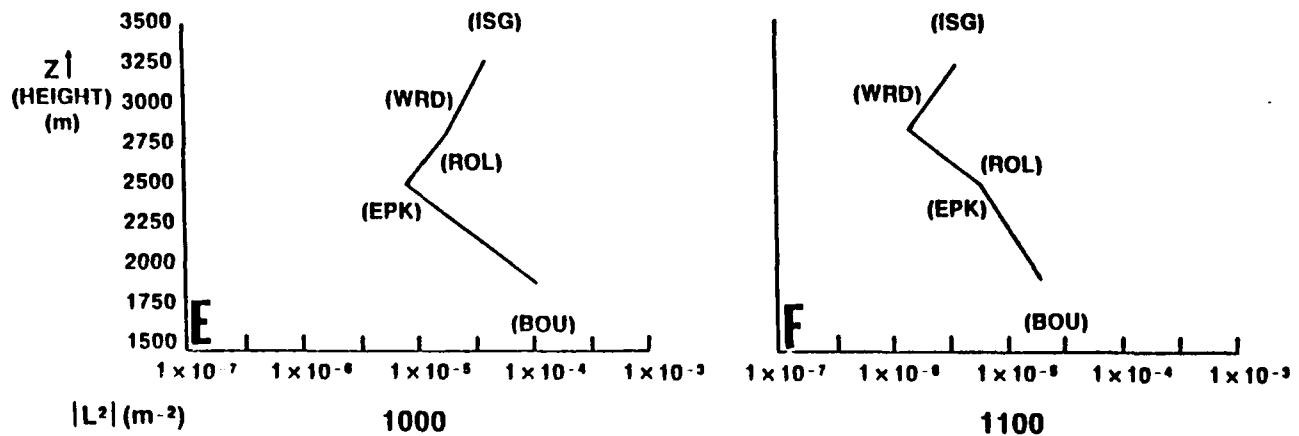
Figure 1 consists of two cross-sections of the atmosphere, labeled E and F, showing height (z) in meters versus distance in degrees. Both plots show a solid line for the 1100 U wind profile and a dashed line for the 1100 V wind profile. Key features include the (ISG) jet, (WRD) wind reversal, (ROL) wind reversal, (EPK) wind peak, and (BOU) wind peak. The y-axis ranges from 1500 to 3500 m, and the x-axis ranges from -8 to 8 degrees.

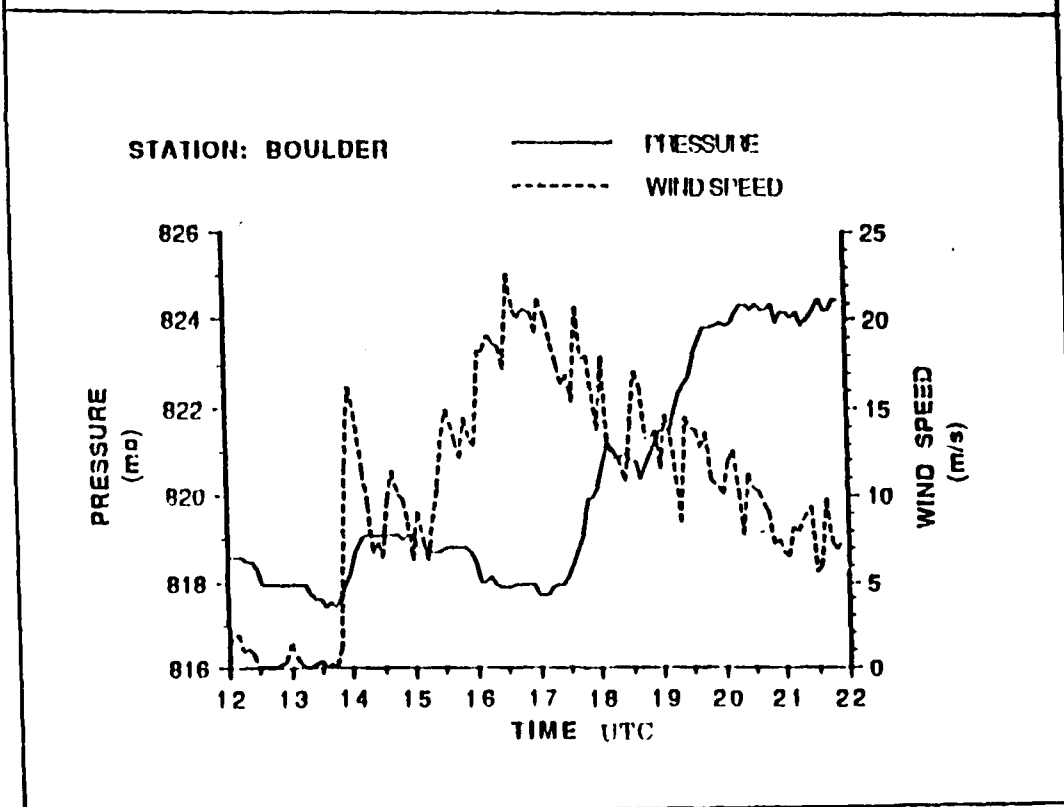
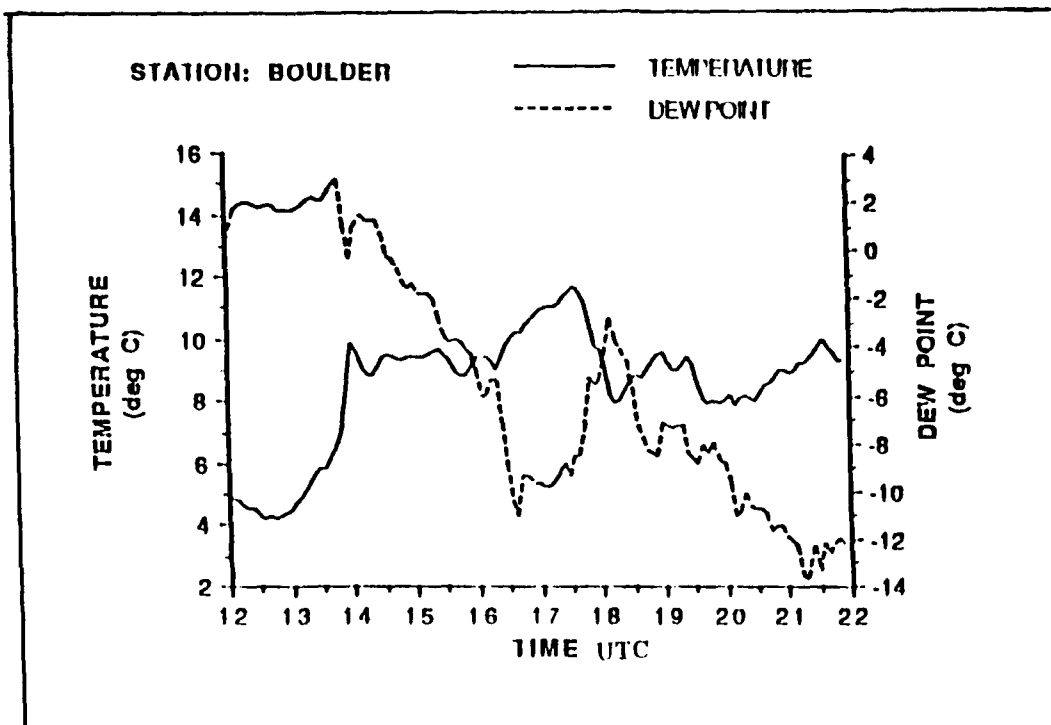


RECONSTRUCTED FRONT RANGE SOUNDING SCORER PARAMETER

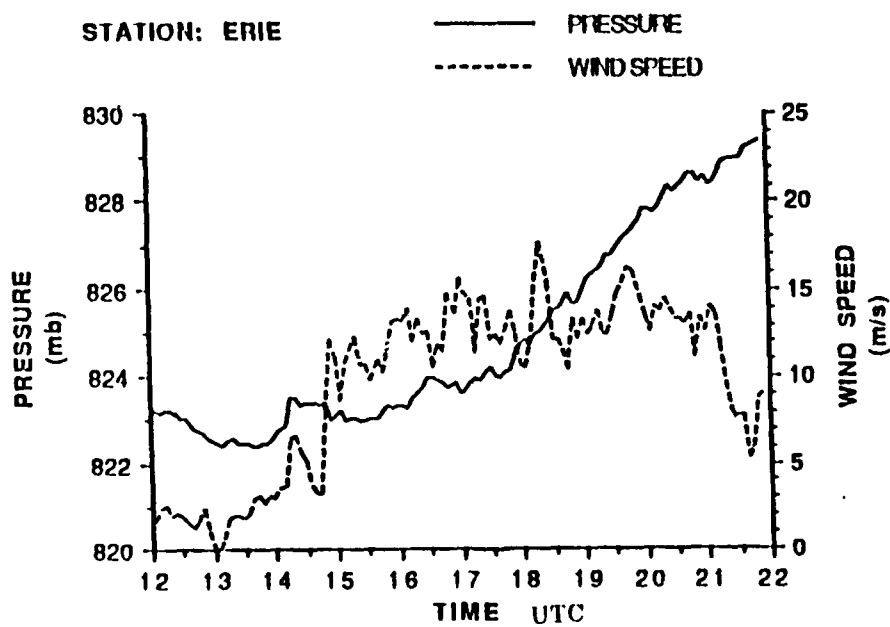
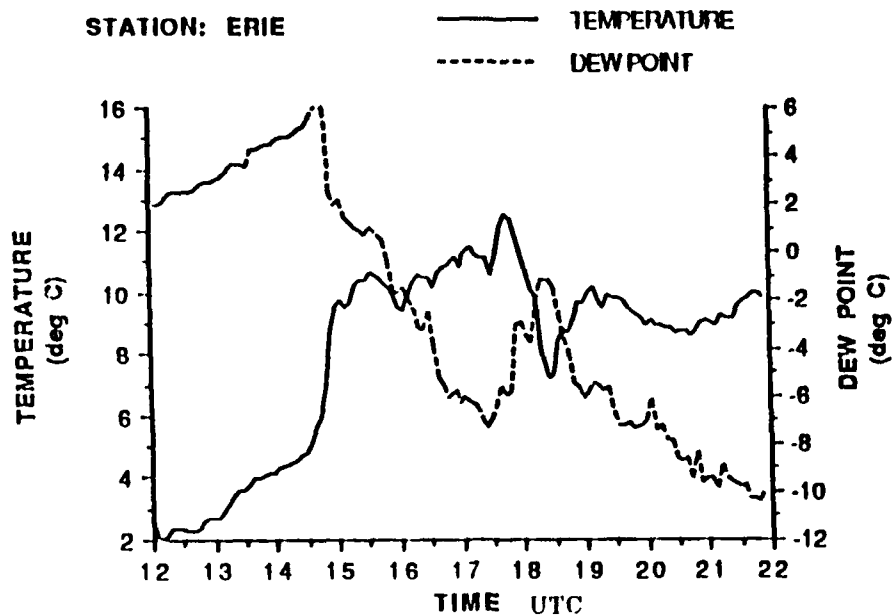


RECONSTRUCTED FRONT RANGE SOUNDING SCORER PARAMETER (Continued)





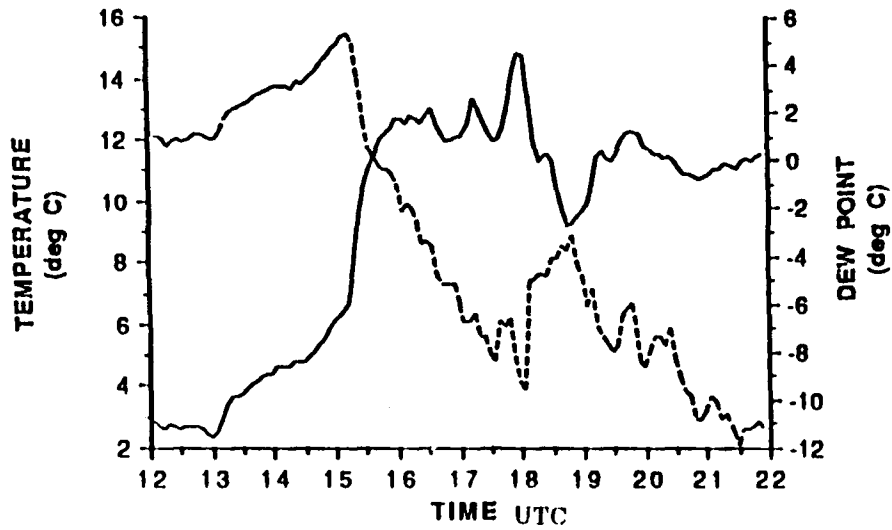
a



b

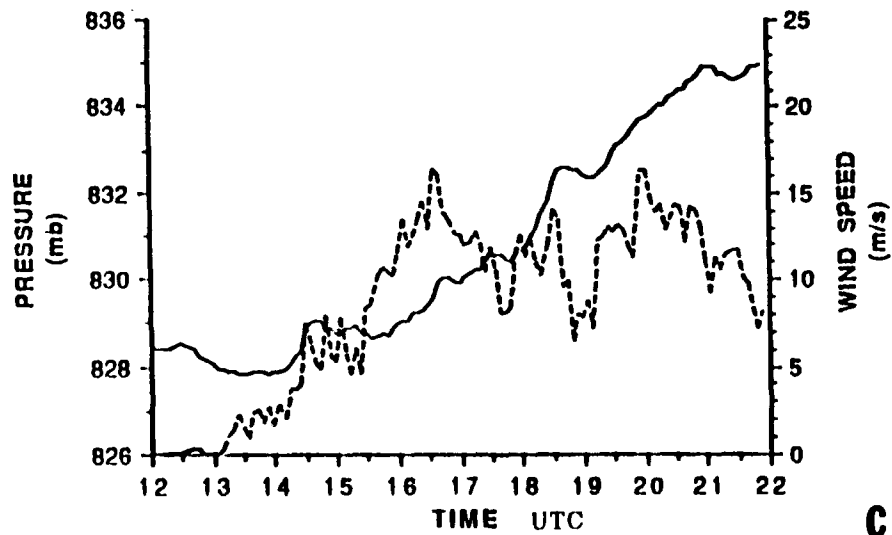
STATION: BRIGHTON

— TEMPERATURE
- - - DEWPOINT

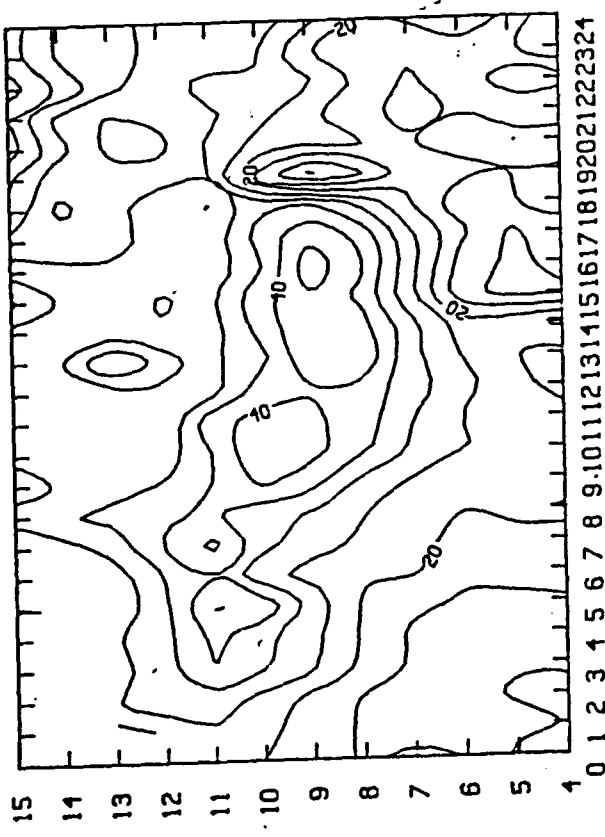


STATION: BRIGHTON

— PRESSURE
- - - WIND SPEED



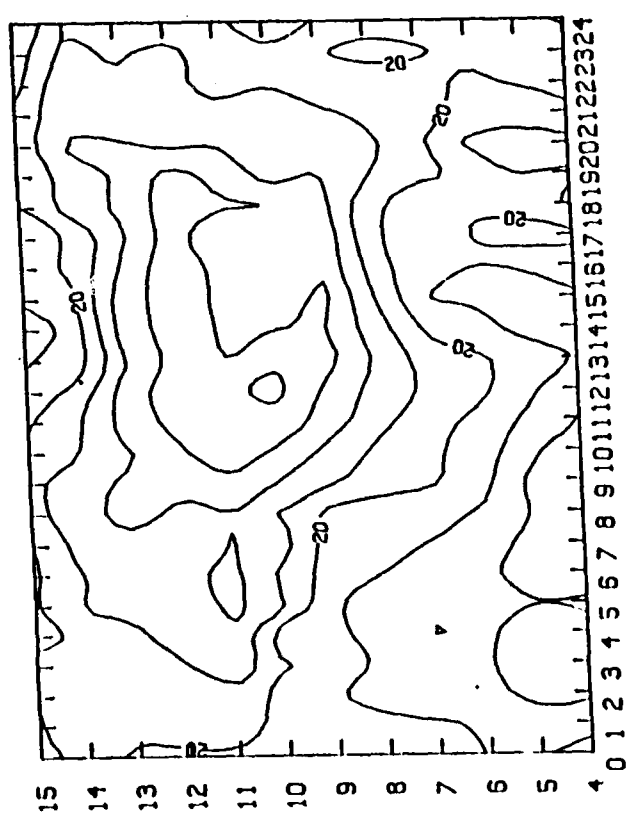
C



A

STA: PLT

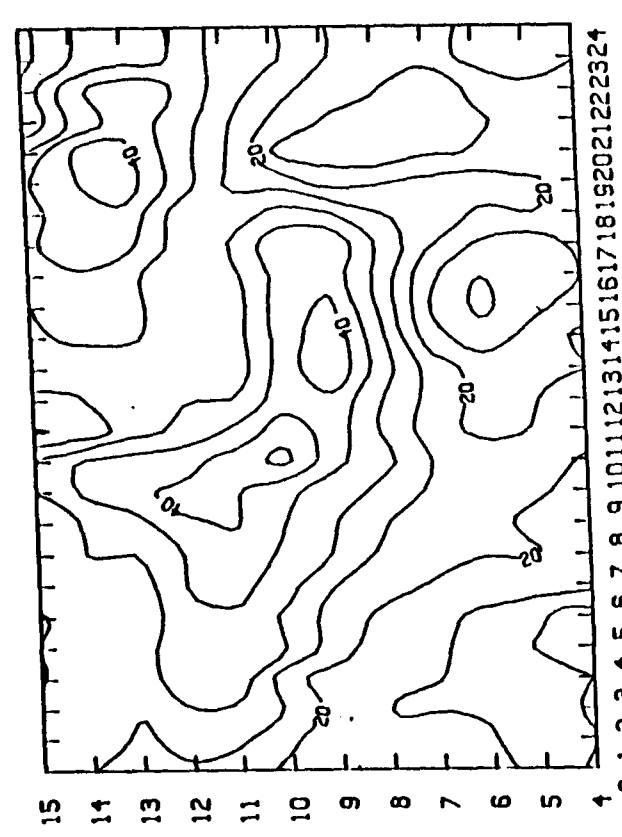
TIME UTC 41385



B

STA: DEN

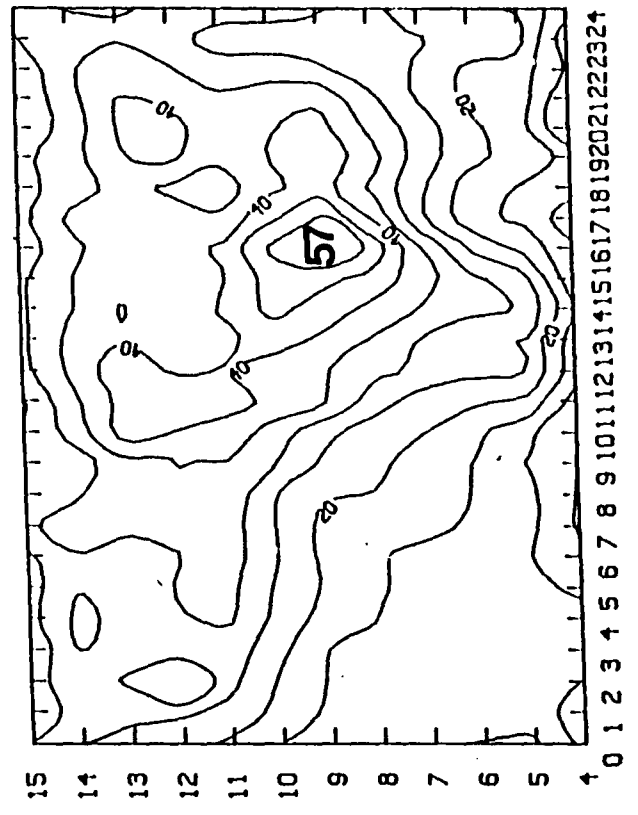
TIME UTC 41386



C

STA: FLG

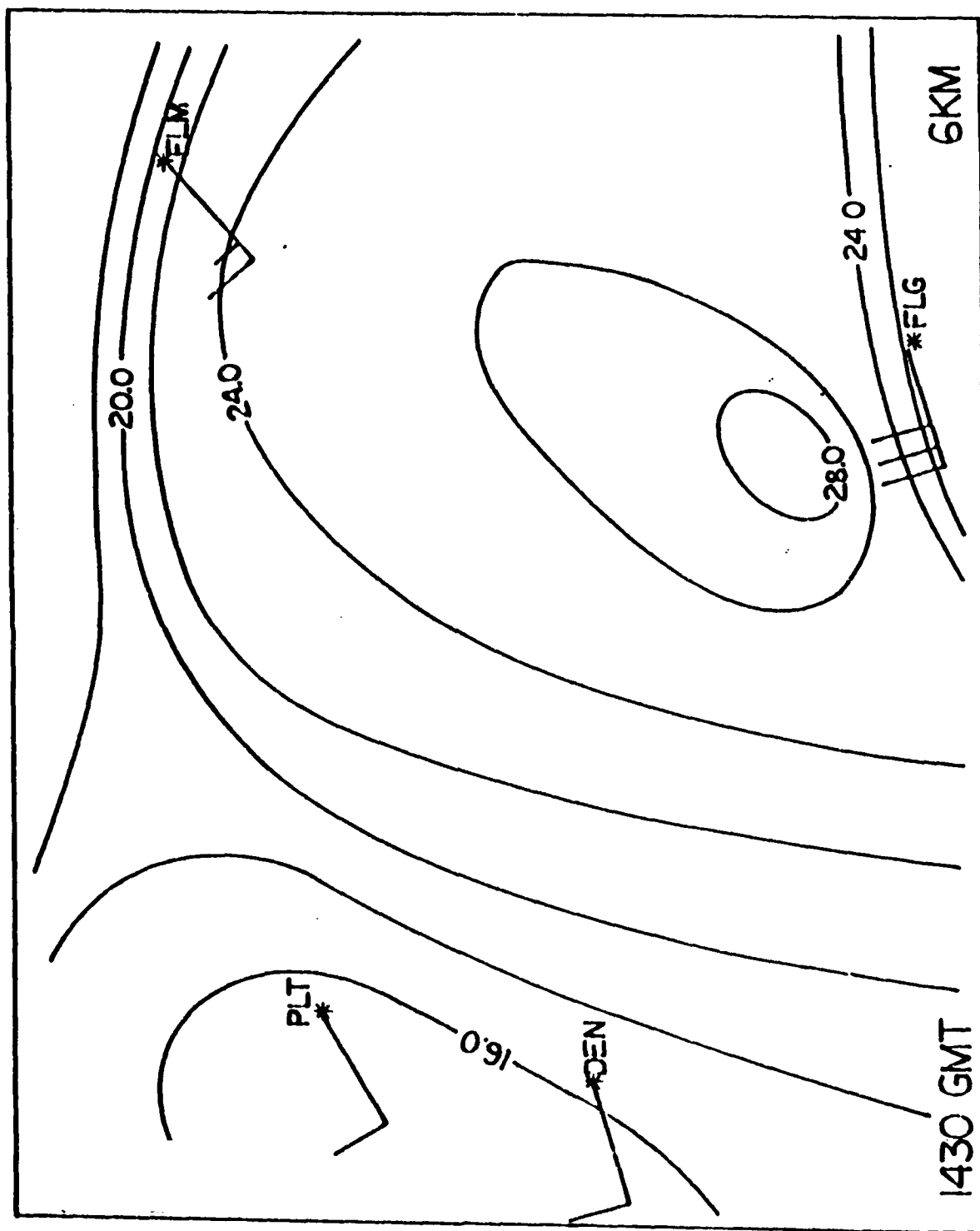
TIME UTC 41386



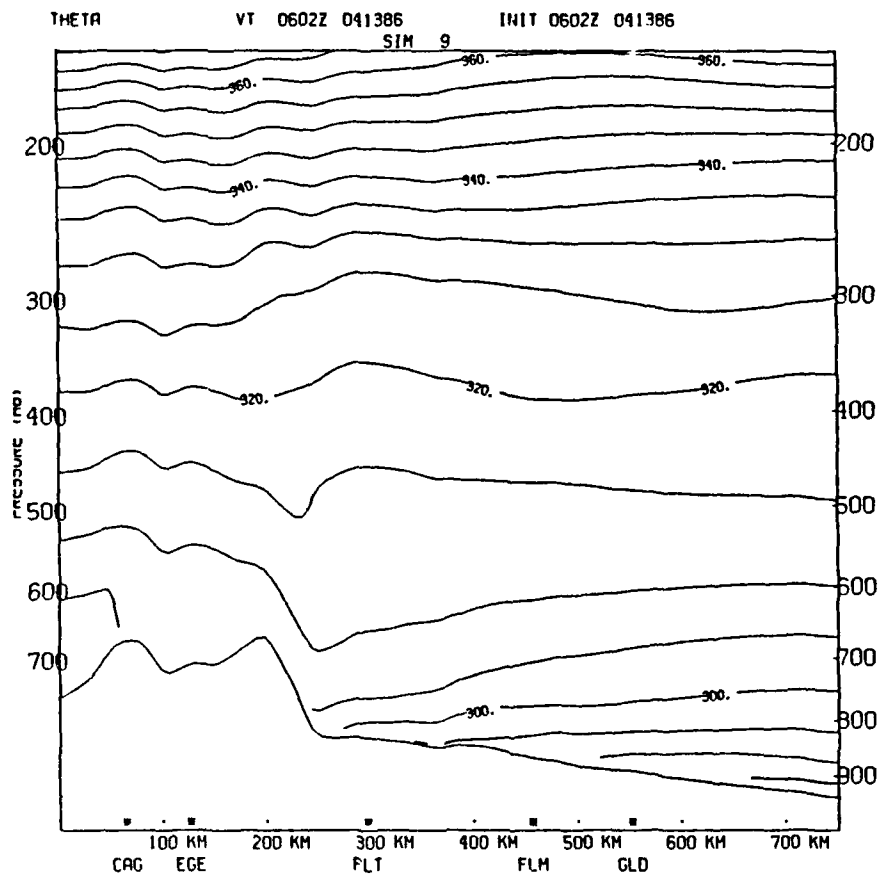
D

STA: FLM

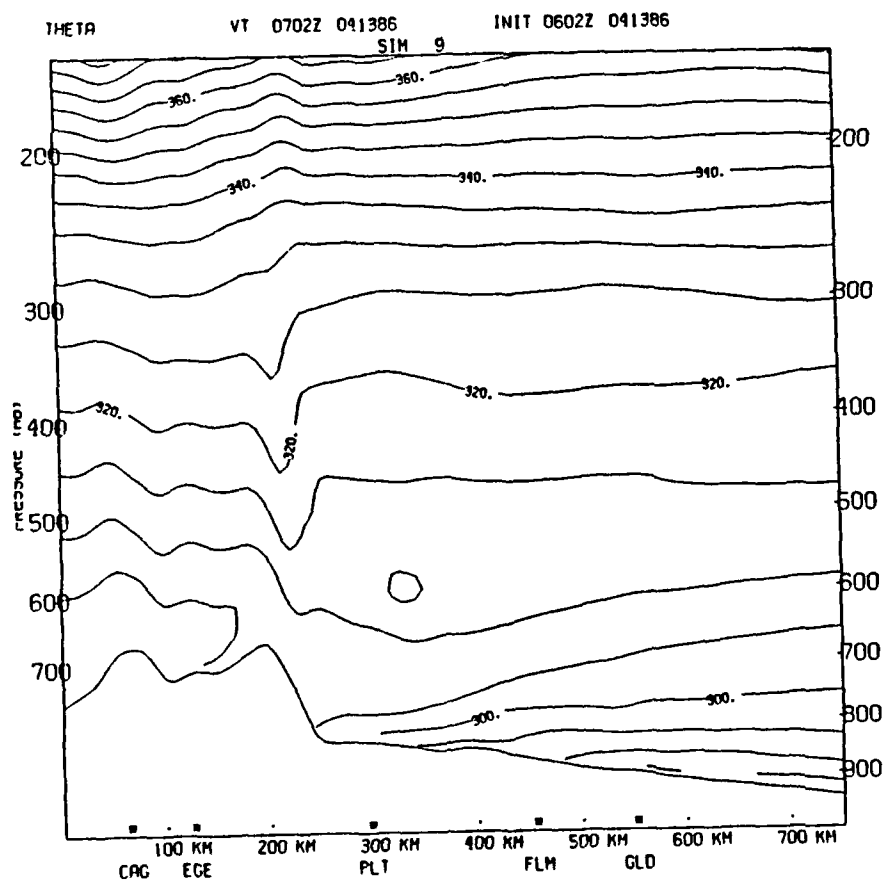
TIME UTC 41386



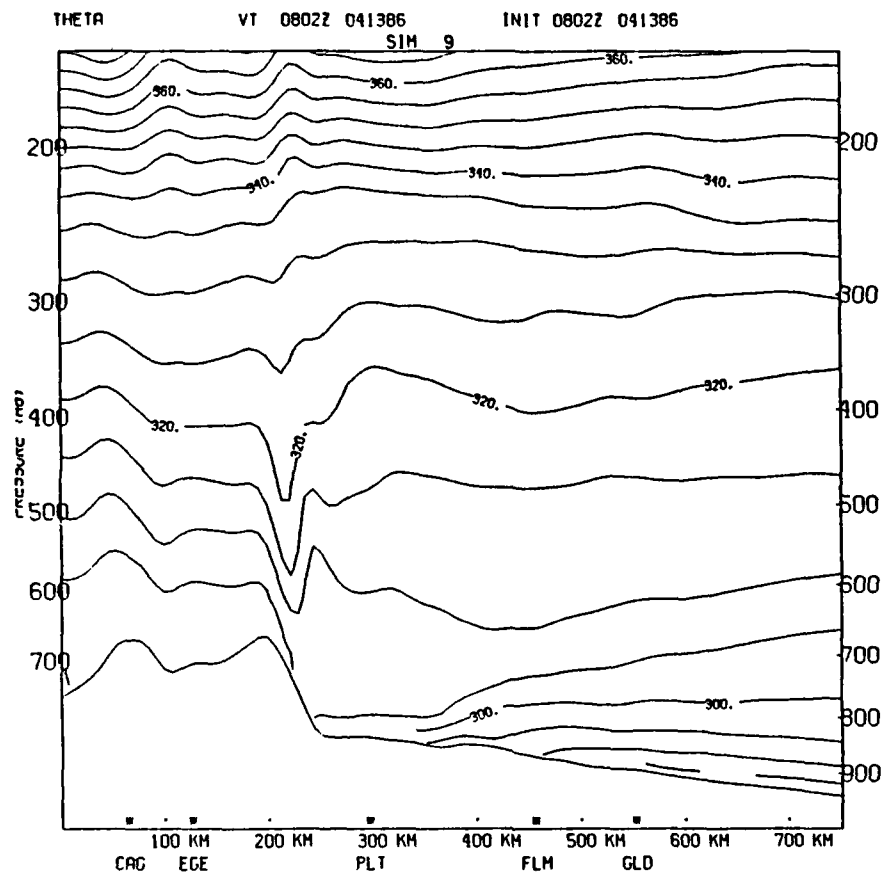
e



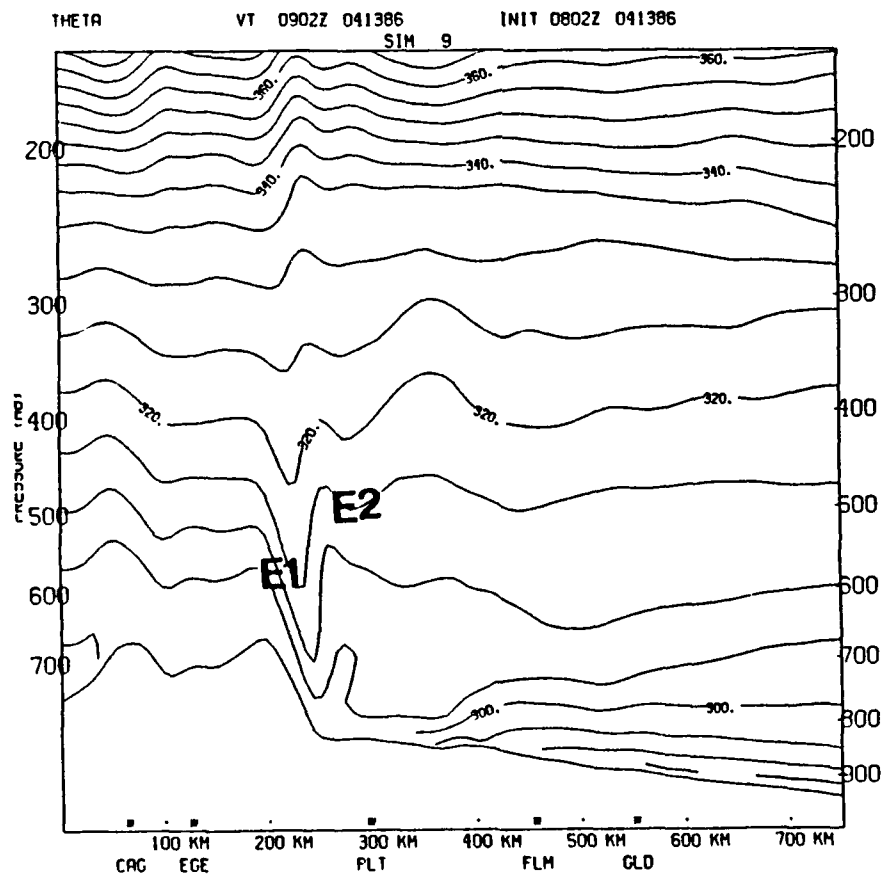
a



b

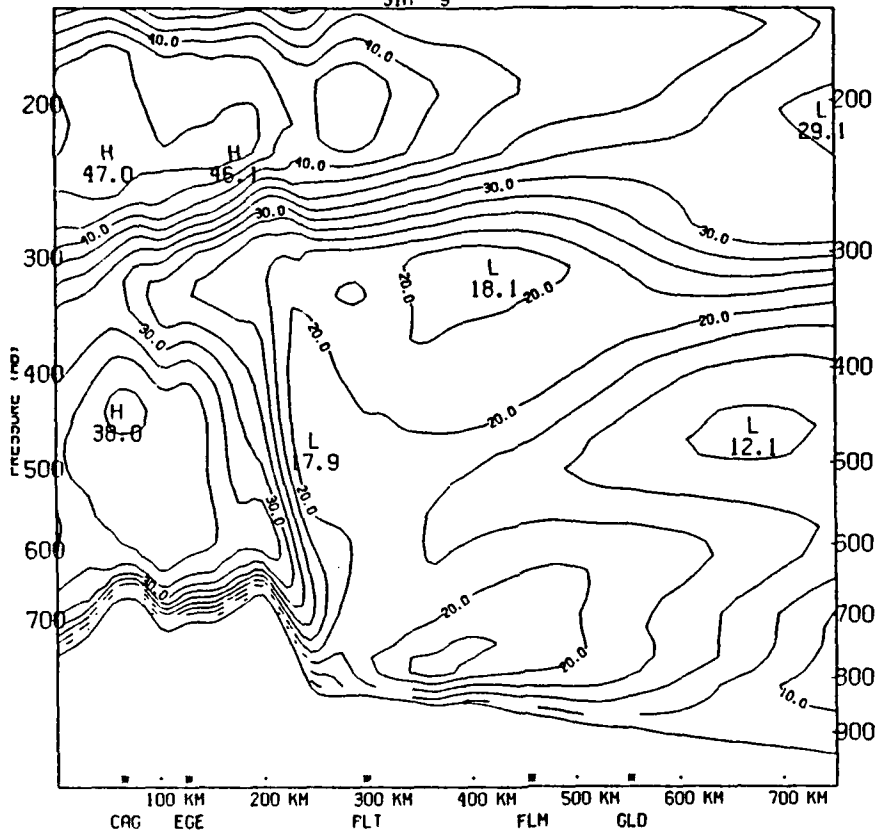


c



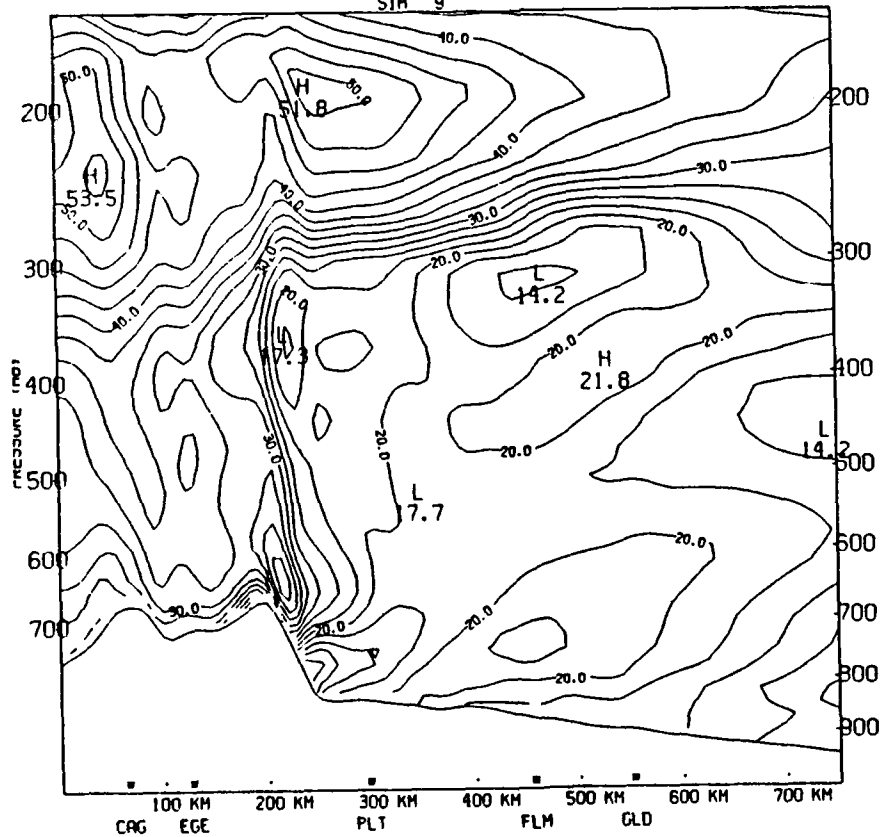
d

TOTAL WIND VT 0602Z 041386 INIT 0602Z 041386
SIM 9

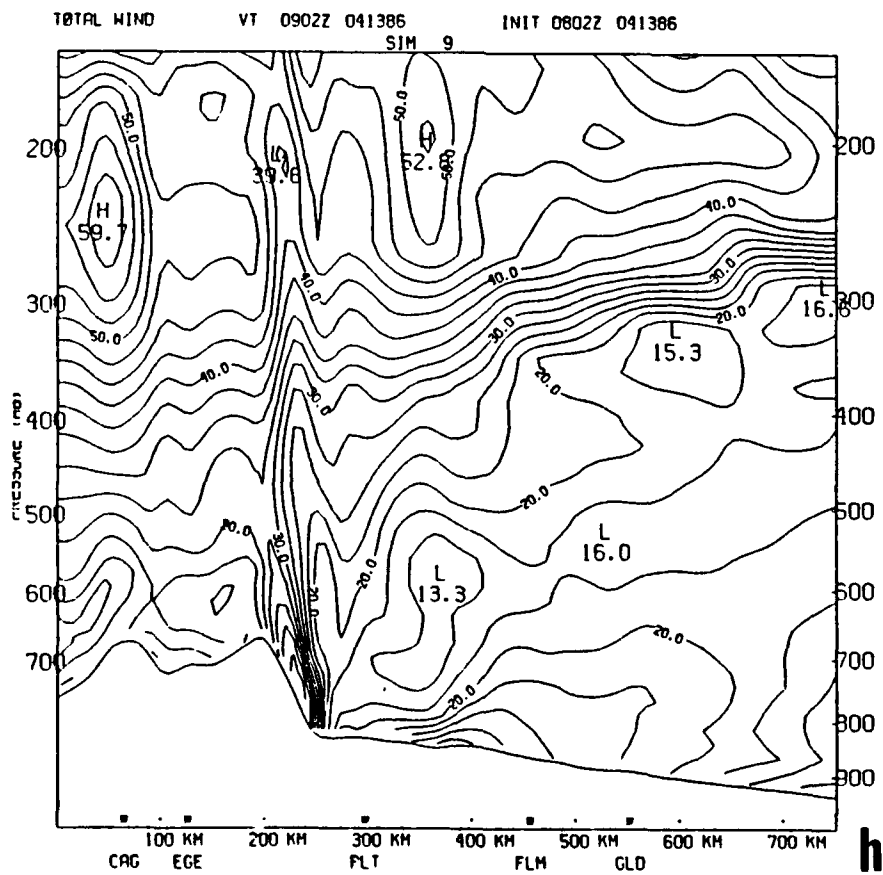
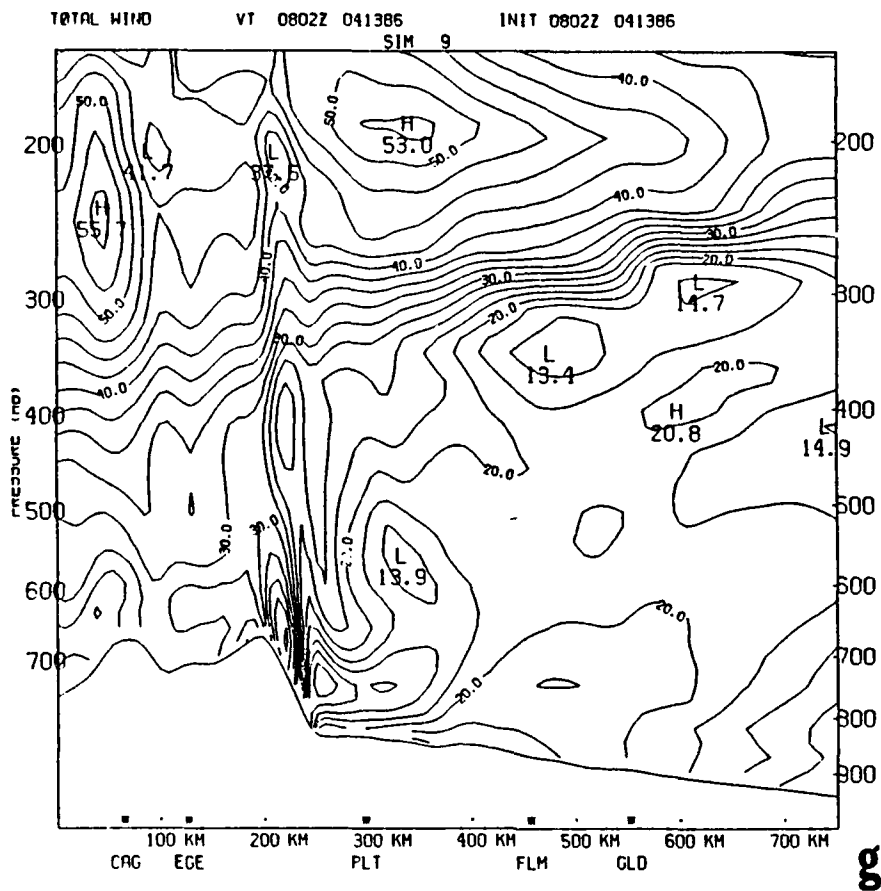


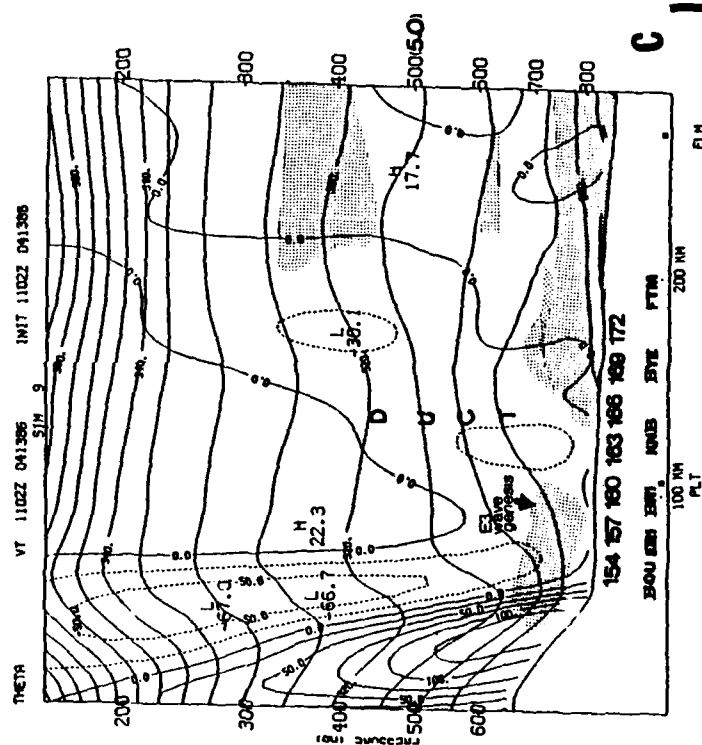
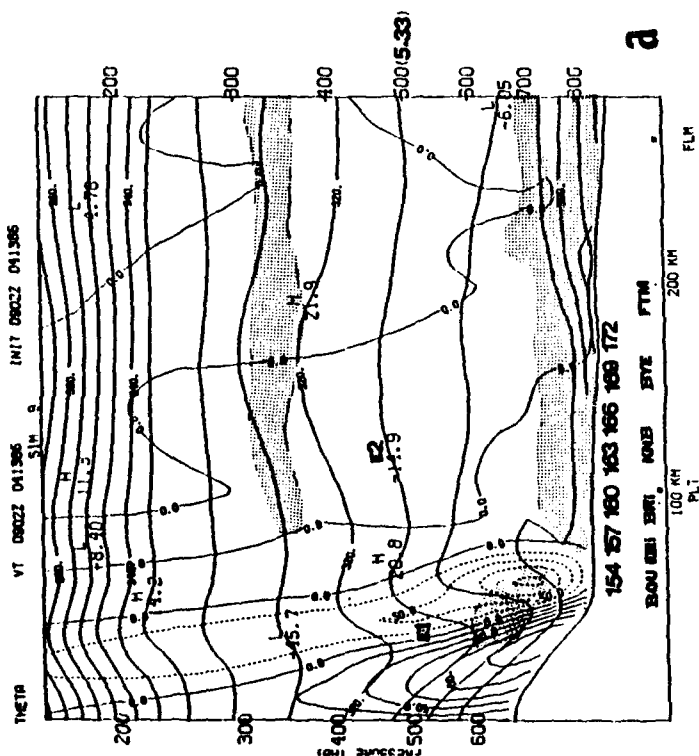
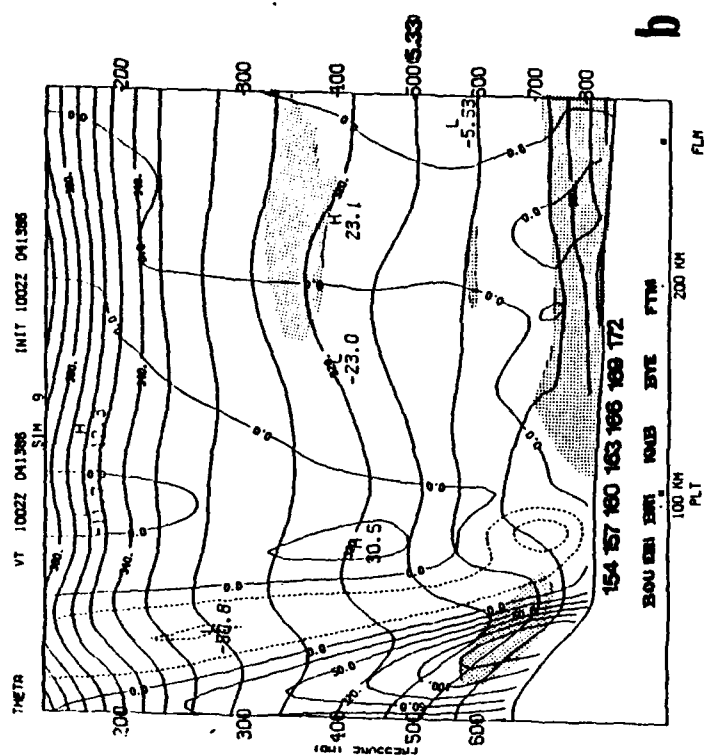
e

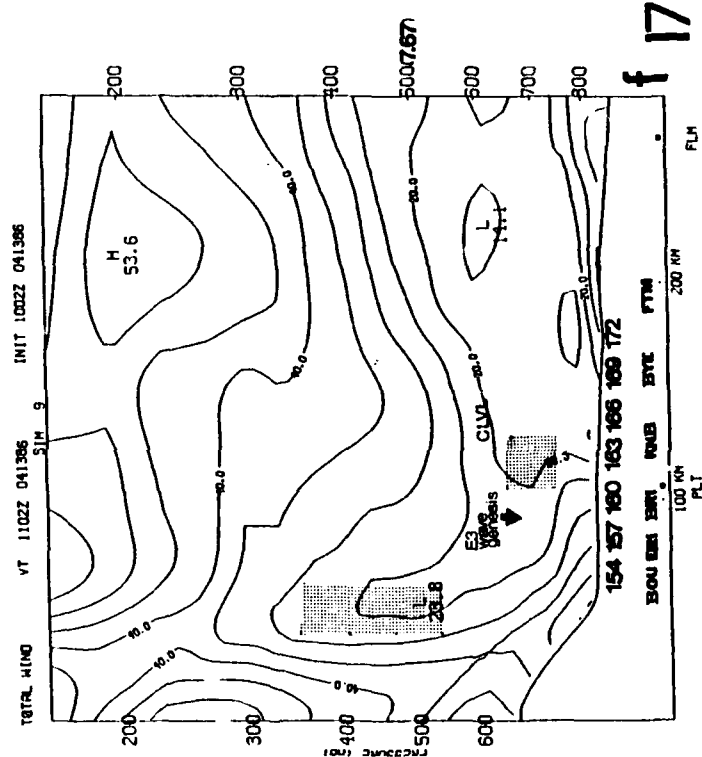
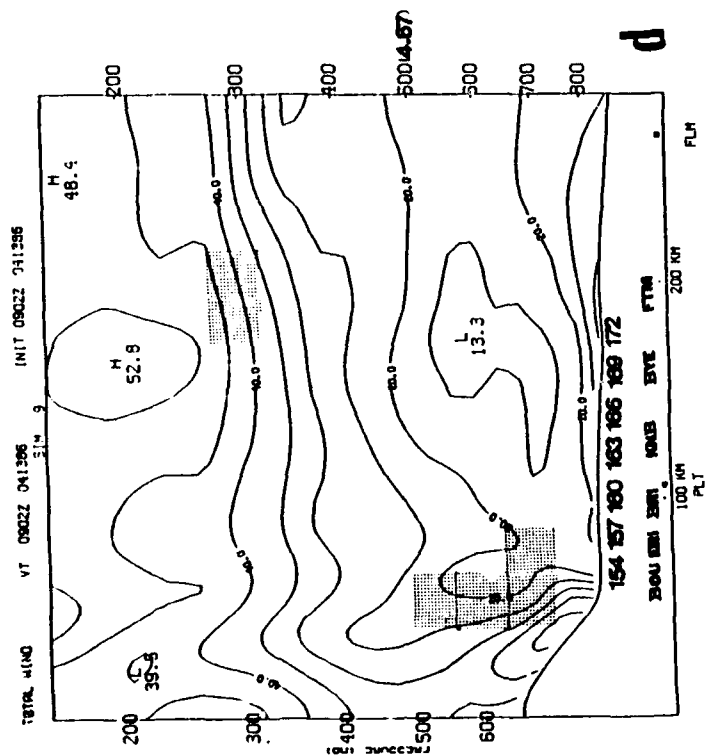
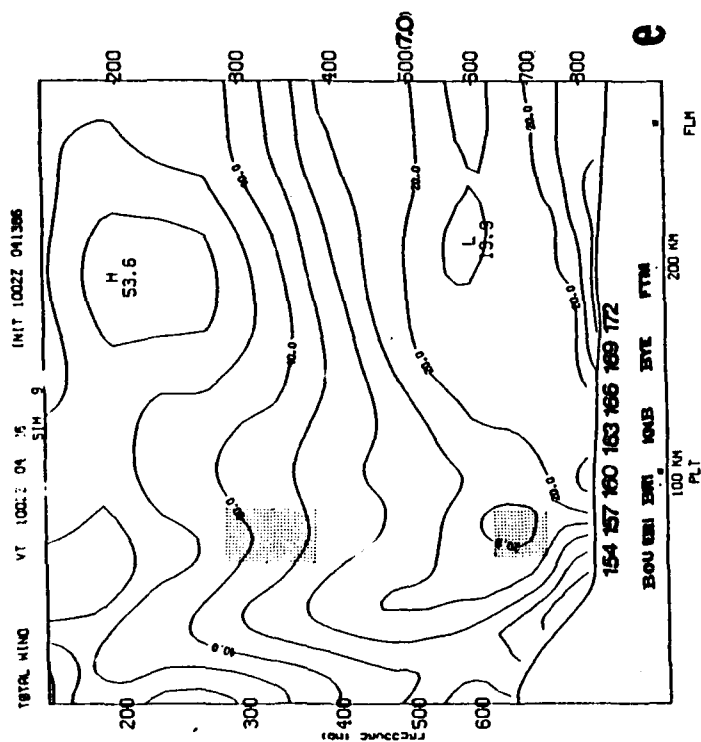
TOTAL WIND VT 0702Z 041386 INIT 0602Z 041386
SIM 9

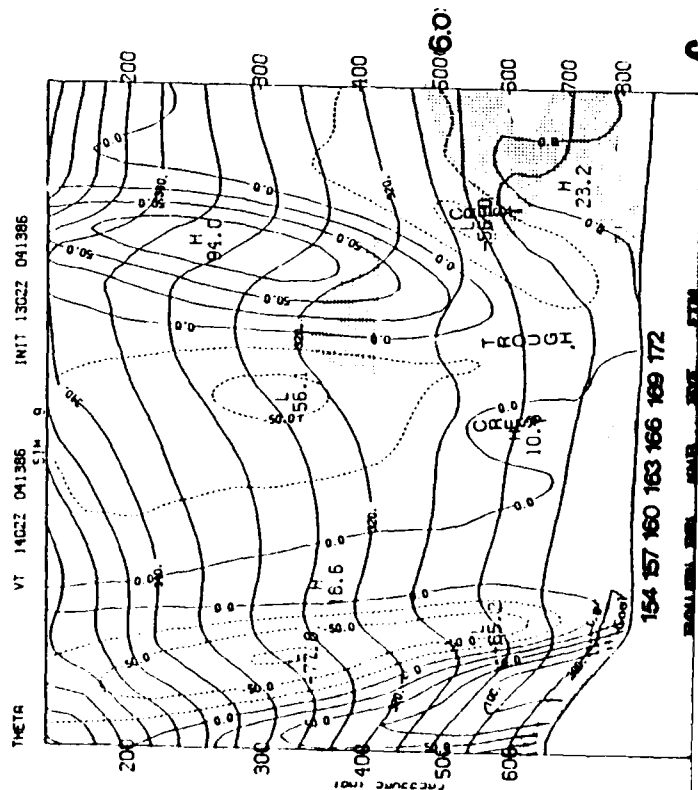
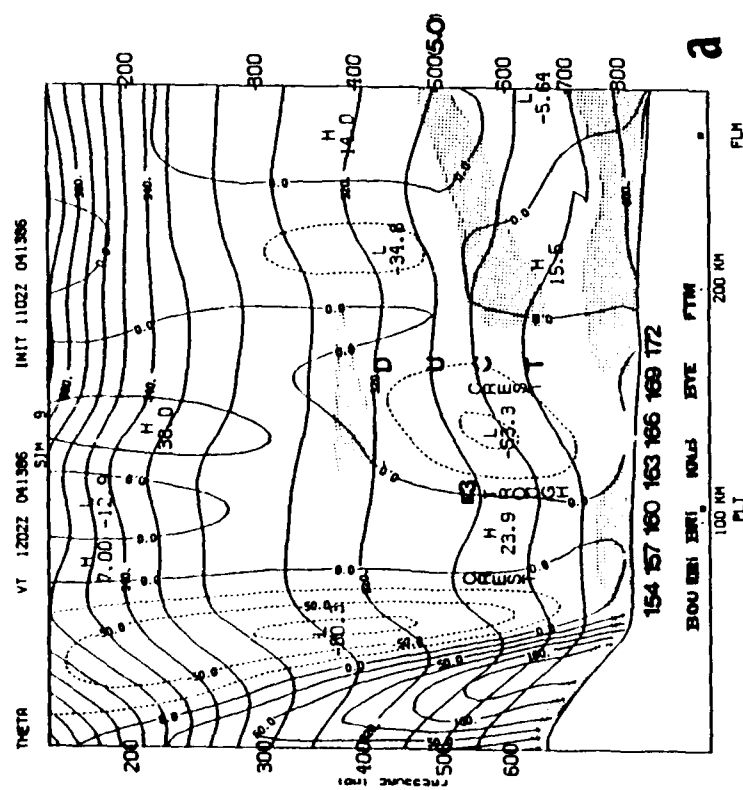
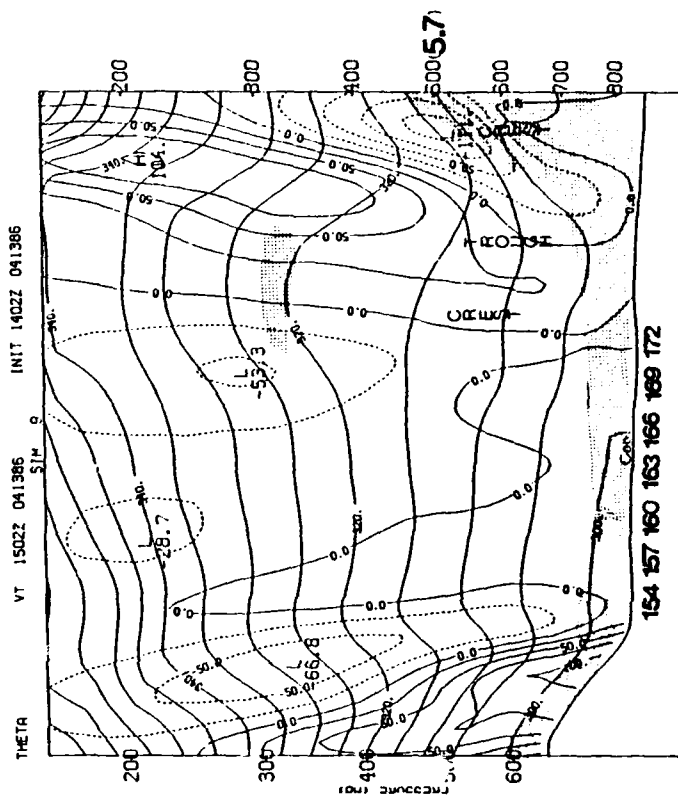
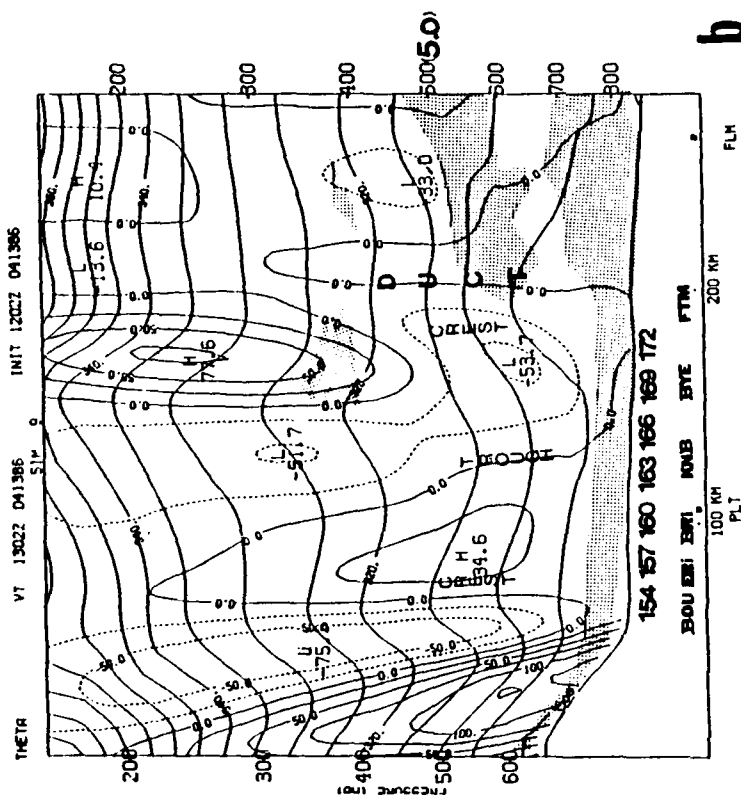


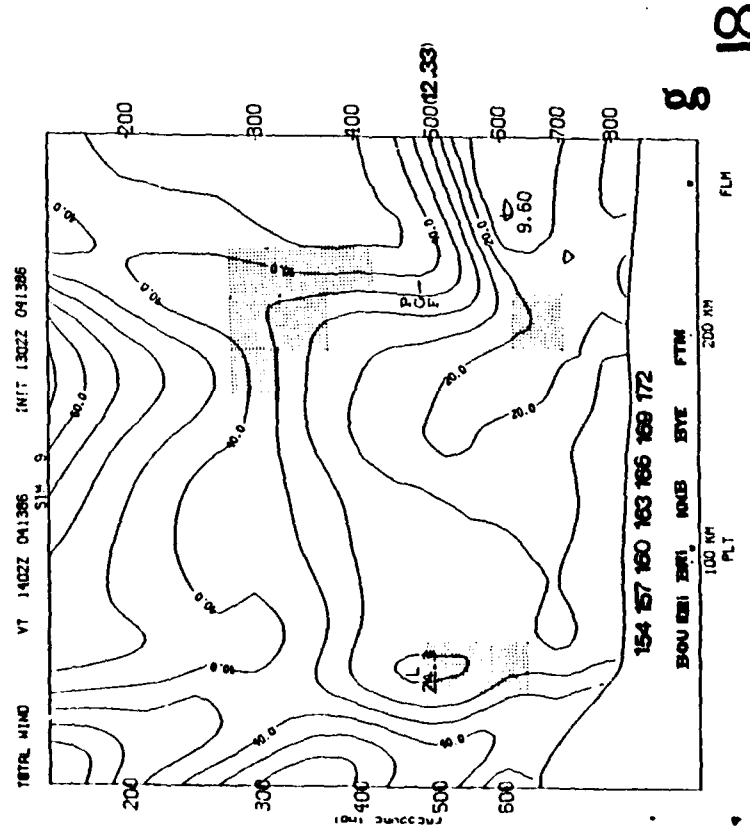
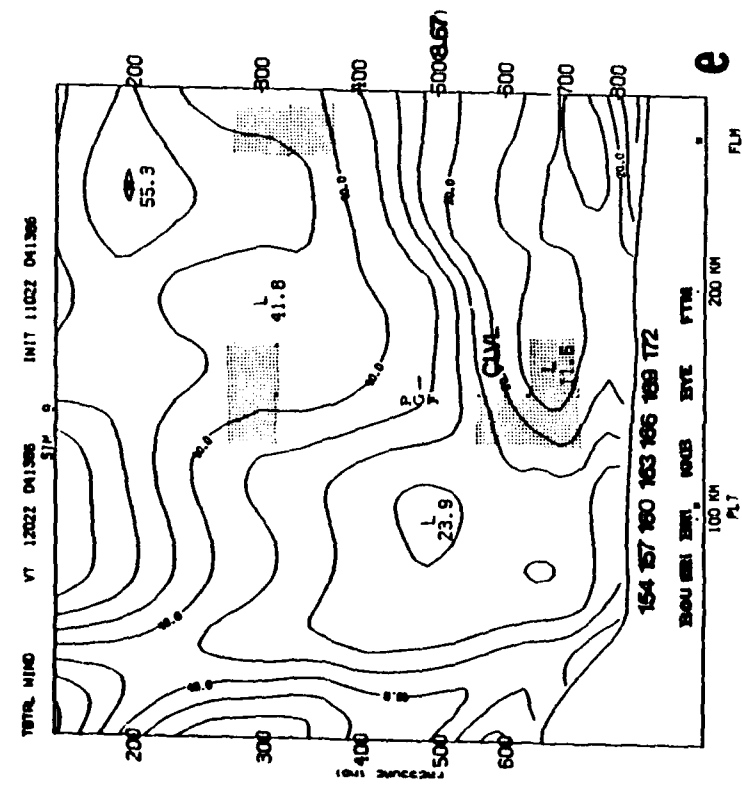
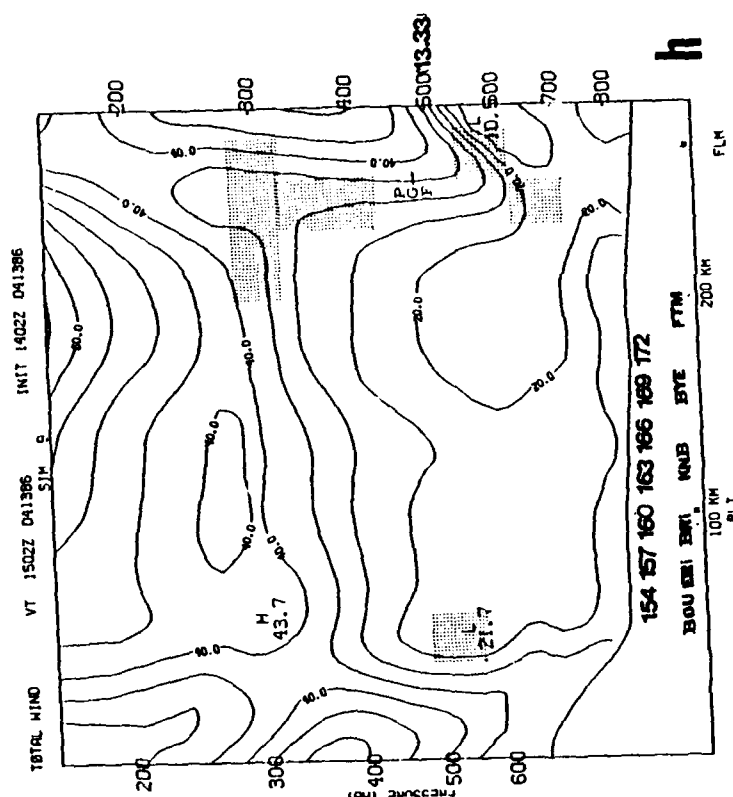
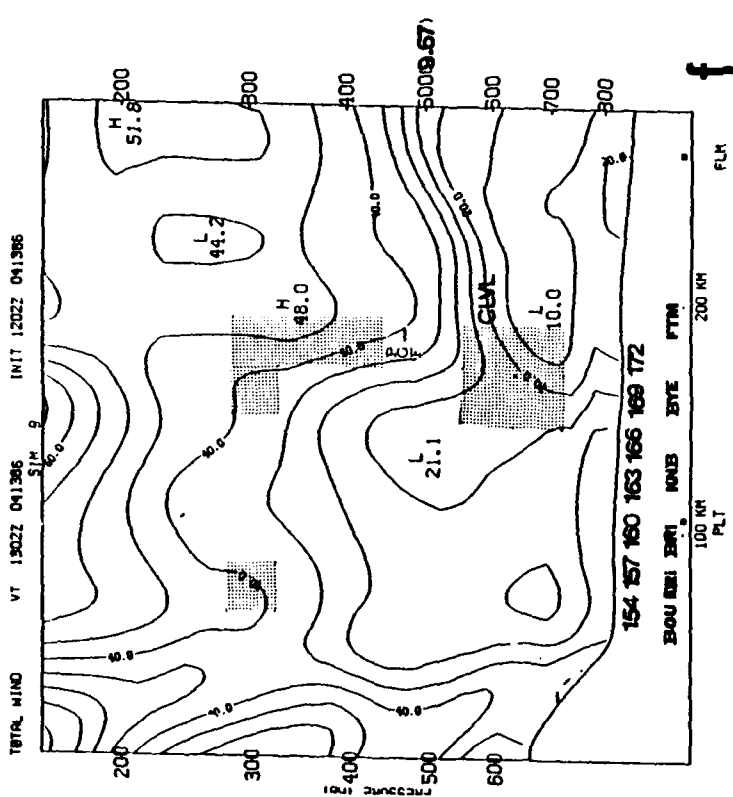
f

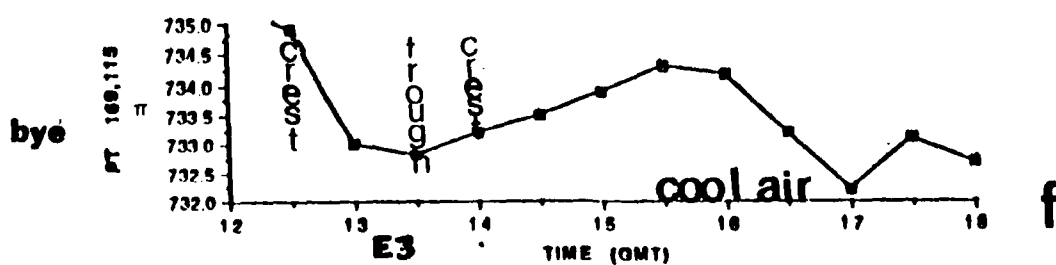
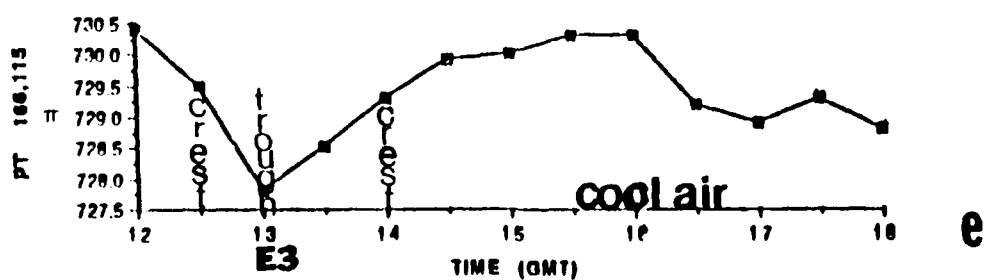
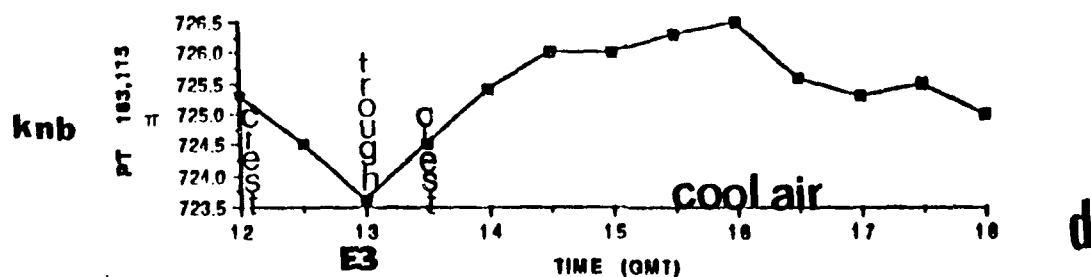
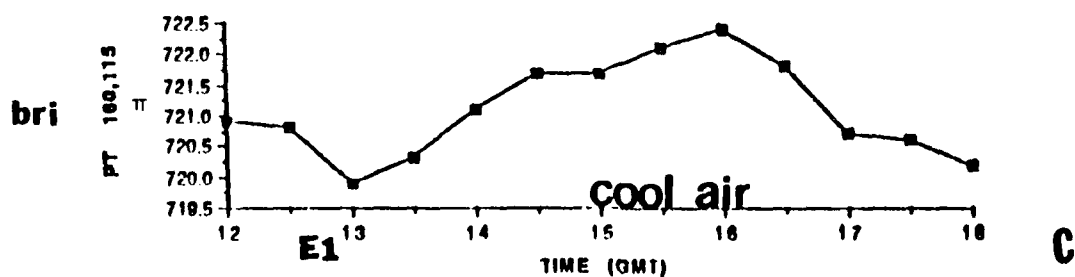
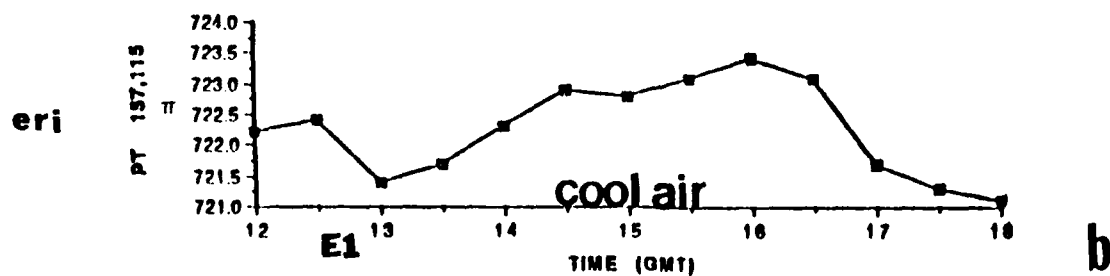
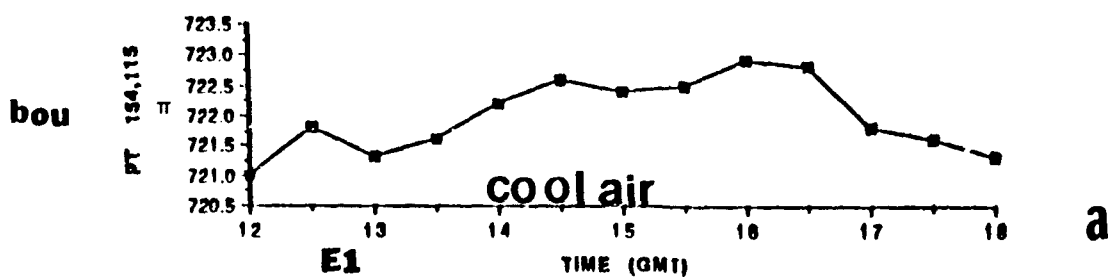


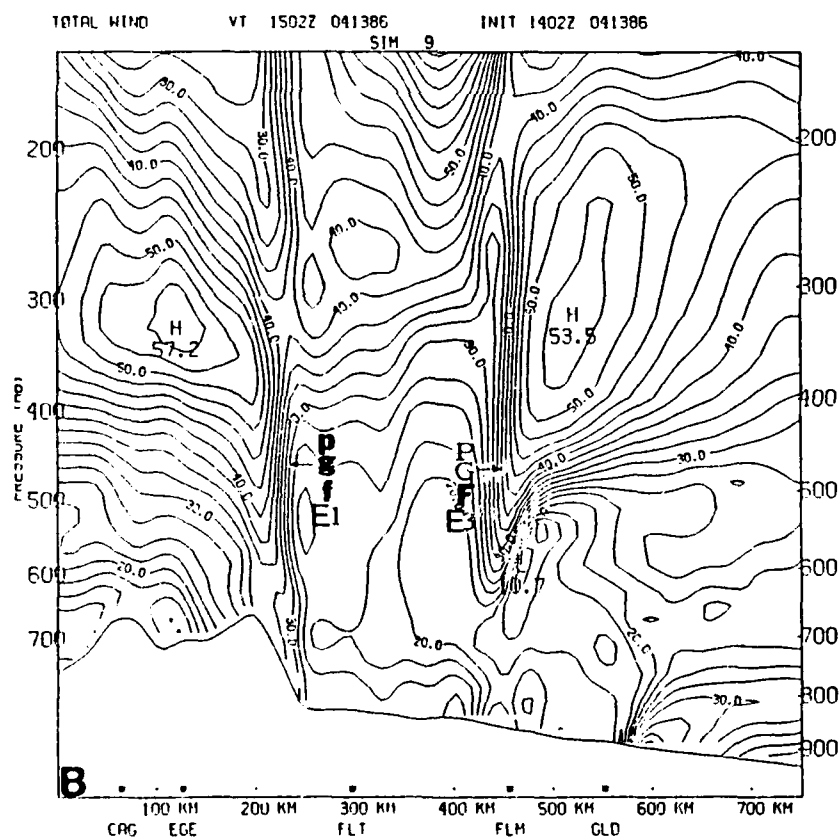
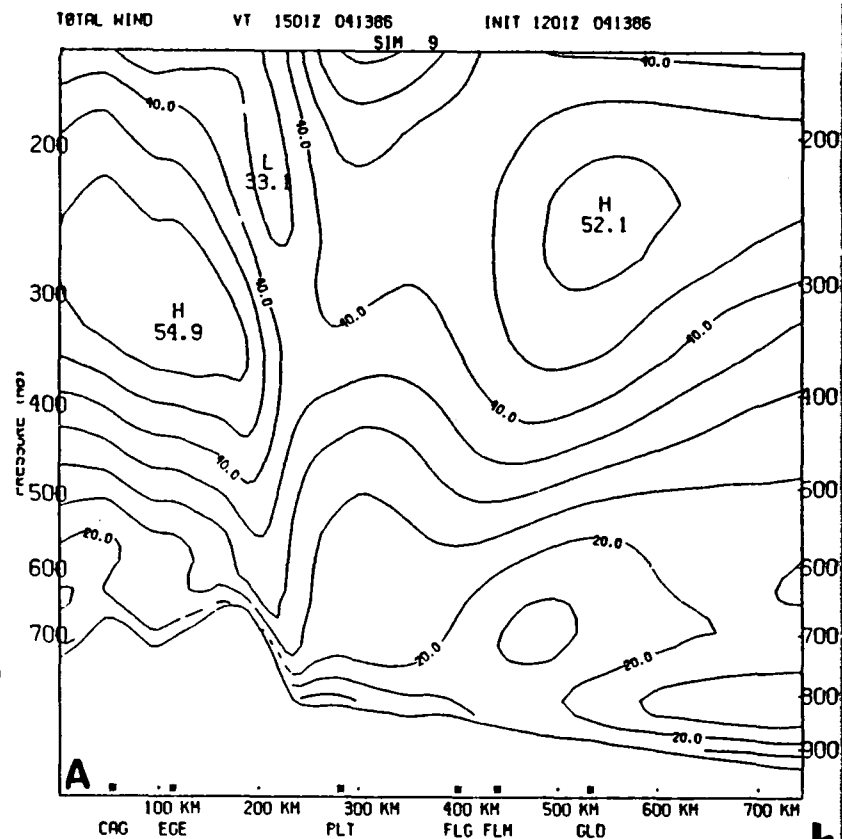
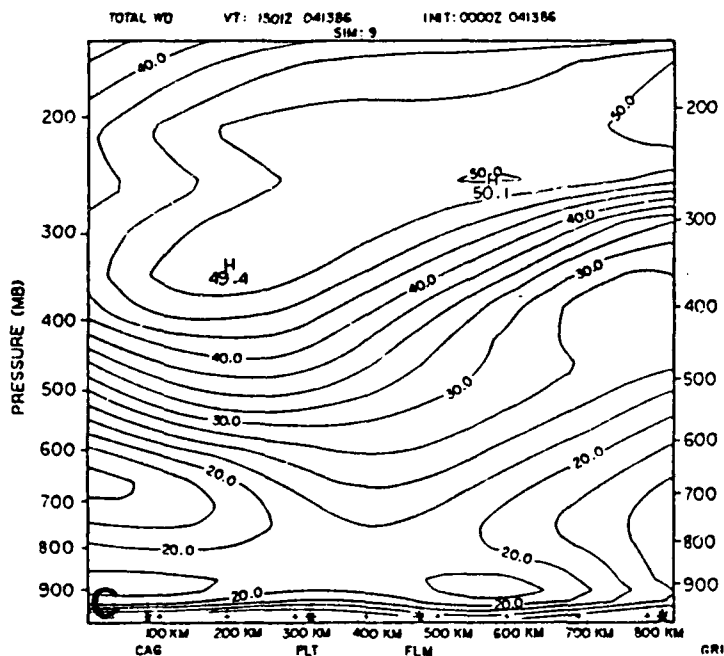


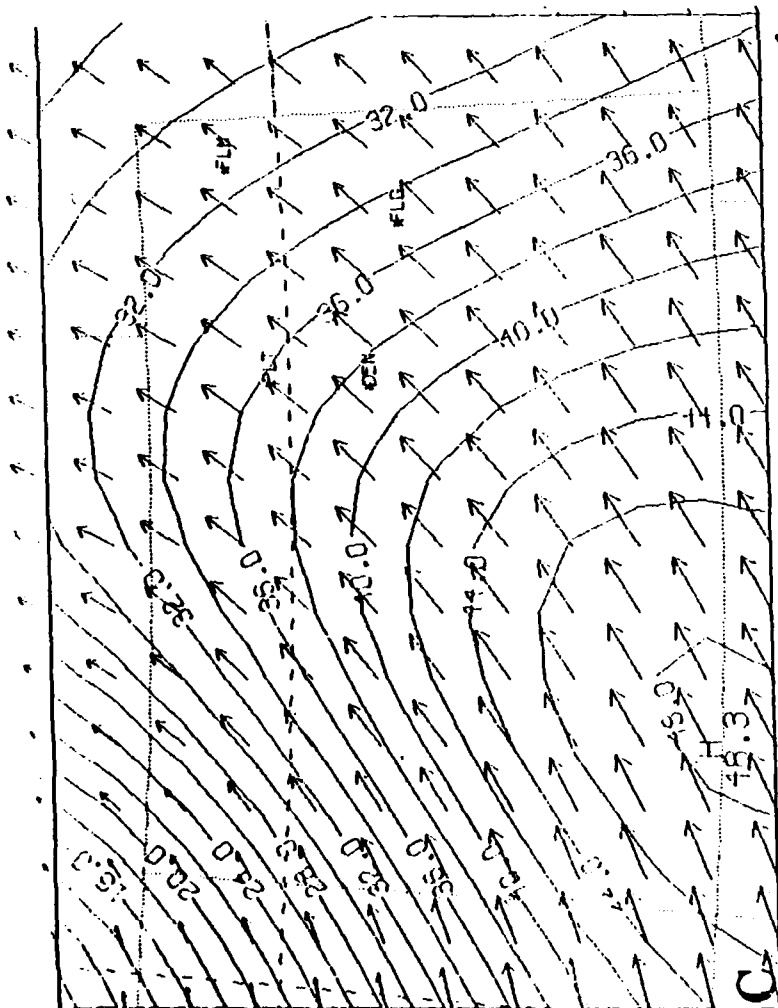




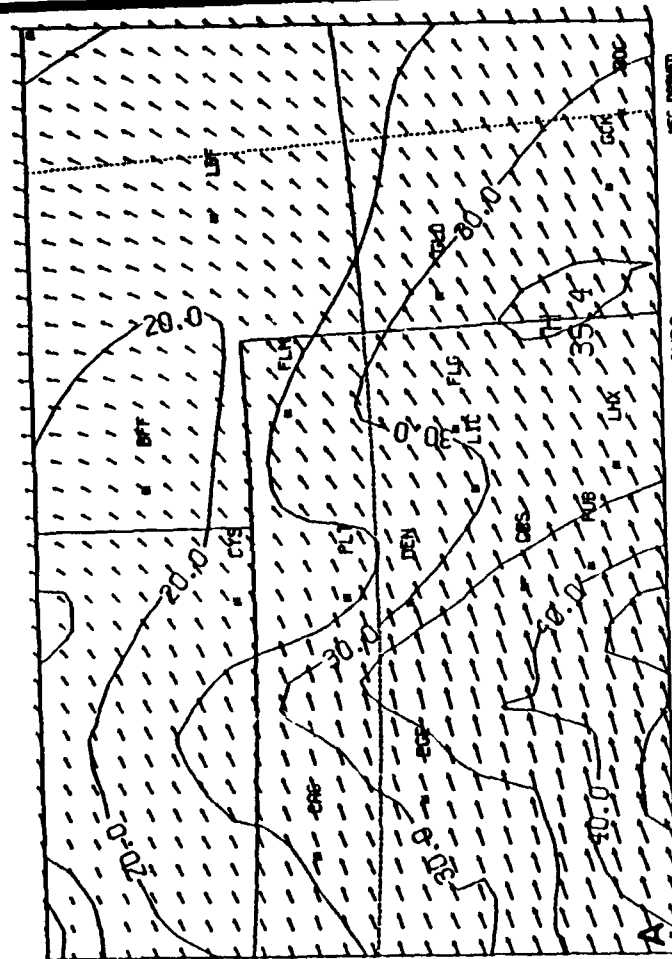
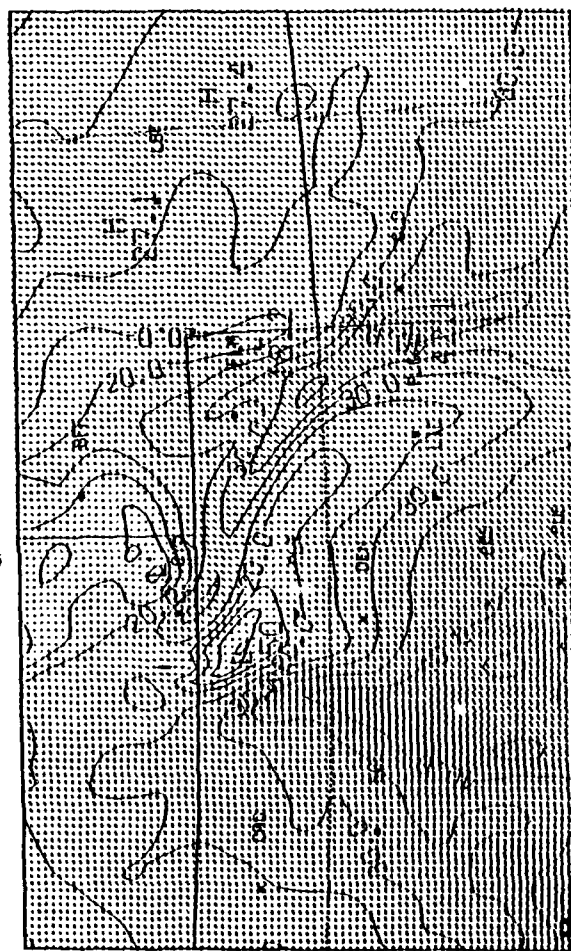








d



NEC DRAINED
SCALED BY 0.10 -01

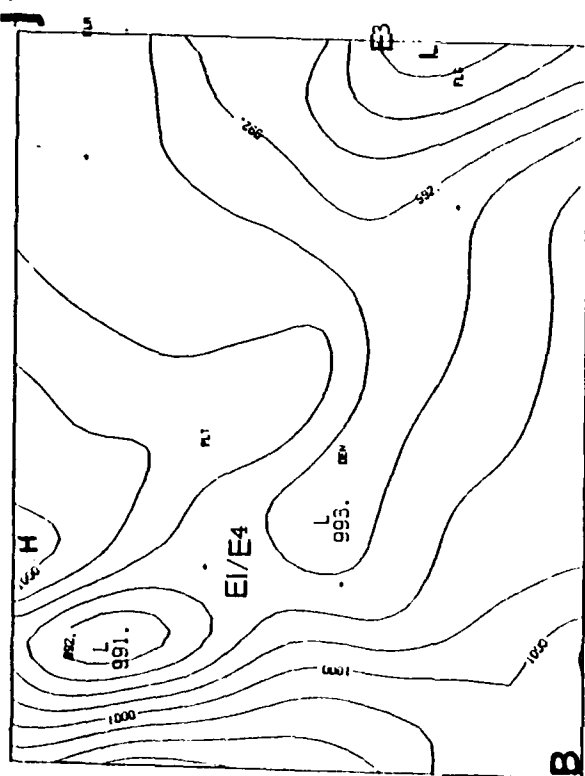
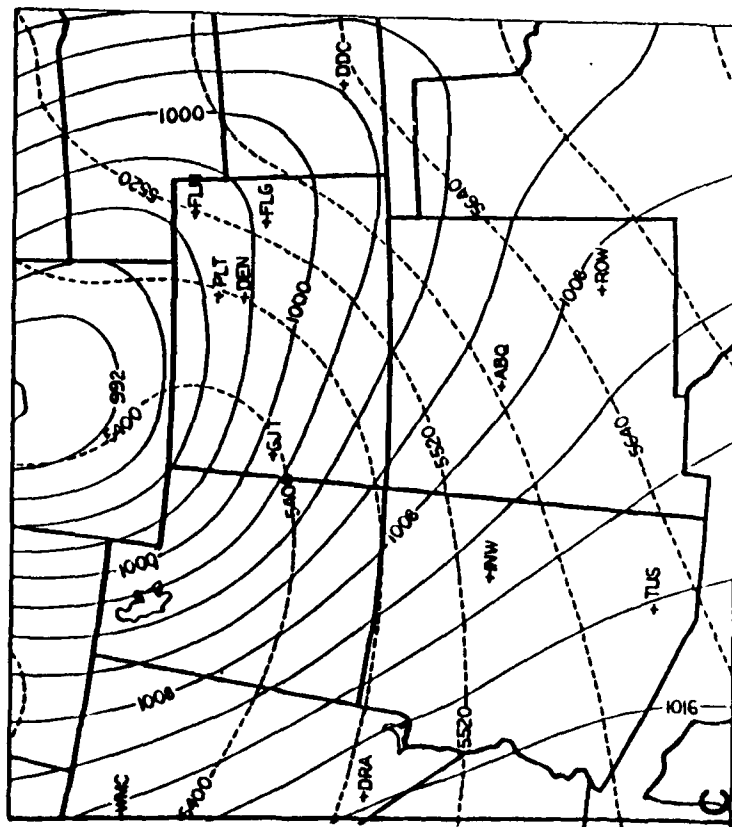
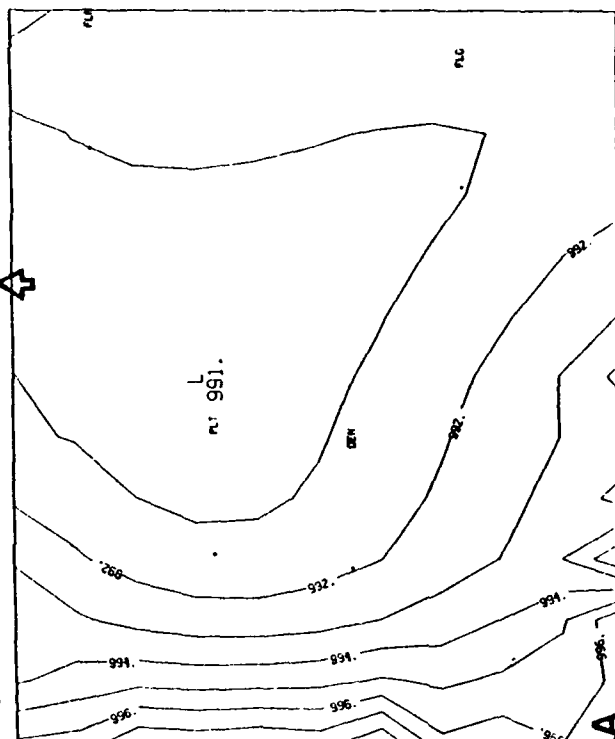
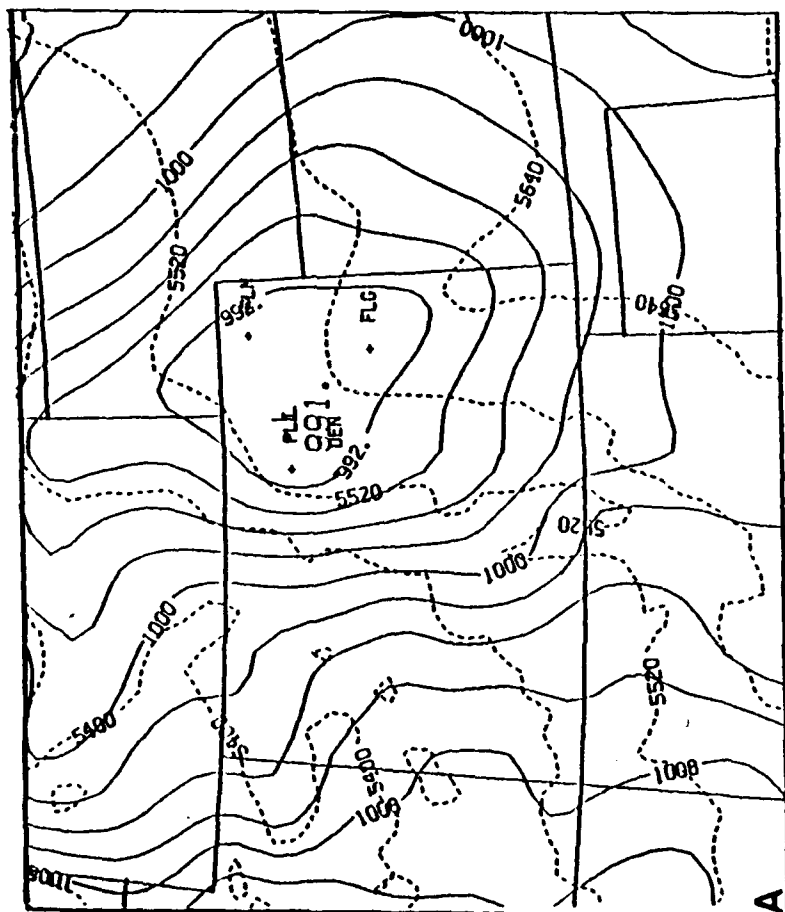
500 WINDS

MRSS 4.0 VT 1500Z 041386
INIT 1200Z 041386

NEC DRAINED
SCALED BY 0.10 -01

500 WINDS

MRSS 4.0 VT 1501Z 041386
INIT 1501Z 041386



REGION 3.0	7	KM NEST	SIMULATION	P
MSL P/TIMIN	VT	18012	041386	041386

	SIMULATION	9
28 KM NEST		

